

Microstructured hollow fibers and microsieves
Fabrication, characterization and filtration applications

Pınar Zeynep Çulfaz

MICROSTRUCTURED HOLLOW FIBERS
AND MICROSIEVES

Fabrication, Characterization and Filtration Applications

The research presented in this thesis was financed by MicroNed, workpackage 3-C: Phase Separation Microfabrication.

Promotion committee

Prof. Dr. Ir. R.G.H. Lammertink (promotor)	University of Twente
Prof. Dr.-Ing. M. Wessling (co-promotor)	University of Twente, RWTH Aachen University, Germany
Prof. Dr. Ir. W.G.J. van der Meer	University of Twente/Wetsus
Prof. Dr. G. Mul	University of Twente
Prof. Dr.-Ing. T. Melin	RWTH Aachen University, Germany
Prof. Dr. G. Lipscomb	University of Toledo, U.S.A.

Microstructured hollow fibers and microsieves: Fabrication, characterization and filtration applications

ISBN: 9789036531177

DOI: <http://dx.doi.org/10.3990/1.9789036531177>

Printed by Gildeprint Drukkerij, Enschede, The Netherlands

© 2010 Pınar Zeynep Çulfaz, Enschede, The Netherlands

MICROSTRUCTURED HOLLOW FIBERS AND MICROSIEVES

FABRICATION, CHARACTERIZATION AND FILTRATION APPLICATIONS

DISSERTATION

to obtain
the degree of doctor at the University of Twente,
on the authority of the rector magnificus,
Prof. Dr. H. Brinksma,
on account of the decision of the graduation committee,
to be publicly defended on
Friday the 3rd of December, 2010, at 13:15

by

Pınar Zeynep Çulfaz

born on February 26th, 1981
in Ankara, Turkey

This thesis has been approved by:

Prof. Dr. Ir. R.G.H. Lammertink (promotor)

Prof. Dr.-Ing. M. Wessling (co-promotor)

CONTENTS

1	Introduction	1
1.1	Phase inversion membranes	3
1.2	Membrane performance criteria	6
1.2.1	Permeability and retention	6
1.2.2	Concentration polarization and fouling	6
1.3	Microstructured membranes	15
1.4	Microsieves	16
1.5	Scope of the thesis	17
1.6	References	18
2	Hollow fiber membranes with microstructured outer skin	27
2.1	Introduction	29
2.2	Experimental	30
2.2.1	Fabrication of the fibers	30
2.2.2	Characterization of the fibers	32
2.2.3	Characterization of the polymer dopes	34
2.3	Results and Discussion	35
2.3.1	Fiber morphology	35
2.3.2	Fiber performance	42
2.4	Conclusions	48
2.5	References	49
3	Fouling behavior of microstructured hollow fiber membranes in dead-end filtrations: Critical flux determination and NMR imaging of particle deposition	53
3.1	Introduction	55
3.2	Experimental	56
3.2.1	Membranes	56
3.2.2	Materials	57
3.2.3	Flux-stepping Experiments	58
3.2.4	Nuclear Magnetic Resonance (NMR) imaging	58
3.3	Results and Discussion	60
3.3.1	Flux-stepping experiments with colloidal silica	60
3.3.2	NMR imaging of silica deposition	62
3.3.3	Flux-stepping experiments with sodium alginate	69
3.4	Conclusions	73
3.5	References	74
	Appendix: Calculation of the diffusion coefficient	77
4	Fouling behavior of microstructured hollow fibers in cross-flow filtrations: Critical flux determination and direct visual observation of particle deposition	79
4.1	Introduction	81
4.2	Experimental	82
4.2.1	Membranes and modules	82
4.2.2	Flux-cycling experiments	83

4.2.3	Direct-visual observation (DVO) experiments	85
4.3	Results and Discussion	87
4.3.1	Flux-cycling experiments	87
4.3.2	Direct visual observation of yeast deposition	95
4.4	Conclusions	97
4.5	References	98
5	Fouling behavior of microstructured hollow fiber membranes in submerged and aerated filtrations	103
5.1	Introduction	105
5.2	Experimental	106
5.2.1	Flux-stepping Experiments	107
5.3	Results and Discussion	108
5.3.1	Comparison of round, structured and twisted fibers	109
5.3.2	Effect of aeration rate	111
5.3.3	Effect of module orientation and bubble size	113
5.3.4	Effect of sub-mm sized bubbles	114
5.4	Conclusions	115
5.5	References	116
6	Hollow fiber ultrafiltration membranes with microstructured inner skin	119
6.1	Introduction	121
6.2	Experimental	122
6.2.1	Fiber Fabrication	122
6.2.2	Fiber Characterization	123
6.3	Results and Discussion	124
6.3.1	Fiber morphology	124
6.3.2	Fiber performance	128
6.4	Conclusions	132
6.5	References	133
7	Polymeric microsieves made by phase separation micro-molding: Downscaling perforation size by solvent-shrinking and optimizing mold design for easier release	137
7.1	Introduction	139
7.2	Experimental	141
7.2.1	Microsieve preparation	141
7.2.2	Molds	141
7.2.3	Microsieve shrinkage	143
7.2.4	Peeling test	143
7.2.5	Membrane inspection	143
7.3	Results and Discussion	144
7.3.1	Downscaling of perforation size by solvent shrinking	144
7.3.2	Influence of mold design on release	151
7.4	Conclusions	154
7.5	References	156
8	Summary and Outlook	159
8.1	Prologue	160

8.2	Summary	160
8.3	Reflections	163
8.3.1	Fabrication of microstructured hollow fibers	163
8.3.2	Characterization of fouling behavior	165
8.3.3	Fouling of the microstructured fibers with more complex feed solutions	167
8.3.4	Polymeric microsieves via phase separation microfabrication	168
8.4	Epilogue	169
8.5	References	169
	Summary	171
	Samenvatting	173
	Acknowledgements	175

CHAPTER 1

Introduction

A membrane is a barrier which separates two phases and selectively transports certain species while it restricts the transport of others [1]. Synthetic membranes are produced since the early 1900's and have found industrial use in 1960's with the Loeb-Sourirajan process of making defect-free, high-flux membranes [1, 2]. These membranes are formed via phase separation of a polymer solution in a nonsolvent. They have an asymmetric structure with a thin, selective skin on a much thicker but highly porous supporting layer. Today many membranes used in ultrafiltration, reverse osmosis and gas separation are fabricated by this technique, called phase inversion [1, 3].

1.1 Phase inversion membranes

A variety of membrane structures can be obtained via phase inversion. The structure of the membrane depends on both the thermodynamics of the system and the kinetics of phase separation [1–5]. The phase diagram of a typical membrane forming system is schematically shown in Figure 1.1. The system has three components: A polymer, a solvent and a nonsolvent, which is miscible with the solvent but not with the polymer. The corners of the ternary diagram represent pure components and the sides represent binary mixtures of the two components connected. The binodal boundary divides the phase diagram into a single-phase region, where the three components are miscible in all compositions, and a two-phase region, where the system separates into two phases. The compositions of the two phases are connected by the tie-lines. At the end of phase separation, the polymer-rich phase forms the membrane matrix, whereas the polymer-lean phase forms the membrane pores. The two-phase region can be further divided into a metastable region and an unstable region. Within the metastable region between the binodal and spinodal boundaries, phase separation is thermodynamically favored, however the system is stable against small concentration fluctuations ($\partial^2 G / \partial x^2 > 0$). Within this region, phase separation proceeds via nucleation and growth of one of the phases (path A, Figure 1.1). On the other hand, within the spinodal region all compositions are unstable ($\partial^2 G / \partial x^2 < 0$) and the phase transition occurring within this region is characterized by a fast and uniform separation of the two phases (path B, Figure 1.1). Spinodal decomposition leads to interconnected, bicontinuous structures (Figure 1.2(b)), whereas nucleation and growth results in cellular structures (Figure 1.2(c)). Closed cells form if the growth of nuclei stops in the initial stages. If the

nuclei grow and touch each other, an open-cellular structure is formed.

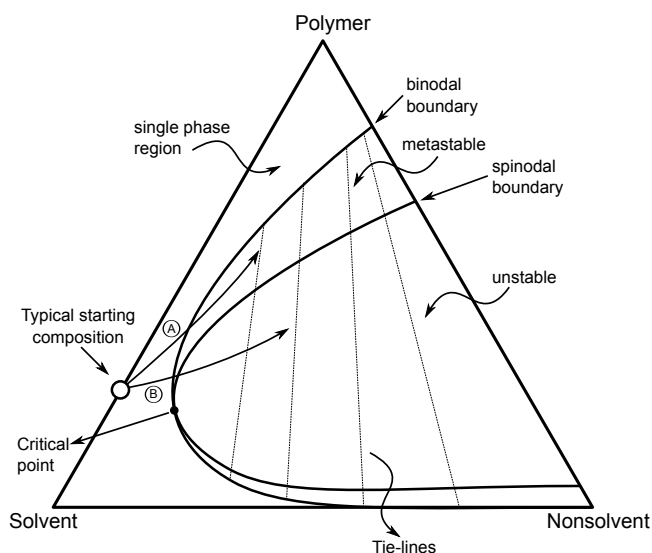


Figure 1.1: Ternary phase diagram of a simple membrane forming system of a polymer, a solvent and a nonsolvent. Two paths A and B illustrate qualitatively two possible paths through which phase separation can occur.

In ultrafiltration membranes and some gas separation membranes, often a nodular structure is observed (Figure 1.2(d)). The origin of this structure has been explained in different ways. In earlier observations, the origin of nodules were attributed to micelles [6], aggregates [7], perturbations at the membrane-coagulant interface [8] or nuclei of the polymer-rich phase which form during phase separation by nucleation and growth [3]. Later, it has been argued by several authors that these structures are generated by spinodal decomposition [9–12]. Pinnau and Koros suggested that nodules can arise due to surface tension induced breakup of the bicontinuous spinodal network [11]. Wienk et al. reported that the dimensions of nodular structures found in ultrafiltration membranes coincide with the fastest growing wavelength of the concentration fluctuations, according to the spinodal demixing theory [13, 14]. Boom et al. suggested that a bicontinuous structure formed in early stages by spinodal demixing can develop into a discontinuous morphology with spherical domains [15]. The coarsening of a bicontinuous, interconnected pore structure into noncircular pores

and ultimately into circular pores was observed by Akthakul and co-workers [9].

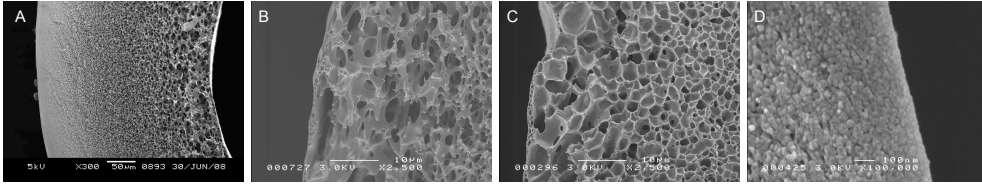


Figure 1.2: (a) An asymmetric membrane with the skin layer on the left of the picture. (b) A bicontinuous pore structure. (c) A cellular pore structure. (d) Nodular structure in the skin layer of an ultrafiltration membrane.

Although the phase equilibrium of the membrane forming system determines what kind of phase transitions can occur, it is mostly the kinetics of the process that determines the final result. In membrane forming systems, equilibrium is often not reached and the membrane structure is determined by the rate and ratio of solvent and nonsolvent diffusion [3, 4].

When the polymer solution is immersed in the coagulation medium in the liquid phase, the solvent diffuses out of the solution and the nonsolvent diffuses in. This brings the interface between the solution and the coagulation medium rapidly to a concentration within the two-phase region. The coagulated structure in the interface is finely microporous due to the high polymer concentration at the moment of phase separation [2]. This layer which coagulates first forms the “skin” of the membrane and acts as a barrier for diffusion of components through it. The formation of a skin causes slower coagulation in the bulk of the solution and results in a highly porous structure below the skin layer, forming an asymmetric membrane (Figure 1.2(a)) [1].

When phase separation is induced by nonsolvent vapor, coagulation occurs more slowly and forms a homogeneous structure throughout the membrane thickness, with large pores [2]. A similar structure is obtained when the polymer solution is coagulated in a mixture of nonsolvent and solvent [16, 17].

Very often, membrane forming solutions consist of more than simply the polymer and the solvent. Having a certain amount of nonsolvent in the starting polymer solution, which brings the solution closer to the binodal boundary increases the porosity and decrease the thickness of the skin layer [4, 18]. Polymeric additives such as polyvinylpyrrolidone (PVP) and polyethyleneglycol (PEG) were shown to increase

pore size, pore connectivity and hydrophilicity, the latter being an important factor in reducing fouling [19–21]. The addition of PVP in some systems also suppresses macrovoid formation [15, 21].

1.2 Membrane performance criteria

1.2.1 Permeability and retention

The main performance criteria for a membrane are its permeability and its selectivity or retention to certain species. The first characterizes the quantity of the product, while the second characterizes its quality.

In asymmetric membranes, the skin layer forms the major resistance to flow. Therefore, to achieve a high permeability, the skin layer should be thin and highly porous. In addition to the requirement that the membrane should be as permeable as possible, it is also desired to increase the membrane area packed within a given volume [22].

Ultrafiltration and microfiltration membranes, which are the subjects of this thesis, retain particles through size sieving. The pore size distribution of these membranes can be determined by a number of methods such as permoporometry, thermoporometry, bubble point and microscope observations [23–28]. It can also be deduced from the retentions of a mixture of solutes. The molecular weight of the molecule which is retained by 90 % is designated as the Molecular Weight Cut-off (MWCO). MWCO is the most common way of describing ultrafiltration membranes. However its value is strongly affected by the measurement conditions as the presence and extent of concentration polarization alters the retention of the membrane. To minimize concentration polarization in MWCO determination, the filtration needs to be done at low permeate flux and high cross-flow velocity [29, 30].

1.2.2 Concentration polarization and fouling

Concentration polarization is the reversible buildup of retained solutes or particles in the feed solution near the membrane-solution interface. As a result of the retention of the membrane, the layer of the feed solution near the membrane surface becomes

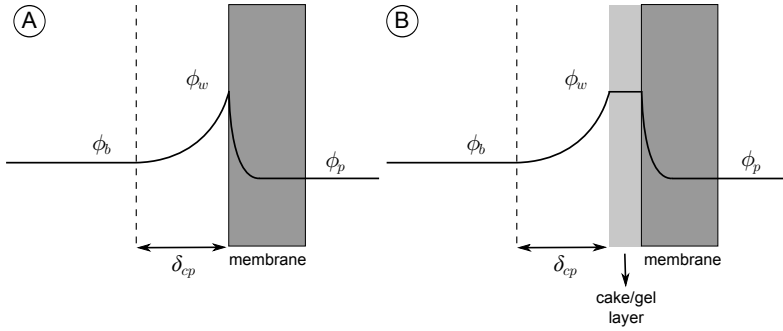


Figure 1.3: Schematic illustration of concentration polarization (a) and particle deposition (b) on the membrane.

depleted in the component dominantly permeating through the membrane and enriched in the retained component (Figure 1.3). The presence of concentration polarization increases the resistance to filtration and decreases the retention of the membrane. At steady-state, the net permeate flux of the retained component through the membrane equals the net flux of the component in the concentration polarization layer.

$$J\phi - D\frac{d\phi}{dx} = J\phi_p \quad (1.1)$$

where J is the permeate flux, ϕ is the particle volume fraction in the concentration polarization layer, ϕ_p is the particle volume fraction on the permeate side, D is the diffusion coefficient of the particle and x is the coordinate perpendicular to the membrane surface. Integrating over the thickness of the mass transfer boundary layer or the concentration polarization layer, δ_{cp} in Figure 1.3, yields,

$$\frac{\phi_w - \phi_p}{\phi_b - \phi_p} = \exp\left(\frac{J \cdot \delta_{cp}}{D}\right) \quad (1.2)$$

where ϕ_w is the wall concentration and ϕ_b is the bulk concentration of the particles. Rearranging Equation 1.2 gives the concentration polarization modulus,

$$\frac{\phi_w}{\phi_p} = \frac{\exp\left(\frac{J \cdot \delta_{cp}}{D}\right)}{\exp\left(\frac{J \cdot \delta_{cp}}{D}\right) - R_{mem} \cdot \left[\exp\left(\frac{J \cdot \delta_{cp}}{D}\right) - 1\right]} \quad (1.3)$$

where R_{mem} is the intrinsic retention of the membrane, defined as,

$$R_{mem} = 1 - \left(\frac{\phi_p}{\phi_w} \right) \quad (1.4)$$

The observed retention is lower than the intrinsic retention when concentration polarization exists,

$$R_{obs} = 1 - \left(\frac{\phi_p}{\phi_b} \right) \quad (1.5)$$

If the concentration polarization modulus (Equation 1.3) is unity, it means that ϕ_{wall} is equal to ϕ_{bulk} and there is no polarization. Deviation from unity indicates the presence of concentration polarization. The term $(J \cdot \delta_{cp}/D)$ in Equation 1.3 is the Peclet number, which is the ratio of the convective transport to the diffusive transport in the membrane boundary layer. The modulus depends on the Peclet number and the intrinsic retention of the membrane. Increasing the Peclet number by increasing the permeate flux, J , or the mass transfer boundary layer thickness, δ , or by decreasing the diffusion coefficient of the retained component, D , increase the value of the modulus. Similarly, increasing the retention, R_{mem} , also increases the modulus. For a given feed (fixed D) and membrane (fixed R_{mem}), to obtain the required permeate flux, the remaining adjustable parameter is the mass transfer boundary layer thickness, δ_{cp} . The boundary layer thickness can be reduced by increasing the cross-flow velocity and by promoting turbulence near the membrane surface as will be explained in more detail in the section on fouling mitigation.

Concentration polarization is a reversible phenomenon, such that the concentration gradient disappears when permeation ceases. However, it can lead to fouling if the balance between the convective drag and the back diffusion is broken in favor of the convective drag (Figure 1.3). Often, when a critical wall concentration is exceeded particles coagulate as a compact cake or gel layer on the membrane surface, and the thickness of this layer increases as filtration continues. Apart from the fouling on the membrane surface as gel or cake deposition, the foulants can also adsorb in the membrane pores. In the most general sense, the adsorption and/or deposition of solutes or particles on the surface and in the pores of the membrane is called membrane fouling [1, 31]. Membrane fouling not only increases the resistance of the membrane

to filtration, but also can deteriorate the membrane performance irreversibly.

The permeate flux through the membrane can be described by Darcy's law as,

$$J = \frac{\Delta P}{\eta R} \quad (1.6)$$

where ΔP is the pressure gradient across the membrane, which is often expressed as the transmembrane pressure difference (TMP), η is the viscosity and R is the total resistance to filtration. This total resistance can be expressed as the summation of various contributions.

$$R = R_{mem} + R_{cp} + R_f \quad (1.7)$$

where R_{mem} is the intrinsic membrane resistance, R_{cp} is the resistance due to concentration polarization and R_f is the resistance due to fouling. R_f can be further divided into reversible and irreversible fouling resistances.

1.2.2.1 Fouling characterization

The presence of concentration polarization results in a lower permeability for the feed solution compared to the pure water permeability. In other words, the resistance of the membrane to filtration is higher than the intrinsic membrane resistance. Fouling further increases the resistance. In a constant-flux filtration, particle deposition causes a continuous increase in transmembrane pressure necessary to maintain the permeate flux. In a constant pressure filtration, the flux will decline in a similar manner. However, when it declines to a flux low enough, equilibrium between convective transport towards the membrane, $J\phi$, and back diffusion, $D(d\phi/dx)$, will be reached.

In recent years, the critical flux concept has been used increasingly to characterize fouling in cross-flow and dead-end operations as well as in membrane bioreactors [32–35]. The critical flux was identified for the first time in cross-flow filtration of colloids as the flux below which no fouling occurs [36, 37]. Bacchin et al. explained the existence of the critical flux by modeling the mass flux of the particles towards the membrane, taking into account the permeation and cross-flow velocities, diffusion of the particles and surface interactions between the particles [38]. Under the forces mentioned, the critical flux is the flux at which the repulsive surface interactions are

overcome by the net flux of particles towards the membrane surface, which leads to coagulation of the particles into a cake or gel layer [32, 39]. In this sense, it can also be described as the transition point from concentration polarization to particle deposition [32, 40].

During dead-end filtrations, the definition of critical flux is slightly different. As there is no cross-flow, for reasonable values of permeate fluxes the back diffusion and surface interactions are quickly overcome by the permeate drag. In this case, it has been shown that there exists a critical flux for a given permeate volume, or a critical permeate volume for a given flux above which particles coagulate [41, 42]. In dead-end filtrations, whether or not the critical flux is reached is determined by doing rinses or backwashes between filtrations of constant filtrate volume. The membrane resistances before and after the backwash/rinse are compared to assess the reversibility of fouling [34, 43].

The analysis of flux-TMP behavior and membrane autopsies can give important information about the fouling process. In addition to these, real-time monitoring of filtration can provide further insight into fouling phenomena [44]. Here, two of these techniques which are used in this thesis are introduced.

Direct observation

Direct observation techniques employ a camera or microscope to observe the particle deposition on the membrane surface. Direct observation through the membrane (DOTM) technique uses anodised aluminum membranes. These membranes have high porosity and straight through pores which makes them transparent while wet and allows observation from the permeate side. The deposition of micron sized yeast and latex particles as well as submicron bacteria has been observed with DOTM [45–47]. Similarly, placing the lens on the feed side, it is possible to observe the surface of nontransparent membranes [48, 49]. The effects of particle size [45, 47, 50, 51], membrane surface properties [52], solution chemistry [48, 50] and cross-flow velocity [45, 48] on the particle deposition rates have been observed using these techniques. Flux-stepping was used to determine the critical flux for particle deposition. Trends obtained from flux-TMP relationships were confirmed, as the critical flux was observed to increase with increasing particle size, cross-flow velocity and zeta potential. Removal of deposited yeast particles by cross-flow and backwashing was also studied by direct observation [49, 53]. The flux recovery after backwashing was found to increase with

increasing backpulse pressure, duration and shear rate. At high backpulse pressure and shear rates, short and frequent backpulses were found to be more effective than long and fewer backpulses. At low pressure and shear rates, foulant was more effectively removed by longer backpulses since short backpulses are not strong enough to move the foulant [53]. Marselina et al. observed the cake deposition on hollow fibers by focusing on the edge of a hollow fiber during filtration, and obtained information on cake growth, distinguishing compact and loose regions of the cake layer as well as the removal of the cake by baskwashing and by cross-flow [54].

Nuclear Magnetic Resonance (NMR) imaging

NMR involves the excitation and relaxation of protons in a specimen under the influence of an external magnetic field. NMR imaging can be used for determining flow profiles and the real-time visualization of concentration polarization and cake layer formation in membrane filtrations [44]. Velocity distributions in the shell and lumen sides of hollow fiber membrane modules were observed by this technique [55–58]. Flow maldistribution in hemodialysis modules was illustrated and it was shown that the distribution can be improved by using textile yarns as spacers in the shell side [56]. The occurrence of Dean vortices in curved slits and ducts were visualized and compared to theoretical predictions and numerical simulations [59, 60].

The formation of the concentration polarization layers during the filtration of silica suspensions was observed by making use of the altered nuclear spin relaxation times (T_1 and T_2) of water protons surrounding the silica particles [61]. Similarly, by using chemical-shift imaging during the filtration of an oil-water emulsion, the oil polarization layer was visualized [62, 63]. The movement of the polarized layer in the axial direction was illustrated for both feeds [61, 63]. While mostly hollow fiber modules were used for NMR imaging studies, Graf von der Schulenburg et al. observed biofouling in spiral-wound modules [64]. Velocity heterogeneities arising with biofilm formation were visualized.

1.2.2.2 Fouling mitigation

There are two distinct approaches to mitigate membrane fouling. One approach is to modify the surface of the membrane, such that solutes or particles do not adsorb. It is generally observed that hydrophilic surfaces are more resistant towards adsorption of

the majority of potential foulants such as proteins, polysaccharides and other organic molecules, which have hydrophobic surfaces themselves [20, 21]. The methods used to incorporate hydrophilicity on membrane surfaces are the adsorption, coating, reaction or grafting of a hydrophilic material on the base membrane surface after membrane preparation or blending a hydrophilic polymer in the polymer solution before phase separation [20, 65].

Another approach is to modify the hydrodynamics around the membrane surface, in order to increase particle back transport and decrease concentration polarization. This can be done by increasing the shear rate near the membrane surface and by creating flow instabilities or vortices. The simplest way of increasing shear rate is to flow the feed solution tangentially to the membrane surface (cross-flow filtration) as opposed to dead-end filtration where all of the feed is filtered through the membrane. While laminar flow decreases concentration polarization to some extent, turbulent flow is more effective. In addition to conventional cross-flow, shear rate on the membrane surface can also be increased by using high-shear devices such as rotating disk, rotating membrane or vibrating membrane modules [66]. Although these methods of creating high shear rates to decrease concentration polarization are very effective, they are quite energy-intensive.

Pulsatile flow [67], turbulence promoters [68–70], corrugated membranes [71–76], two-phase flow [77] and centrifugal flow instabilities [59, 60, 66, 78–80] are some of the less energy-intensive ways of enhancing liquid mixing near the membrane surface. These methods create flow instabilities or vortices, which can disrupt the concentration polarization layer.

Pulsatile flow involves periodic pressure and flow rate variations on the membrane surface and has been shown to increase mass transfer coefficients and reduce concentration polarization significantly [67]. Turbulence promoters such as straight or helical rods and Kenics static mixers inserted in membrane channels promote secondary flows and increase shear rate [68–70]. In spiral wound modules the spacers between the membranes also act as turbulence promoters [81]. In corrugated membranes, the corrugations act as turbulence promoting inserts on the membrane surface and cause the formation of vortices around the corrugations when the feed flow is tangential to the membrane surface. A more detailed summary on the literature on corrugated and microstructured membranes will be given in the next section.

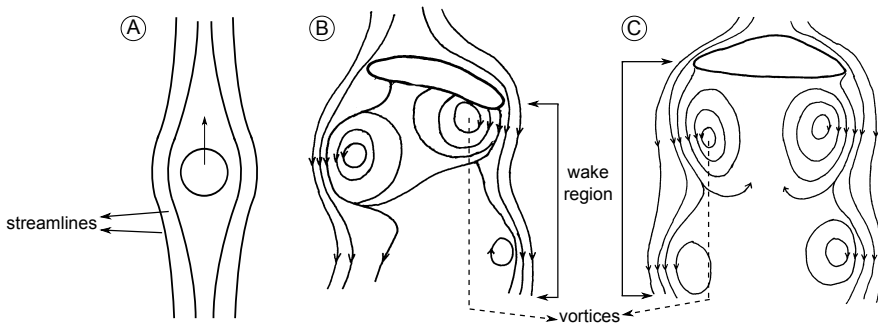


Figure 1.4: (a) Small, spherical bubbles without a wake region (b) Ellipsoidal shaped bubbles with helical vortex wakes (c) Spherical-cap shaped bubbles with symmetric vortex rings [77, 82].

Two-phase flow, i.e. addition of solid particles or gas bubbles in the feed, can create additional shear and flow instability by the vortices formed behind the particles or bubbles. Gas-liquid flow is more preferable than solid-liquid flow, since solid particles may damage the membrane surface and require a solid-liquid removal stage. Also, with the development of membrane bioreactors (MBRs), there has been increased interest in using gas bubbles in membrane processes. In the MBR process, the air bubbles serve multiple purposes: To provide oxygen for the microorganisms, to maintain the sludge in suspension and to decrease fouling. When a bubble is injected in a stationary fluid, it moves upward driven by buoyancy. The motion of the bubble can generate secondary flows behind the bubble, in the wake region (Figure 1.4). The presence and properties of the secondary flow depend on the bubble size and shape, which are related to the type of gas sparging, the gas flowrate used and the viscosity and density of the liquid [83]. Small, sub-millimeter sized bubbles are often spherical in shape. These bubbles move in the liquid without generating a wake region behind (Figure 1.4(a)). Ellipsoidal bubbles, which are typically 1.5-15 mm in size, create asymmetric helical vortex wakes (Figure 1.4(b)). Bubbles larger than about 15 mm have a spherical-cap shape and create symmetric ring vortices in the wake (Figure 1.4(c)). The fouling removal efficiency of bubbles depend on the cross-flow created by the bubble movement, secondary flows in the bubble wake, pressure pulsing caused by the bubble movement, the scouring action and fiber movement induced by the bubbles [77, 83].

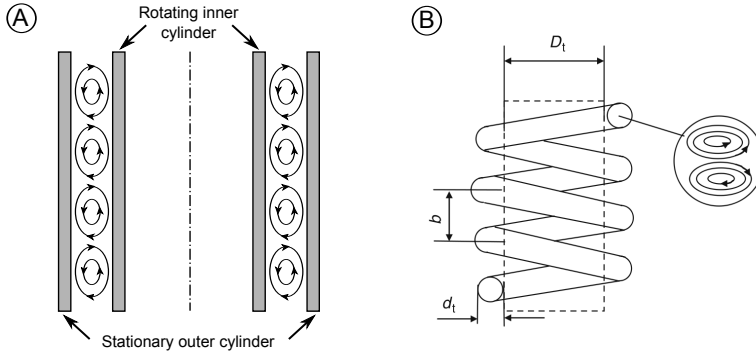


Figure 1.5: (a) Taylor vortices (b) Dean vortices

Centrifugal instabilities, such as Taylor and Dean vortices can also be used to depolarize foulant buildup near the membrane surface [59, 66, 78–80, 84]. Taylor vortices form in the fluid flowing between concentric rotating cylinders (Figure 1.5(a)), while Dean vortices form in curved ducts (Figure 1.5(b)). When a fluid is moving in a curved duct, a secondary flow is generated due to the imbalance between viscous and centrifugal forces. The intensity of the secondary flow depends on the fluid flow and the geometry of the curved channel and is characterized by the Dean number (De):

$$De = Re \sqrt{\frac{d_t}{D_t}} \quad (1.8)$$

where Re is the Reynolds number, D_t is the coil diameter and d_t is the tube diameter, as illustrated in Figure 1.5(b). For helical tubes, the coil diameter is modified to take into account the pitch, b , as:

$$D'_t = D_t \left[1 + \left(\frac{\pi}{bD_t} \right)^2 \right] \quad (1.9)$$

Dean vortices have been shown to depolarize foulant buildup during microfiltration and ultrafiltration in spiral, coiled, meander-shaped and helically twisted tubes or channels [78–80, 84].

1.3 Microstructured membranes

Structured or corrugated surfaces are quite common in heat exchangers. The corrugated surface both increases the surface area for heat transfer and disrupts the thermal boundary layer.

In membrane processes, corrugated surfaces have been used for similar reasons. Corrugations can be introduced on flat sheet membranes by a number of techniques. Mostly an originally flat membrane is pressed between dies to obtain corrugations of a few millimeters height [72–75]. Gronda et al. cast the membranes on a mold with triangle shaped corrugations [85]. Balster et al. and Peters et al. used phase separation micromolding to fabricate membranes with micrometer-sized corrugations [71, 86]. Izak et al. fabricated membranes of urethane-urea elastomers with three dimensional relief structures, by making use of the emergence of smooth features when the polymer is exposed to UV light and defined extensional stress conditions [76]. It has been shown both experimentally and theoretically that surfaces with corrugations normal to the flow direction can enhance mass transfer rates by inducing liquid mixing and disrupting the concentration polarization layer [87]. Furthermore, the membrane area-to-volume ratio is increased.

Structuring surfaces of tubular membranes or hollow fibers is less common. Broussous et al. fabricated ceramic tubular membranes with helical grooves on the inner surface by adapting the extrusion process [88, 89]. They observed significant flux improvement compared to tubular membranes with smooth walls and attributed this to the flow disturbance by the helical structure. Nijdam et al. produced polymeric hollow fibers for gas separation by phase separation microfabrication. The spinneret used contains a silicon insert with a microstructured opening in the middle, which transfers its shape to the polymer solution and finally to the membrane upon solidification [90]. They observed increased gas permeability, which was attributed to the increased surface area. In this thesis, we use the same method in the fabrication of hollow fibers for ultrafiltration, with microstructured surfaces on the shell side (Chapter 2) and on the bore side (Chapter 6).

1.4 Microsieves

Microsieves are special microfiltration membranes with straight-through pores of well-defined size, which can provide very specific separation performance and high fluxes. Microsieves can be made via different techniques from inorganic and organic materials. Inorganic microsieves are made of silicon-based materials via lithographic techniques. Microsieves with pores larger than 1 μm can be fabricated using standard mask lithography, while laser interference lithography is used to form submicron pores [91].

The main drawback of inorganic microsieves is the elaborate and expensive fabrication route. On the other hand, polymeric microsieves can be fabricated at lower costs. Several different routes have been reported to prepare polymeric microsieves. One approach is to take an existing polymer film and form pores through it. Track etching is one of these routes, which is based on irradiation of a polymeric material with fragments from the fission of heavy nuclei such as californium or uranium, or with ion beams from accelerators. The irradiation forms tracks in the polymer layer, which are later etched to form the membrane pores [92]. Polymeric nano- and microsieves can also be produced via interference holography [93].

The use of spherical templates to form pores in polymers has been reported by several research groups [94–97]. Hydrophobized silica colloids [97], glass beads [94], polystyrene microspheres [96] and water-based sessile drops [95] are examples of pore formers used, which were later removed by etching or dissolving.

Another approach is to deposit a polymer solution on a substrate with pillars, which stick through the solution and form the pores after formation of the polymer film. Yan et al. formed pillar arrays of ZnO and polystyrene on selected substrates and deposited polysulfone or nylon 6/6 solutions which were solidified via solvent evaporation [98]. The pillars were then selectively removed by etching in acid or dissolving in a solvent. Phase separation microfabrication (PS μ F) uses a similar approach to fabricate polymeric microsieves [99, 100]. The polymer solution containing a volatile additive is cast on a silicon mold with pillars. The volatile additive is evaporated after casting to ensure that the pillars of the mold perforate the polymer solution. Upon phase separation, the perforations made by the pillars form the pores of the

microsieve. The technique can be used with any polymer that can be phase separated in a nonsolvent.

1.5 Scope of the thesis

The main focus of this thesis is the fabrication, characterization and filtration behavior of microstructured membranes produced by phase separation microfabrication (PS μ F).

Chapter 2 describes the fabrication of hollow fiber membranes with a microstructured outer surface. Fabrication parameters such as the air gap, take-up speed, polymer dope viscosity and coagulation value were varied in order to observe their effects on the fiber microstructure. The fibers were characterized with respect to their permeability, pore size distribution, molecular weight cut-off and skin layer thickness and compared to round fibers fabricated under the same conditions.

In **Chapter 3** these microstructured membranes were tested in dead-end filtrations. Flux-stepping experiments were done to evaluate the fouling reversibility during filtrations of colloidal silica and sodium alginate. NMR imaging was used to visualize silica deposition on the membranes.

In **Chapter 4**, the microstructured fibers were tested in cross-flow filtrations and their performance is compared to round fibers. Additionally, in separate modules, the structured fibers were twisted around their own axes to see the effect of helical grooves under cross-flow. The critical fluxes for the onset of particle deposition and for the onset of irreversible deposition were determined in flux-cycling experiments using colloidal silica and yeast suspensions as feed solutions. Direct visual observation was used to monitor the deposition of yeast particles on the surface of the membranes.

In **Chapter 5**, the structured, round and twisted fibers were compared in submerged filtrations with aeration using colloidal silica as a model foulant. Effects of aeration rate, module orientation and bubble size were investigated.

Chapter 6 describes the fabrication of hollow fibers with microstructured surfaces on the bore side. Fabrication parameters such as the polymer dope flowrate, bore liquid flowrate, air gap and take-up speed were varied in order to observe their effects on the

fiber microstructure and properties. The fibers were characterized and compared to inner-skinned round fibers with respect to their permeability, pore size distribution and skin layer thickness.

Chapter 7 is on polymeric microsieves made by phase separation microfabrication. The first part describes the downscaling of the perforation size by shrinking the microsieves in acetone and acetone-NMP mixtures. In the second part the influence of mold design on the release of the microsieves from the molds is investigated. Molds were designed with different pillar spacings, densities, shapes and arrangements and the peeling forces were measured.

Finally **Chapter 8** presents a summary of the main conclusions of the thesis followed by an outlook and suggestions for future work on microstructured membranes.

1.6 References

- [1] R.W. Baker; *Membrane Technology and Applications* (2004); John Wiley and Sons
- [2] H. Strathmann and K. Kock; *The formation mechanism of phase inversion membranes*; *Desalination* **21** (3) (1977) 241–255
- [3] K. Kimmerle and H. Strathmann; *Analysis of the structure-determining process of phase inversion membranes*; *Desalination* **79** (2-3) (1990) 283–302
- [4] P.S.T. Machado, A.C. Habert and C.P. Borges; *Membrane formation mechanism based on precipitation kinetics and membrane morphology: Flat and hollow fiber polysulfone membranes*; *Journal of Membrane Science* **155** (2) (1999) 171–183
- [5] P. van de Witte, P.J. Dijkstra, J.W.A. van den Berg and J. Feijen; *Phase separation processes in polymer solutions in relation to membrane formation*; *Journal of Membrane Science* **117** (1-2) (1996) 1–31
- [6] M. Panar, H.H. Hoehn and R.R. Hebert; *The nature of asymmetry in reverse osmosis membranes*; *Macromolecules* **6** (5) (1973) 777–780
- [7] R.E. Kesting; *Four tiers of structure integrally skinned phase inversion membranes and their relevance to the various separation regimes*; *Journal of Applied Polymer Science* **41** (11-12) (1990) 2739–2752

- [8] R.J. Ray, W.B. Krantz and R.L. Sani; *Linear stability theory model for finger formation in asymmetric membranes*; Journal of Membrane Science **23** (2) (1985) 155–182
- [9] A. Akthakul, W.F. McDonald and A.M. Mayes; *Noncircular pores on the surface of asymmetric polymer membranes: Evidence of pore formation via spinodal demixing*; Journal of Membrane Science **208** (1-2) (2002) 147–155
- [10] S.P. Nunes and T. Inoue; *Evidence for spinodal decomposition and nucleation and growth mechanisms during membrane formation*; Journal of Membrane Science **111** (1) (1996) 93–103
- [11] I. Pinnau and W.J. Koros; *Qualitative skin layer formation mechanism for membranes made by dry/wet phase inversion*; Journal of Polymer Science, Part B: Polymer Physics **31** (4) (1993) 419–427
- [12] I.M. Wienk, R.M. Boom, M.A.A. Beerlage, A.M.W. Bulte, C.A. Smolders and H. Strathmann; *Recent advances in the formation of phase inversion membranes made from amorphous or semi-crystalline polymers*; Journal of Membrane Science **113** (2) (1996) 361–371
- [13] J.W. Cahn; *Phase separation by spinodal decomposition in isotropic systems*; The Journal of Chemical Physics **42** (1) (1965) 93–99
- [14] I.M. Wienk, T. van den Boomgaard and C.A. Smolders; *Formation of nodular structures in the top layer of ultrafiltration membranes*; Journal of Applied Polymer Science **53** (8) (1994) 1011–1023
- [15] R.M. Boom, I.M. Wienk, T. van den Boomgaard and C.A. Smolders; *Microstructures in phase inversion membranes. Part 2. The role of a polymeric additive*; Journal of Membrane Science **73** (2-3) (1992) 277–292
- [16] R.M. Boom; *Membrane formation by immersion precipitation: The role of a polymeric additive*; Ph.D. thesis; University of Twente (1992)
- [17] H. Matsuyama, K. Nakagawa, T. Maki and M. Teramoto; *Studies on phase separation rate in porous polyimide membrane formation by immersion precipitation*; Journal of Applied Polymer Science **90** (1) (2003) 292–296
- [18] A.J. Reuvers and C.A. Smolders; *Formation of membranes by means of immersion precipitation. Part II. The mechanism of formation of membranes prepared from the system cellulose acetate-acetone-water*; Journal of Membrane Science **34** (1) (1987) 67–86
- [19] Y. Liu, G.H. Koops and H. Strathmann; *Characterization of morphology*

- controlled polyethersulfone hollow fiber membranes by the addition of polyethylene glycol to the dope and bore liquid solution*; Journal of Membrane Science **223** (1-2) (2003) 187–199
- [20] H. Susanto and M. Ulbricht; *Characteristics, performance and stability of polyethersulfone ultrafiltration membranes prepared by phase separation method using different macromolecular additives*; Journal of Membrane Science **327** (1-2) (2009) 125–135
- [21] I.M. Wienk, F.H.A. Olde Scholtenhuis, T. van den Boomgaard and C.A. Smolders; *Spinning of hollow fiber ultrafiltration membranes from a polymer blend*; Journal of Membrane Science **106** (3) (1995) 233–243
- [22] T. Buer and J. Cumin; *MBR module design and operation*; Desalination **250** (3) (2010) 1073–1077
- [23] S. Nakao; *Determination of pore size and pore size distribution. 3. Filtration membranes*; Journal of Membrane Science **96** (1-2) (1994) 131–165
- [24] F. Cuperus, D. Bargeman and C. Smolders; *Critical points in the analysis of membrane pore structures by thermoporometry*; Journal of Membrane Science **66** (1) (1992) 45–53
- [25] F.P. Cuperus, D. Bargeman and C.A. Smolders; *Permporometry. The determination of the size distribution of active pores in UF membranes*; Journal of Membrane Science **71** (1-2) (1992) 57–67
- [26] A. Hernandez, J.I. Calvo, P. Pradanos and F. Tejerina; *Pore size distributions in microporous membranes. A critical analysis of the bubble point extended method*; Journal of Membrane Science **112** (1) (1996) 1–12
- [27] A. Mey-Marom and M.G. Katz; *Measurement of active pore size distribution of microporous membranes - a new approach*; Journal of Membrane Science **27** (2) (1986) 119–130
- [28] H. Vivier, M.-N. Pons and J.-F. Portala; *Study of microporous membrane structure by image analysis*; Journal of Membrane Science **46** (1) (1989) 81–91
- [29] S. Platt, M. Mauramo, S. Butylina and M. Nyström; *Retention of pegs in cross-flow ultrafiltration through membranes*; Desalination **149** (1-3) (2002) 417–422
- [30] L.J. Zeman and A.L. Zydney; *Microfiltration and Ultrafiltration - Principles and Applications* (1996); Marcel Dekker
- [31] G. Belfort, R.H. Davis and A.L. Zydney; *The behavior of suspensions and macromolecular solutions in crossflow microfiltration*; Journal of Membrane

- Science **96** (1-2) (1994) 1–58
- [32] P. Bacchin, P. Aimar and R.W. Field; *Critical and sustainable fluxes: Theory, experiments and applications*; Journal of Membrane Science **281** (1-2) (2006) 42–69
- [33] P. Le-Clech, V. Chen and A.G. Fane; *Fouling in membrane bioreactors used in wastewater treatment*; Journal of Membrane Science **284** (1-2) (2006) 17–53
- [34] W.J.C. Van de Ven; *Towards Optimal Saving in Membrane Operation: The development of process inspection and feedwater characterization tools*; Ph.D. thesis; University of Twente (2008)
- [35] W.J.C. van de Ven, K. van Sant, I.G.M. Pünt, A. Zwijnenburg, A.J.B. Kemperman, W.G.J. van der Meer and M. Wessling; *Hollow fiber dead-end ultrafiltration: Influence of ionic environment on filtration of alginates*; Journal of Membrane Science **308** (1-2) (2008) 218–229
- [36] R.W. Field, D. Wu, J.A. Howell and B.B. Gupta; *Critical flux concept for microfiltration fouling*; Journal of Membrane Science **100** (3) (1995) 259–272
- [37] J.A. Howell; *Sub-critical flux operation of microfiltration*; Journal of Membrane Science **107** (1-2) (1995) 165–171
- [38] P. Bacchin, P. Aimar and V. Sanchez; *Model for colloidal fouling of membranes*; AIChE Journal **41** (2) (1995) 368–376
- [39] P. Bacchin, D. Si-Hassen, V. Starov, M.J. Clifton and P. Aimar; *A unifying model for concentration polarization, gel-layer formation and particle deposition in cross-flow membrane filtration of colloidal suspensions*; Chemical Engineering Science **57** (1) (2002) 77–91
- [40] V. Chen, A.G. Fane, S. Madaeni and I.G. Wenten; *Particle deposition during membrane filtration of colloids: Transition between concentration polarization and cake formation*; Journal of Membrane Science **125** (1) (1997) 109–122
- [41] P. Harmant and P. Aimar; *Coagulation of Colloids Retained by Porous Wall*; AIChE Journal **42** (12) (1996) 3523–3532
- [42] D.N. Petsev, V.M. Starov and I.B. Ivanov; *Concentrated dispersions of charged colloidal particles: Sedimentation, ultrafiltration and diffusion*; Colloids and Surfaces A: Physicochemical and Engineering Aspects **81** (C) (1993) 65–81
- [43] Y. Bessiere, N. Abidine and P. Bacchin; *Low fouling conditions in dead-end filtration: Evidence for a critical filtered volume and interpretation using critical osmotic pressure*; Journal of Membrane Science **264** (1-2) (2005) 37–47

- [44] V. Chen, H. Li and A.G. Fane; *Non-invasive observation of synthetic membrane processes - A review of methods*; Journal of Membrane Science **241** (1) (2004) 23–44
- [45] H. Li, A.G. Fane, H.G.L. Coster and S. Vigneswaran; *Direct observation of particle deposition on the membrane surface during crossflow microfiltration*; Journal of Membrane Science **149** (1) (1998) 83–97
- [46] H. Li, A.G. Fane, H.G.L. Coster and S. Vigneswaran; *Observation of deposition and removal behaviour of submicron bacteria on the membrane surface during crossflow microfiltration*; Journal of Membrane Science **217** (1-2) (2003) 29–41
- [47] Y.P. Zhang, A.G. Fane and A.W.K. Law; *Critical flux and particle deposition of fractal flocs during crossflow microfiltration*; Journal of Membrane Science **353** (1-2) (2010) 28–35
- [48] S.-T. Kang, A. Subramani, E.M.W. Hoek, M.A. Deshusses and M.R. Matsumoto; *Direct observation of biofouling in cross-flow microfiltration: Mechanisms of deposition and release*; Journal of Membrane Science **244** (1-2) (2004) 151–165
- [49] W.D. Mores and R.H. Davis; *Direct visual observation of yeast deposition and removal during microfiltration*; Journal of Membrane Science **189** (2) (2001) 217–230
- [50] J.S. Knutson and R.H. Davis; *Deposition of foulant particles during tangential flow filtration*; Journal of Membrane Science **271** (1-2) (2006) 101–113
- [51] H. Li, A.G. Fane, H.G.L. Coster and S. Vigneswaran; *An assessment of depolarisation models of crossflow microfiltration by direct observation through the membrane*; Journal of Membrane Science **172** (1-2) (2000) 135–147
- [52] S. Kang, E.M.V. Hoek, H. Choi and H. Shin; *Effect of membrane surface properties during the fast evaluation of cell attachment*; Separation Science and Technology **41** (7) (2006) 1475–1487
- [53] W.D. Mores and R.H. Davis; *Yeast foulant removal by backpulses in crossflow microfiltration*; Journal of Membrane Science **208** (1-2) (2002) 389–404
- [54] Y. Marselina, Lifia, P. Le-Clech, R.M. Stuetz and V. Chen; *Characterisation of membrane fouling deposition and removal by direct observation technique*; Journal of Membrane Science **341** (1-2) (2009) 163–171
- [55] P.A. Hardy, C.K. Poh, Z. Liao, W.R. Clark and D. Gao; *The use of magnetic resonance imaging to measure the local ultrafiltration rate in hemodialyzers*; Journal of Membrane Science **204** (1-2) (2002) 195–205

- [56] S. Laukemper-Ostendorf, H.D. Lemke, P. Bluemler and B. Bluemich; *NMR imaging of flow in hollow fiber hemodialyzers*; Journal of Membrane Science **138** (2) (1998) 287–295
- [57] C.K. Poh, P.A. Hardy, Z. Liao, Z. Huang, W.R. Clark and D. Gao; *Effect of flow baffles on the dialysate flow distribution of hollow-fiber hemodialyzers: A noninvasive experimental study using MRI*; Journal of Biomechanical Engineering **125** (4) (2003) 481–489
- [58] S. Yao, M. Costello, A.G. Fane and J.M. Pope; *Non-invasive observation of flow profiles and polarisation layers in hollow fibre membrane filtration modules using NMR micro-imaging*; Journal of Membrane Science **99** (3) (1995) 207–216
- [59] K.Y. Chung, W.A. Edelstein and G. Belfort; *Dean vortices with wall flux in a curved channel membrane system. 6. Two dimensional magnetic resonance imaging of the velocity field in a curved impermeable slit*; Journal of Membrane Science **81** (1-2) (1993) 151–162
- [60] H. Mallubhotla, G. Belfort, W.A. Edelstein and T.A. Early; *Dean vortex stability using magnetic resonance flow imaging and numerical analysis*; AIChE Journal **47** (5) (2001) 1126–1140
- [61] D. Airey, S. Yao, J. Wu, V. Chen, A.G. Fane and J.M. Pope; *An investigation of concentration polarization phenomena in membrane filtration of colloidal silica suspensions by NMR micro-imaging*; Journal of Membrane Science **145** (2) (1998) 145–158
- [62] J.M. Pope, S. Yao and A.G. Fane; *Quantitative measurements of the concentration polarisation layer thickness in membrane filtration of oil-water emulsions using NMR micro-imaging*; Journal of Membrane Science **118** (2) (1996) 247–257
- [63] S. Yao, A.G. Fane and J.M. Pope; *An investigation of the fluidity of concentration polarisation layers in crossflow membrane filtration of an oil-water emulsion using chemical shift selective flow imaging*; Magnetic Resonance Imaging **15** (2) (1997) 235–242
- [64] D.A. Graf von der Schulenburg, J.S. Vrouwenvelder, S.A. Creber, M.C.M. van Loosdrecht and M.L. Johns; *Nuclear magnetic resonance microscopy studies of membrane biofouling*; Journal of Membrane Science **323** (1) (2008) 37–44
- [65] D. Rana and T. Matsuura; *Surface modifications for antifouling membranes*; Chemical Reviews **110** (4) (2010) 2448–2471

- [66] K.H. Kroner and V. Nissinen; *Dynamic filtration of microbial suspensions using an axially rotating filter*; Journal of Membrane Science **36** (C) (1988) 85–100
- [67] H.-Y. Li, C.D. Bertram and D.E. Wiley; *Mechanisms by which pulsatile flow affects cross-flow microfiltration*; AIChE Journal **44** (9) (1998) 1950–1961
- [68] D.M. Krstic, M.N. Tekic, M.D. Caric and S.D. Milanovic; *The effect of turbulence promoter on cross-flow microfiltration of skim milk*; Journal of Membrane Science **208** (1-2) (2002) 303–314
- [69] B.B. Gupta, J.A. Howell, D. Wu and R.W. Field; *A helical baffle for cross-flow microfiltration*; Journal of Membrane Science **102** (1-3) (1995) 31–42
- [70] S. Pal, R. Bharihoke, S. Chakraborty, S.K. Ghatak, S. De and S. DasGupta; *An experimental and theoretical analysis of turbulence promoter assisted ultrafiltration of synthetic fruit juice*; Separation and Purification Technology **62** (3) (2008) 659–667
- [71] J. Balster, M.H. Yildirim, D.F. Stamatialis, R. Ibanez, R.G.H. Lammertink, V. Jordan and M. Wessling; *Morphology and microtopology of cation-exchange polymers and the origin of the overlimiting current*; Journal of Physical Chemistry B **111** (9) (2007) 2152–2165
- [72] K. Scott, A.J. Mahmood, R.J. Jachuck and B. Hu; *Intensified membrane filtration with corrugated membranes*; Journal of Membrane Science **173** (1) (2000) 1–16
- [73] N. Tzanetakis, K. Scott, W.M. Taama and R.J.J. Jachuck; *Mass transfer characteristics of corrugated surfaces*; Applied Thermal Engineering **24** (13) (2004) 1865–1875
- [74] M.J. van der Waal and I.G. Racz; *Mass transfer in corrugated-plate membrane modules. I. Hyperfiltration experiments*; Journal of Membrane Science **40** (2) (1989) 243–260
- [75] M.J. van der Waal, S. Stevanovic and I.G. Racz; *Mass transfer in corrugated-plate membrane modules. II. Ultrafiltration experiments*; Journal of Membrane Science **40** (2) (1989) 261–275
- [76] P. Izak, M.H. Godinho, P. Brogueira, J.L. Figueirinhas and J.G. Crespo; *3D topography design of membranes for enhanced mass transport*; Journal of Membrane Science **321** (2) (2008) 337–343
- [77] Z.F. Cui, S. Chang and A.G. Fane; *The use of gas bubbling to enhance membrane processes*; Journal of Membrane Science **221** (1-2) (2003) 1–35
- [78] M.E. Brewster, K.-Y. Chung and G. Belfort; *Dean vortices with wall flux in*

- a curved channel membrane system. 1. A new approach to membrane module design*; Journal of Membrane Science **81** (1-2) (1993) 127–137
- [79] J.N. Ghogomu, C. Guigui, J.C. Rouch, M.J. Clifton and P. Aptel; *Hollow-fibre membrane module design: Comparison of different curved geometries with Dean vortices*; Journal of Membrane Science **181** (1) (2001) 71–80
- [80] H. Mallubhotla, S. Hoffmann, M. Schmidt, J. Vente and G. Belfort; *Flux enhancement during dean vortex tubular membrane nanofiltration. 10. Design, construction and system characterization*; Journal of Membrane Science **141** (2) (1998) 183–195
- [81] F. Li, W. Meindersma, A.B. de Haan and T. Reith; *Optimization of commercial net spacers in spiral wound membrane modules*; Journal of Membrane Science **208** (1-2) (2002) 289–302
- [82] T. Miyahara, K. Tsuchiya and L.-S. Fan; *Wake properties of a single gas bubble in three-dimensional liquid-solid fluidized bed*; International Journal of Multiphase Flow **14** (6) (1988) 749–763
- [83] L. Fan and K. Tsuchiya; *Bubble wake dynamics in liquids and liquid-solid suspensions* (1990); Butterworth
- [84] H. Mallubhotla, E. Nunes and G. Belfort; *Microfiltration of yeast suspensions with self-cleaning spiral vortices: Possibilities for a new membrane module design*; Biotechnology and Bioengineering **48** (4) (1995) 375–385
- [85] A.M. Gronda, S. Buechel and E.L. Cussler; *Mass transfer in corrugated membranes*; Journal of Membrane Science **165** (2) (2000) 177–187
- [86] A.M. Peters, R.G.H. Lammertink and M. Wessling; *Comparing flat and micro-patterned surfaces: Gas permeation and tensile stress measurements*; Journal of Membrane Science **320** (1-2) (2008) 173–178
- [87] L.-Z. Zhang; *Convective mass transport in cross-corrugated membrane exchangers*; Journal of Membrane Science **260** (1-2) (2005) 75–83
- [88] L. Broussous, J.C. Ruiz, A. Larbot and L. Cot; *Stamped ceramic porous tubes for tangential filtration*; Separation and Purification Technology **14** (1-3) (1998) 53–57
- [89] L. Broussous, P. Schmitz, H. Boisson, E. Prouzet and A. Larbot; *Hydrodynamic aspects of filtration antifouling by helically corrugated membranes*; Chemical Engineering Science **55** (21) (2000) 5049–5057
- [90] W. Nijdam, J. de Jong, C.J.M. van Rijn, T. Visser, L. Versteeg, G. Kapantaidakis,

- G.H. Koops and M. Wessling; *High performance micro-engineered hollow fiber membranes by smart spinneret design*; Journal of Membrane Science **256** (1-2) (2005) 209–215
- [91] S. Kuiper, C.J.M. van Rijn, W. Nijdam and M.C. Elwenspoek; *Development and applications of very high flux microfiltration membranes*; Journal of Membrane Science **150** (1) (1998) 1–8
- [92] P. Apel; *Track etching technique in membrane technology*; Radiation Measurements **34** (1-6) (2001) 559–566
- [93] A.M. Prenen, J.C.A.H. van der Werf, C.W.M. Bastiaansen and D.J. Broer; *Monodisperse, polymeric nano- and microsieves produced with interference holography*; Advanced Materials **21** (17) (2009) 1751–1755
- [94] C. Greiser, S. Ebert and W.A. Goedel; *Using breath figure patterns on structured substrates for the preparation of hierarchically structured microsieves*; Langmuir **24** (3) (2008) 617–620
- [95] S.F. Jahn, L. Engisch, R.R. Baumann, S. Ebert and W.A. Goedel; *Polymer microsieves manufactured by inkjet technology*; Langmuir **25** (1) (2009) 606–610
- [96] J. Li and Y. Zhang; *Porous polymer films with size-tunable surface pores*; Chemistry of Materials **19** (10) (2007) 2581–2584
- [97] H. Xu and W.A. Goedel; *Polymer-silica hybrid monolayers as precursors for ultrathin free-standing porous membranes*; Langmuir **18** (6) (2002) 2363–2367
- [98] X. Yan, G. Liu, M. Dickey and C.G. Willson; *Preparation of porous polymer membranes using nano- or micro-pillar arrays as templates*; Polymer **45** (25) (2004) 8469–8474
- [99] M. Girones, I.J. Akbarsyah, W. Nijdam, C.J.M. van Rijn, H.V. Jansen, R.G.H. Lammertink and M. Wessling; *Polymeric microsieves produced by phase separation micromolding*; Journal of Membrane Science **283** (1-2) (2006) 411–424
- [100] L. Vogelaar, R.G.H. Lammertink, J.N. Barsema, W. Nijdam, L.A.M. Bolhuis-Versteeg, C.J.M. Van Rijn and M. Wessling; *Phase separation micromolding: A new generic approach for microstructuring various materials*; Small **1** (6) (2005) 645–655

CHAPTER 2

Hollow fiber membranes with microstructured outer skin

THIS CHAPTER HAS BEEN PUBLISHED:

P.Z. Çulfaz, E. Rolevink, C.J.M. van Rijn, R.G.H. Lammertink and M. Wessling, *Microstructured hollow fibers for ultrafiltration*, *Journal of Membrane Science* **347** (1-2) (2009) 32-41.

ABSTRACT

Hollow fiber ultrafiltration membranes with a corrugated outer microstructure were prepared from a PES/PVP blend. The effect of spinning parameters such as air gap, take-up speed, polymer dope viscosity and coagulation value on the microstructure and membrane characteristics was investigated. Fibers with maximum 89% surface area enhancement were prepared. The structured fibers and the round fibers spun under the same conditions had comparable (intrinsic) pure water permeability, molecular weight cut-off, pore size distribution and average skin layer thickness. This implies that the flow through the unit volume of the structured fibers will be enhanced compared to their round counterparts, while maintaining the same separation properties. A colloidal filtration method was used to determine the skin layer thickness. Structured fibers spun with a slow-coagulating polymer dope had varying skin thickness throughout the outer surface, which was dependent on the geometry of the fiber and was probably caused by varying local coagulation conditions around the structured outer surface of the fibers. A polymer dope with high coagulation value, on the other hand, resulted in a structured fiber with a homogeneous skin layer all along the surface.

2.1 Introduction

Hollow fiber membranes are commonly used in many membrane processes ranging from gas separation to microfiltration. The main advantage of this configuration over the flat sheet membranes is that it provides a high ratio of membrane area to module volume, and therefore higher productivity per membrane module. Hollow fiber membranes are produced by a spinning process in which the polymer solution is extruded through a spinneret into a nonsolvent bath. The membranes are formed via phase inversion and have an asymmetric structure with a thin separating layer on the inner surface, the outer surface or both [1, 2].

To produce a hollow fiber membrane with high permeability, usually the first approach is to optimize membrane fabrication conditions (e.g. composition, temperature and flow rates of the polymer dope and the coagulant, air gap distance, take-up speed, etc.) [2–5]. Mostly, a thin skin emerges on the surface of the hollow fiber, having the desired separation properties. The remaining part of the fiber wall has only mechanical support function. It is difficult, however highly desirable, to increase the permeability of the skin layer [6]. Here, we propose to increase the productivity of a membrane by increasing the area-to-volume ratio of the membrane using corrugated surfaces. The use of corrugated surfaces is a common approach used to enhance heat transfer in heat exchangers. In recent years, this approach has also been used in membrane applications to enhance mass transfer rates. For certain fabrication conditions, the amount of membrane area that fits a certain volume can be increased by using corrugations, thereby increasing the productivity of the membrane module.

Most of the work done so far on corrugated membranes has focused on sheet-like membranes. To prepare the membranes several approaches have been followed such as pressing originally flat sheet membranes between structured dies [7–10] and casting the polymer solution on or between structured molds of millimeter or micrometer scale corrugations [11–13]. It has been shown that corrugated membranes enhance flow by both increasing the membrane area per volume and by disrupting the concentration polarization layer.

There are fewer studies on corrugated tubular or hollow fiber membranes. Broussous et al. reported the preparation of helically corrugated ceramic tubular membranes

by adapting the extrusion process, which proved to improve the permeate flux in the microfiltration of bentonite suspensions [14, 15]. The only report of fabrication of corrugated polymeric membranes has come from our group showing hollow fiber membranes with micrometer-scale corrugations for gas separation by combining silicon micromachining technology and the conventional hollow fiber spinning process [16]. The micro-engineered spinneret that was used contains a silicon insert with a structured opening. The polymer dope flows through this structured annulus instead of a round one and takes the shape of the insert. Upon coagulation, the corrugated fiber forms. The microstructured and round fibers made in this study were shown to have similar intrinsic gas permeances, resulting in enhanced productivity in the structured fibers.

In this study we apply the same spinning method for the fabrication of microstructured hollow fibers for ultrafiltration. We report the effect of various parameters on the fiber structure and a thorough comparison of structured and round fibers spun under the same conditions with respect to their morphology and performance.

2.2 Experimental

2.2.1 Fabrication of the fibers

The hollow fibers were prepared from a PES-PVP blend. Polyether sulfone (PES) was purchased from BASF (Ultrason 6020), Polyvinyl pyrrolidone PVP K30 ($M_w \approx 40$ kDa) and PVP K90 ($M_w \approx 360$ kDa) were purchased from Fluka. All polymers were dried in vacuum at 30°C for 24 hours prior to use. The solvent, N-methyl pyrrolidone (NMP) was purchased from Acros. The water used in preparing the polymer dopes was ultrapure water (18 M Ω .cm). The polymer dopes were filtered through a 25 μ m metal filter and degassed for at least 2 days before spinning. Spinning was done at room temperature. Water was used as the external coagulant, while the bore liquid was a mixture of 3% PVP K90, 19% H₂O and 78% NMP. After spinning, the fibers were washed in water for 24 hours to complete the solvent-nonsolvent exchange. Then they were kept in a 4000 ppm NaOCl solution in water for 48 hours. This treatment was followed by rinsing in water for an hour, and then putting the fibers in a 10% glycerol solution for 24 hours, after which they were dried under ambient conditions.

Table 2.1: Fiber spinning parameters

Fiber	Polymer dope	Insert	Air gap (mm)	Polymer dope flowrate (mL/min)	Polymer dope velocity (m/min)	Bore liquid flowrate (mL/min)	Pulling speed (m/min)
S1	D1	Structured1	5	10	4.0	6	7.0
S2	D1	Structured1	12	10	4.0	6	7.0
S3	D1	Structured1	32	10	4.0	6	7.0
S4	D1	Structured1	58	10	4.0	6	7.0
S5	D2	Structured1	5	5	2.0	3	5.0
S6	D3	Structured1	5	5	2.0	3	5.0
S7	D4	Structured1	5	5	2.0	3	5.0
S8	D1	Structured2	5	5	2.7	3	3.5
S9	D1	Structured2	5	5	2.7	3	7.0
S10	D1	Structured2	5	5	2.7	3	13.0
S11	D1	Structured2	5	5	2.7	3	23.5
S12	D5	Structured1	5	5	2.0	3	5.0

The details of structured fiber spinning are described elsewhere [16]. In this study, two different structured inserts were used to spin structured fibers and a round insert was used to spin round fibers for comparison. Fibers were spun varying the air gap, the polymer dope composition and the take-up speed. The spinning parameters used in the fabrication of the structured fibers are shown in Table 2.1. The compositions of the different polymer dopes used are shown in Table 2.2. For the fibers spun with dope D1, round counterparts were also spun under the same conditions for comparison.

Table 2.2: Polymer dope properties

Dope	%PES	%PVP K30	%PVP K90	%H ₂ O	%NMP
D1	20	5	5	5	65
D2	17	5	5	5	68
D3	14	5	5	5	71
D4	14	5	5	7.5	68.5
D5	17	5	5	7.2	65.8

2.2.2 Characterization of the fibers

2.2.2.1 SEM and FESEM analysis

The structure of the fibers was examined using Scanning Electron Microscopy (JEOL JSM 5600LV). To observe the pores on the skin surface on the outer side of the fibers and the cross-sections of the skin layer, Field Emission Scanning Electron Microscopy was used (JEOL 660T). For preparing the SEM and FESEM samples, the fibers were immersed in ethanol for a few minutes and then broken in liquid nitrogen. Prior to measurement, the fibers were sputtered with gold for SEM images and with platinum for FESEM images.

The perimeter and cross-sectional area of the fibers were measured from the SEM images using ImageJ software. For assessing the enhancement in surface area of the structured fibers, the convoluted perimeter of the fiber was divided by the perimeter of a circle passing through the middle of the fins and the grooves in the fiber.

2.2.2.2 Pure Water Permeability

The pure water permeabilities of the fibers were measured using ultrapure water with modules of fibers having a length of 30 cm (ca. 70-100 cm² membrane area) and under transmembrane pressure differences of 0.5 and 1.0 bars. Three modules were prepared for each fiber batch. Before measuring the pure water permeabilities, the fibers were washed with ultrapure water in cross flow for approximately half an hour to remove the glycerol in the pores. The permeabilities reported for the structured fibers were calculated using the actual convoluted surface area. In other words, the intrinsic permeabilities of the membranes, in units of L/h.m².bar, are reported for both structured and round fibers.

2.2.2.3 Molecular Weight Cut-off

For measuring the molecular weight cut-off (MWCO) of the membranes a dextran mixture prepared using dextrans of 18 kDa, 75 kDa and 250 kDa nominal molecular weight (PDI \approx 1.5, as reported by the manufacturer) was used. The filtration was done

in cross-flow mode with cross-flow velocities of 0.7-2.0 m/s and under transmembrane pressure difference of 0.15-0.25 bar. The filtration conditions for each fiber batch tested were such that the estimated ratio J/k was smaller than 1, where J is the permeate flux and k is the estimated mass transfer coefficient in the boundary layer near the membrane surface. This choice of operating conditions minimizes concentration polarization and should yield data that is more representative of the membrane structure and independent of the filtration conditions [17, 18]. Retentate and permeate samples were taken after 30 and 60 minutes of filtration and analyzed with Gel Permeation Chromatography (GPC) to determine the retention of each molecular weight. The molecular weight of the dextran which has 90% retention was reported as the molecular weight cut-off.

2.2.2.4 Permporometry

Permporometry is a method used to characterize the size distribution of active pores in porous materials [19, 20]. The measurement protocol of Liu et al. was used to determine the pore size distribution of the hollow fibers [2].

2.2.2.5 Skin layer characterization

To characterize the skin layer of the fibers, the method first introduced by Cuperus et al. was used [21]. Uniform sized colloidal gold particles that are known to be larger than the skin layer pores were filtered from the support structure towards the skin of the membrane. In this way, the particles that cannot permeate through the pores of the skin outline the skin layer. Colloidal solutions of 10 and 20 nm gold particles were obtained from Sigma-Aldrich. Membrane modules of 3-4 cm² area were prepared and 15 mL of 25 ppm gold solution was filtered from the bore side towards the outer skin under a transmembrane pressure difference of 1.5 bar. After filtration, the membranes were dried overnight in vacuum at 30°C and then the outer surfaces were sputtered with platinum. This way, the skin layer where there is no gold was sandwiched between the accumulated gold layer before the skin and the platinum layer on the surface of the membrane. The platinum-coated membranes were fractured in liquid nitrogen in the same way as the standard SEM samples. No further coating was applied on the cross section surface of the samples which were examined in backscattered electron

image mode with the JEOL JSM 5600LV Scanning Electron Microscope under low vacuum (20-25 Pa). The backscattered electron signal depends on the atomic number of materials, and therefore yields an image with contrast between gold and platinum, which appear light, and the polymer, which appears dark in the image.

2.2.3 Characterization of the polymer dopes

2.2.3.1 Viscosity

The shear-dependent viscosity of the polymer dopes were measured with Haake Viscotester 550 and the value found by extrapolating the shear rate to zero was used as an estimate of the zero-shear viscosity.

2.2.3.2 Surface tension

The surface tension of the polymer dopes were measured with Krüss EasyDyne tensiometer using the Wilhelmy Plate method.

2.2.3.3 Cloud point and coagulation value

The cloud point of the polymer dopes were determined by preparing solutions with different water concentrations varying in steps of 0.5% water. After mixing the solutions for two days, they were checked for turbidity and the concentration between the first turbid solution and the last clear solution was estimated to be the cloud point. The coagulation value was then calculated as follows:

$$\text{Coagulation value} = \frac{\text{H}_2\text{O}_{\text{in polymer dope}}}{\text{H}_2\text{O}_{\text{at cloud point}}} \quad (2.1)$$

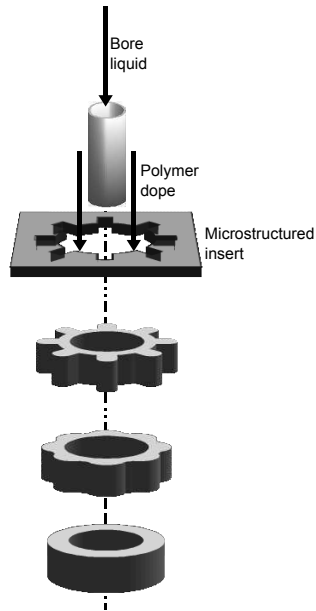


Figure 2.1: The structure evolution of the polymer solution in the air gap

2.3 Results and Discussion

2.3.1 Fiber morphology

When fibers are spun with the microstructured spinneret, the polymer solution leaves the spinneret taking the shape of the opening in the silicon insert. Before it coagulates, it first passes through the air gap and then enters the water bath where it coagulates either immediately (100% coagulation value) or with a certain delay. During this time, the initial structured shape of the polymer solution flows gradually towards a round shape, which is a process driven by the surface tension and retarded by viscous forces (Figure 2.1). Further spinning parameters that affect the amount of structure retained in the fiber are the air gap distance and the take-up speed, which determine the residence time in the air gap and the coagulation value, which determines how fast the fiber coagulates in the nonsolvent bath.

2.3.1.1 Effect of air gap distance on fiber structure

As the fiber passes through the air gap the surface energy is minimized by rounding the features, finally resulting in a totally round fiber. Figure 2.2 shows the fibers spun at different air gaps using the polymer dope D1. An increased air gap results in a longer residence time in air, the magnitude of which can be roughly estimated using the average of the velocity of the polymer solution as it exits the spinneret and the take-up velocity. With this estimation, an air gap of 5 mm corresponds to a residence time of 60 ms, and the longest air gap used, 58 mm, corresponds to a residence time of 670 ms. At an air gap of 5 mm, the surface area enhancement is calculated as 89%, which gradually diminishes as the air gap is increased to 58 mm (Table 2.3).

Table 2.3: Spinning parameters, polymer dope properties and the resulting surface area enhancement in the structured fibers

Fiber	Code	Polymer dope			Fiber perimeter (mm)	Middle circle perimeter	%Surface area enhancement	Cross-sectional area (mm ²)
		Zero-shear viscosity Pa.s	Surface tension mN/m	Coagulation value %				
S1	D1	155	41	70	8.9	4.7	89	1.08
S2	D1	155	41	70	7.8	4.9	59	1.15
S3	D1	155	41	70	6.3	5.0	27	1.33
S4	D1	155	41	70	4.8	-	-	1.16
S5	D2	63	44	65	7.6	4.4	72	0.80
S6	D3	28	46	65	5.3	4.1	31	0.76
S7	D4	28	47	95	5.2	4.3	20	0.86
S8	D1	155	41	70	7.1	4.8	47	1.31
S9	D1	155	41	70	5.6	3.5	57	1.60
S10	D1	155	41	70	4.2	2.6	60	0.31
S11	D1	155	41	70	3.1	1.9	66	0.16
S12	D5	-	-	95	7.5	4.7	60	1.05

2.3.1.2 Effect of take-up speed on fiber structure

Figure 2.3 shows the fibers spun at a constant air gap of 5 mm using different take-up speeds. This set of fibers were spun with a different insert, and for this reason have a star-shape rather than the flower-shape of the fibers in the previous and the following sections. Increasing the take-up speed decreases the residence time of the fibers in the air gap. At the same time, since the velocity of the fiber is increased, the cross-sectional area decreases, as dictated by the conservation of mass. As shown in Table 2.3, from

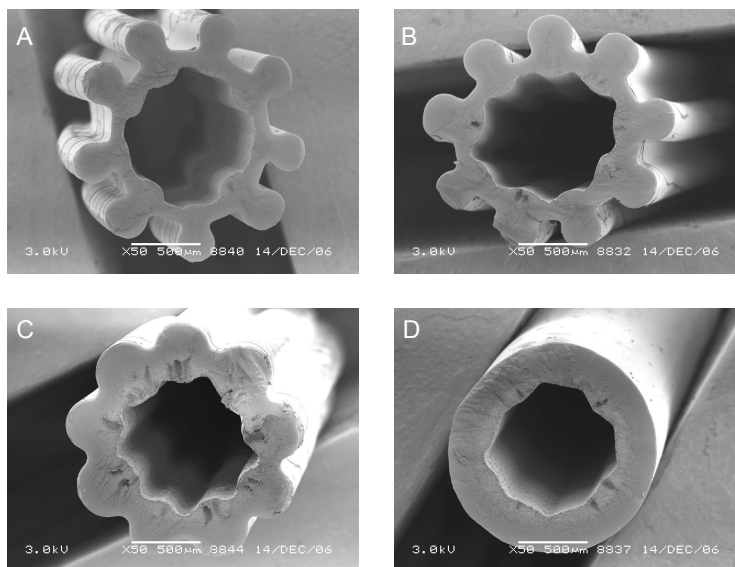


Figure 2.2: Fibers spun with dope D1, using air gaps of (a) 5, (b) 12, (c) 32 and (d) 58 mm

a take-up speed of 3.5 m/min to 23.5 m/min, the cross sectional area of the fiber decreases from 1.31 mm² to 0.16 mm², and the surface area enhancement increases from 47% to 66%.

2.3.1.3 Effect of polymer dope properties on fiber structure

There is very little variation in the surface tension of the polymer dopes that were used to prepare the membranes. This is a result of the relatively narrow range of relevant compositions to prepare ultrafiltration membranes with a chosen polymer-solvent-nonsolvent system. However, with decreasing polymer concentration, membranes of varying separation properties can be prepared and the decreasing polymer concentration decreases the viscosity significantly (Table 2.3). The decrease in viscosity speeds up the structure loss in the air gap and from dope D1 to D3 the surface area enhancement decreases from 89% to only 31% (Figure 2.4). The polymer dopes D3 and D4 have the same viscosities but different coagulation values. The increasing coagulation value of dope D4, which results in the polymer solution to coagulate faster in the water bath, however, does not improve the surface area enhancement further. The coagulation rate of similar polymer solution systems are reported to be on the order of a few seconds,

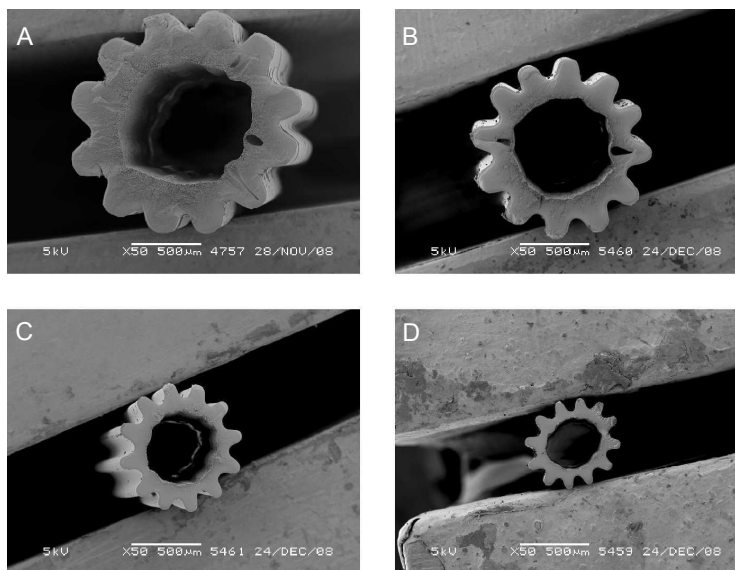


Figure 2.3: Fibers spun with dope D1, using take-up speeds of (a) 3.5, (b) 7, (c) 13 and (d) 23.5 m/min

which is comparable to the residence times in the air gap used in our study [22, 23]. The reason why decreasing the time before coagulation in the water bath does not have a significant effect on the structure loss can be that the interfacial tension between the polymer solution and water is less than that between the polymer solution and air. In water, initially the interfacial tension is about half the value of that in air. Besides, it gets smaller and smaller as the solvent-nonsolvent exchange starts taking place. As a result, it appears that the most important property of the polymer dope in determining the rate of structure loss of the fiber is the viscosity.

2.3.1.4 Scaling theory to describe the rate of structure evolution

As mentioned earlier, the driving force for the structured shape to flow towards a round shape is the surface tension associated with the different degrees of curvature in the initial shape. The surface tension that causes the polymer solution to flow is resisted by viscous forces. There are a number of studies in literature on the numerical modeling of melt spinning of noncircular fibers [24, 25]. Here we try to describe a scaling argument to estimate the rate of structure loss in the air gap and to compare

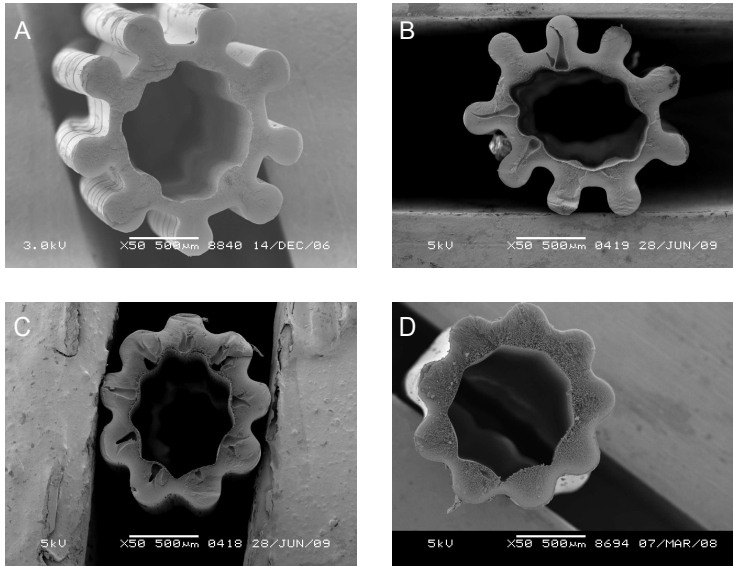


Figure 2.4: Fibers spun with dopes (a) D1, (b) D2, (c) D3 and (d) D4 using an air gap of 5 mm

the results of this scaling theory with the experimental results obtained from the fibers spun under various conditions.

As the fiber exits the spinneret, its outer shape is assumed to be the same as the shape of the structured insert in the spinneret. As it flows through the air gap this shape flows toward a more rounded shape. This final shape of the fibers is taken as the shape observed in the SEM images of the fully coagulated fibers. The change in surface energy, dE_s , of a cross section of thickness dz can be described as,

$$dE_s = \sigma dC_f dz \quad (2.2)$$

where σ is the surface tension of the polymer solution and C_f is the circumference of the cross section.

The re-flow of the structured shape of the polymer solution towards a rounded shape is laminar considering the dimensions and the approximate velocity of the surface. Therefore, inertial forces can be neglected and the change in surface energy can be considered to be compensated by viscous dissipation. The viscous dissipation (dE_v) for a unit volume dV of the fluid and per unit time dt scales with the viscosity, η and

the square of the shear rate, γ as follows;

$$dE_v \sim \eta\gamma^2 \quad (2.3)$$

where

$$\gamma \sim \frac{1}{t} \quad (2.4)$$

For a volume of $dV = dA_c dz$, where dA_c is the cross sectional area, then, the viscous dissipation during time, t , can be estimated as,

$$dE_v = \left(\frac{\eta}{t^2}\right) (dtdA_c dz) \quad (2.5)$$

Equating dE_s and dE_v gives the relation,

$$\sigma dC_f = \left(\frac{\eta}{t^2}\right) (dtdA_c) \quad (2.6)$$

For the fiber set where the take-up speed was varied, the cross sectional area of the fiber decreases up to tenfold from the initial area at the high take-up speeds used. Therefore, for this set, an appropriate expression for the time dependence of the cross-sectional area is necessary to estimate the time dependence of the circumference. However, for the other two sets, the change in cross-sectional area is not very high and we can use an average value for the area to integrate equation 2.6 as,

$$\Delta C_f \approx -\frac{\eta A_{c,av}}{\tau\sigma} \quad (2.7)$$

or rearranging,

$$\frac{C_f}{A_{c,av}} \approx \frac{\eta}{\tau\sigma} \quad (2.8)$$

since the initial circumference C_0 is the same.

According to equation 2.8, for a given dope with a certain viscosity and surface tension, the change in the circumference varies with the inverse of the residence time in the airgap. The change is fastest in the beginning, where the driving force is the highest

and slows down as time passes and the fibers curvature is rounded.

The residence time of the fiber in the air gap, τ , is a function of the length of the air gap, the take-up speed and the speed with which the polymer dope exits the spinneret. The velocity distribution of fibers in the spinning line has usually been observed to have a sigmoid shape, which starts with the velocity at the exit of the spinneret and reaches the take-up velocity at or before the take-up element [26, 27]. Most of the available experimental data for velocity distributions is either obtained for dry melt-spinning [28] or wet-spinning [29]. Here, for simplicity, the residence time in the air gap is estimated to scale as,

$$\tau \sim \frac{2l_{airgap}}{(u_{take-up} + u_{exit})} \quad (2.9)$$

$C_f/A_{c,av}$ versus $\eta/\tau\sigma$ is plotted in (Figure 2.5). The two separate data sets are for fibers S1-S4, where the airgap was varied and for fibers S1, S5, S6 and S7, where different polymer dopes were used. As the scaling relation predicts, the fiber circumference per cross-sectional area is higher in fibers with high $\eta/\tau\sigma$, that is, high viscosity and small residence time in the air gap. From S1 to S4, increasing the residence time ten-fold decreases the fiber circumference by a factor of two. The viscosity of the dope of S1 is about six times higher than those of S6 and S7, and the circumference of S1 is about

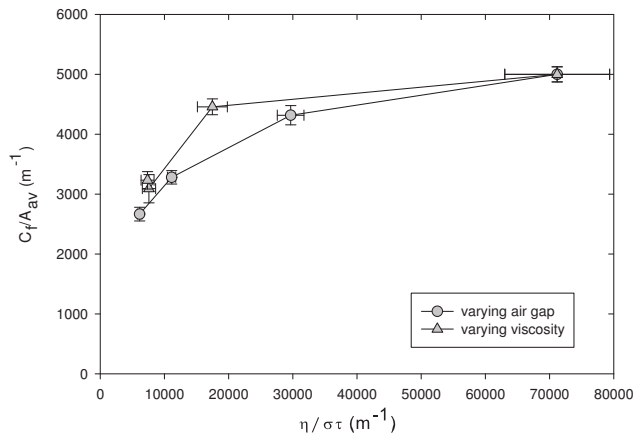


Figure 2.5: The scaling of $C_f/A_{c,av}$ with $\eta/\tau\sigma$

50% higher than the circumferences of S6 and S7.

2.3.1.5 Effect of spinning parameters on formation of macrovoids

The use of PVP and addition of nonsolvent to the polymer dope are two of the common approaches to suppress macrovoid formation, which were also used in our study [30–32]. As a result, the structured fibers contain either relatively few macrovoids or no macrovoids at all. Furthermore, the appearance of macrovoids in certain conditions agrees well with previous reports in literature. In cases where macrovoids appear such as those shown in Figures 2.3(a), 2.3(b), 2.4(b) and 2.4(c), they only appear in the thick parts of the fibers. Such dependence of macrovoid formation to membrane thickness has been reported by a number of authors [33, 34]. From polymer dope D1 to D3, an increase in macrovoid amount is observed, which can be attributed to the decreased polymer concentration and/or decreased viscosity of the polymer dope [2, 31]. By adding more water to dope D3, the macrovoids were suppressed (Figure 2.4(d)) [2].

2.3.2 Fiber performance

The primary reason for fabricating structured fibers is to enhance the flow per unit volume in a membrane module. To prove whether the enhancement in surface area of the structured fibers results in enhanced flow, the pure water permeabilities of the structured fibers (normalized for the total surface area) and their round pairs were measured. These are plotted on the left axis of Figure 2.6 for the structured fibers S1-S3 and their round counterparts R1-R3; and on the left axis of Figure 2.7 for the structured fibers S8-S11 and their round counterparts R8-R11. Together with the permeability, the separation behavior of the fibers should also be determined, since the aim is to improve the flow without altering the separation properties. This was done by measuring the molecular weight cut-off, which is plotted on the right axes of Figures 2.6 and 2.7.

Changing the air gap from 5 mm to 32 mm does not show a significant influence on the molecular weight cut-off and the pure water permeability of the fibers. This is probably because the range of air gaps used was narrow in order to maintain the

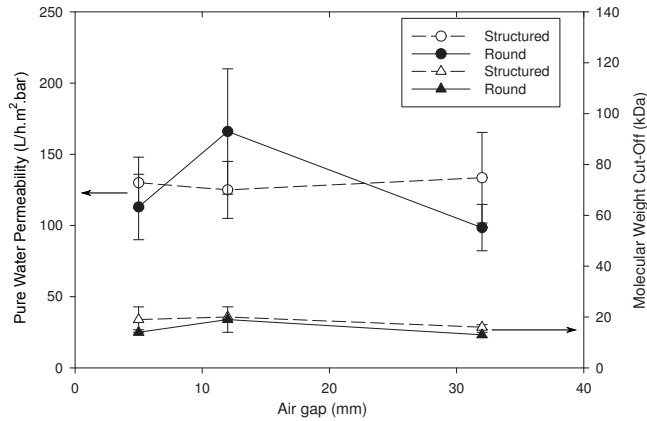


Figure 2.6: Pure water permeability and molecular weight cut-off of structured and round fibers spun with polymer dope D1 using different air gaps.

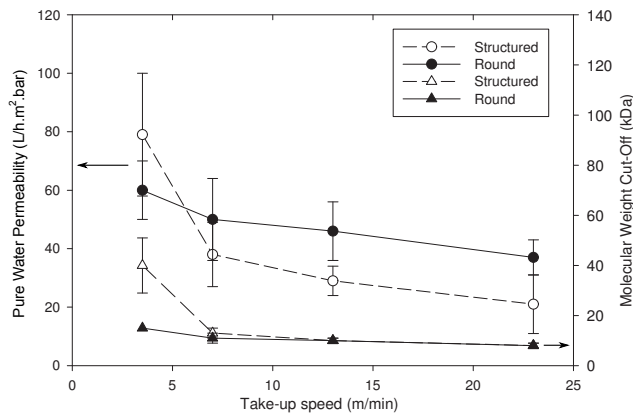


Figure 2.7: Pure water permeability and molecular weight cut-off of structured and round fibers spun with polymer dope D1 using different take-up speeds.

microstructure of the fibers. All the structured and round fibers spun with dope D1 with different air gaps have molecular weight cut-offs around 15-20 kDa and pure water permeabilities between 100 and 165 L/h.m².bar. The pure water permeabilities measured from the same batch of fibers show variances between 15 and 40% around the mean value. Such variances are not uncommon for pure water permeabilities [35, 36] and may result from slight variances in measurement or spinning conditions [18]. However, within the variance between the modules of the same fiber batch,

the permeabilities of the structured and round fiber pairs are similar. Since these permeabilities are calculated using the actual convoluted surface area of the structured fibers, this shows that the structured fibers will have enhanced flow compared to the round fibers, the enhancement being proportional to the surface area enhancement reported in Table 2.3.

A similar result is obtained when comparing structured and round fiber pairs spun by varying the take-up speed (Figure 2.7). The pure water permeabilities and molecular weight cut-offs of the structured and round pairs are similar for all the fibers except S8 and R8, which were spun using 3.5 m/min take-up speed, corresponding to a draw ratio close to 1. For the rest of the fibers, increasing the take-up speed decreased the pure water permeability and also slightly the molecular weight cut-off of the fibers. In literature, for different polymer-solvent-nonsolvent systems, the take-up speed or more generally the draw ratio has been reported to influence the pore size and the permeability in different directions [37–39]. Chang et al. argued that elongational stresses during fiber spinning may have effects in different directions for different systems. The stress may elongate the nodules on the surface, inducing molecular orientation, thus resulting in better packing of the nodules and produce membranes with small pore size and low flux, or disaggregate them resulting in increased pore size and porosity on the surface [39, 40].

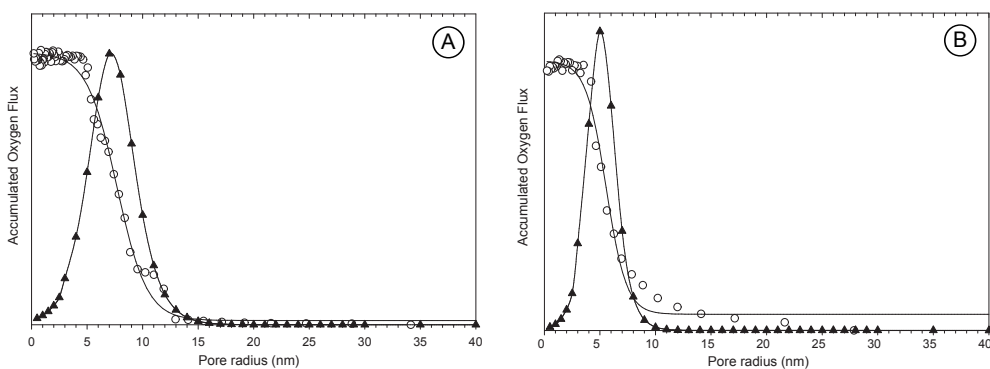


Figure 2.8: The pore size distributions (triangles) of S1 (a) and R1 (b) calculated from the accumulated oxygen flux from the feed side to the permeate side (circles) as a function of cyclohexane relative pressure

Permporometry was used as an additional method of comparing the pore size distribution of the membranes. Figure 2.8 shows the results of permporometry measurements

of S1 and R1. The calculated mean pore radii of the two fibers are 7 and 5 nm, respectively. The surface images of these fibers are given in Figure 2.9. The pore sizes seen in these images are consistent with those measured by permeometry. The pore size on the fins and in the grooves of the structured fiber S1 and the pore size on the round fiber R1 appear to be similar according to these figures.

Table 2.4 summarizes the pore size distributions of S1, R1 and the rest of the fibers. The full width at half maximum (FWHM) of the pore size distribution is also given as an indication of the broadness of the pore size distribution. With respect to both of these parameters, the pore size distributions of the structured and round fiber pairs are similar. For fibers S1, S2, R1 and R2, the mean pore diameters as well as the molecular weight cut-offs are higher than those of S9-S11 and R9-R11.



Figure 2.9: The outer surfaces of S1 in the grooves (a) and the fins (b) and the outer surface of R1 (c)

Table 2.4: Mean pore diameter and the full width at half maximum (FWHM) of the pore size distribution of the structured and round fiber pairs

Fiber	Mean pore diameter (nm)	FWHM (nm)	MWCO (kDa)
S1	14	10	19±5
R1	10	6	14±1
S2	16	12	20±1
R2	16	8	19±5
S9	4	3	13±2
S9	6	4	11±2
S10	4	2	10±1
R10	3	2	10±1
S11	6	4	8±1
R11	4	2	8±1

To have more insight on the structure of the skin layer, gold colloids were filtered from inside out through the membranes and these membranes were examined in SEM to see

where the gold particles accumulate. The fibers S1 and R1 did not show any retention to the 10 nm colloids, whereas the retentions of 20 nm colloids were 95% for S1 and 80% for R1. The fibers S9 and R9, on the other hand, showed 95% retention for the 10 nm colloids. These retentions are in good agreement with the pore size determined by FESEM and permoporometry.

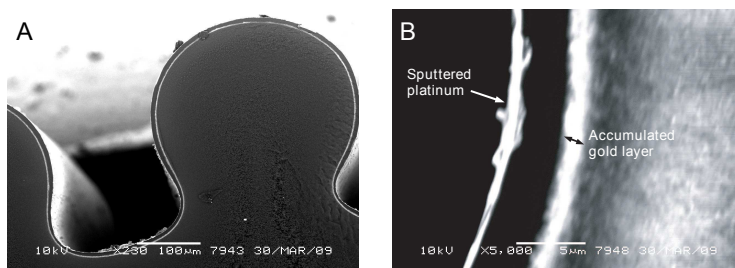


Figure 2.10: (a) The backscattered electron image of the structured fiber S1. The accumulated gold layer and the sputtered platinum layer which sandwich the skin layer are shown in (b), where a close-up of the bottom corner of the fin is illustrated.

Figure 2.10(a) shows the skin layer of S1 in one full fin and groove. The skin has a homogeneous thickness of 6 μm all along the surface except for the bottom corners of the fins, where the thickness is 3.5 μm (Figure 2.10(b)). The skin layer thickness of the round fiber R1 was found to be 4 μm . Here, we must note that the thickness measured with a certain colloid size simply indicates where a certain pore size is, rather than an absolute skin layer thickness, since the skin layer of the fibers does not have an absolute pore size but a pore size gradient as seen in Figure 2.11. So, the skin layer thickness measured with a colloid is a function of both the pore size gradient and the absolute pore size on the surface. Therefore, the thinner skin of fiber R1 can be attributed to the slightly lower retention for the 20 nm sized particles indicating larger pores on the surface, as well as a steeper pore size gradient, also seen in Figure 2.11(c).

Applying the same method to the structured fiber S9, which has a more “wavy” shape reveals a more continuous variation in the skin thickness. The skin is the thinnest in the bottom of the groove (1 μm) and the thickness increases gradually to 1.5 μm in the middle of the wall of the fin and finally to 3.5 μm at the top of the fin. The skin layer thickness of the round fiber R9 is 1.5 μm , which is comparable to the thickness

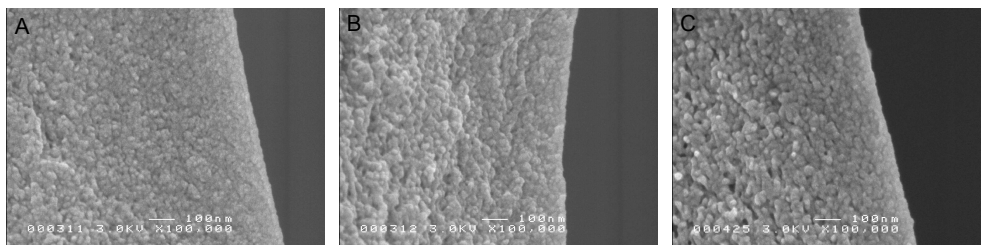


Figure 2.11: The cross section of S1 in the grooves (a) and the fins (b) and the cross section of R1 (c).

in the bottom and walls of the grooves in the structured pair, S9.

A possible explanation for the variation in the skin layer thickness of the structured fibers can be based on the local coagulation conditions at different locations in the structured fiber skin. In the corners of the grooves in S1, due to the relatively large curvature, the solvent diffusing out from all sides can create a coagulant with higher solvent concentration than for the rest of the fiber. A higher solvent concentration, in turn, creates bigger pores on the surface, which is reflected in the thinner skin layer in these parts. Since the pore size distribution is shifted towards bigger pores, the 20 nm gold particles can penetrate further towards the surface. For S9, the same curvature is present in the whole groove bottom. This can explain why we see a continuous variation in skin thickness in this fiber, as opposed to S1.

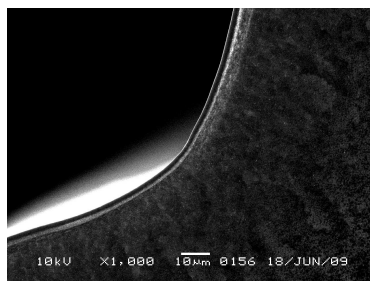


Figure 2.12: The skin layer in the corner of the fin of fiber S12 spun with a polymer dope of 95% coagulation value.

The fiber S12 with a similar flower shape as S1, spun with a polymer dope of 95% coagulation value (as opposed to the low coagulation value of dope D1 used in fibers S1 and S9) does not show the skin layer thinning in the corners (Figure 2.12). A high coagulation value provides that the polymer solution coagulates rapidly upon contact

with the coagulant. This rapid coagulation may suppress the effects of varying local coagulation conditions, resulting in a structured fiber with a homogeneous skin layer all along the surface.

2.4 Conclusions

Using a microstructured spinneret, structured and round hollow fibers for ultrafiltration were prepared. Decreasing the air gap, increasing the take-up speed and increasing the viscosity of the polymer dope were found to increase the amount of surface area enhancement obtained. A maximum surface area enhancement of 89% was obtained using a polymer dope of high viscosity and a short air gap of 5 mm. The surface area enhancement obtained by varying these parameters was compared to a simple scaling argument that relates the change in surface energy of the structured fiber in the air gap to the viscous dissipation that counters the flow of the structured surface shape towards round.

The pure water permeability, molecular weight cut-off and pore size distribution of the structured and round fiber pairs spun under the same conditions were found to be similar. This implies that the structured fibers will have enhanced flow rates due to the enhanced surface area, while maintaining the same separation behavior as the round fibers. On average, the skin layer thicknesses found by the gold colloid filtration method were found to be comparable between structured and round fibers. However, the skin layer of the structured fibers can show some variation in thickness along the surface. The structured fiber with the flower-shape had a thinner skin layer in only the corners of the fins, whereas the star-shaped fiber had a continuous gradient where the skin is the thinnest at the bottom of the fins and gets thicker towards the top of the fins. The reason for this variation is explained by the coagulant being locally higher in solvent concentration in some parts of the fiber due to the confinement caused by the curved geometry. Later, it was shown that a more rapidly coagulating system can suppress this variation in skin thickness, resulting in a structured fiber with a homogeneous skin layer all along the surface.

2.5 References

- [1] P. van de Witte, P.J. Dijkstra, J.W.A. van den Berg and J. Feijen; *Phase separation processes in polymer solutions in relation to membrane formation*; Journal of Membrane Science **117** (1-2) (1996) 1–31
- [2] Y. Liu, G.H. Koops and H. Strathmann; *Characterization of morphology controlled polyethersulfone hollow fiber membranes by the addition of polyethylene glycol to the dope and bore liquid solution*; Journal of Membrane Science **223** (1-2) (2003) 187–199
- [3] T.-S. Chung, J.-J. Qin and J. Gu; *Effect of shear rate within the spinneret on morphology, separation performance and mechanical properties of ultrafiltration polyethersulfone hollow fiber membranes*; Chemical Engineering Science **55** (6) (2000) 1077–1091
- [4] M. Khayet; *The effects of air gap length on the internal and external morphology of hollow fiber membranes*; Chemical Engineering Science **58** (14) (2003) 3091–3104
- [5] D.-G. Yu, W.-L. Chou and M.-C. Yang; *Effect of draw ratio and coagulant composition on polyacrylonitrile hollow fiber membranes*; Separation and Purification Technology **52** (2) (2006) 380–387
- [6] A. van den Berg and M. Wessling; *Nanofluidics: Silicon for the perfect membrane*; Nature **445** (7129) (2007) 726–
- [7] K. Scott, A.J. Mahmood, R.J. Jachuck and B. Hu; *Intensified membrane filtration with corrugated membranes*; Journal of Membrane Science **173** (1) (2000) 1–16
- [8] N. Tzanetakis, K. Scott, W.M. Taama and R.J.J. Jachuck; *Mass transfer characteristics of corrugated surfaces*; Applied Thermal Engineering **24** (13) (2004) 1865–1875
- [9] M.J. van der Waal and I.G. Racz; *Mass transfer in corrugated-plate membrane modules. I. Hyperfiltration experiments*; Journal of Membrane Science **40** (2) (1989) 243–260
- [10] M.J. van der Waal, S. Stevanovic and I.G. Racz; *Mass transfer in corrugated-plate membrane modules. II. Ultrafiltration experiments*; Journal of Membrane Science **40** (2) (1989) 261–275
- [11] J. Balster, M.H. Yildirim, D.F. Stamatialis, R. Ibanez, R.G.H. Lammertink, V. Jordan and M. Wessling; *Morphology and microtopology of cation-exchange*

- polymers and the origin of the overlimiting current*; Journal of Physical Chemistry B **111** (9) (2007) 2152–2165
- [12] A.M. Gronda, S. Buechel and E.L. Cussler; *Mass transfer in corrugated membranes*; Journal of Membrane Science **165** (2) (2000) 177–187
- [13] A.M. Peters, R.G.H. Lammertink and M. Wessling; *Comparing flat and micro-patterned surfaces: Gas permeation and tensile stress measurements*; Journal of Membrane Science **320** (1-2) (2008) 173–178
- [14] L. Broussous, J.C. Ruiz, A. Larbot and L. Cot; *Stamped ceramic porous tubes for tangential filtration*; Separation and Purification Technology **14** (1-3) (1998) 53–57
- [15] L. Broussous, P. Schmitz, H. Boisson, E. Prouzet and A. Larbot; *Hydrodynamic aspects of filtration antifouling by helically corrugated membranes*; Chemical Engineering Science **55** (21) (2000) 5049–5057
- [16] W. Nijdam, J. de Jong, C.J.M. van Rijn, T. Visser, L. Versteeg, G. Kapantaidakis, G.H. Koops and M. Wessling; *High performance micro-engineered hollow fiber membranes by smart spinneret design*; Journal of Membrane Science **256** (1-2) (2005) 209–215
- [17] S. Platt, M. Mauramo, S. Butylina and M. Nyström; *Retention of pegs in cross-flow ultrafiltration through membranes*; Desalination **149** (1-3) (2002) 417–422
- [18] L.J. Zeman and A.L. Zydney; *Microfiltration and Ultrafiltration - Principles and Applications* (1996); Marcel Dekker
- [19] F.P. Cuperus, D. Bargeman and C.A. Smolders; *Permporometry. The determination of the size distribution of active pores in UF membranes*; Journal of Membrane Science **71** (1-2) (1992) 57–67
- [20] A. Mey-Marom and M.G. Katz; *Measurement of active pore size distribution of microporous membranes - a new approach*; Journal of Membrane Science **27** (2) (1986) 119–130
- [21] F.P. Cuperus, D. Bargeman and C.A. Smolders; *A new method to determine the skin thickness of asymmetric UF-membranes using colloidal gold particles*; Journal of Colloid And Interface Science **135** (2) (1990) 486–495
- [22] P.S.T. Machado, A.C. Habert and C.P. Borges; *Membrane formation mechanism based on precipitation kinetics and membrane morphology: Flat and hollow fiber polysulfone membranes*; Journal of Membrane Science **155** (2) (1999) 171–183
- [23] A. Stropnik, V. Musil and M. Brumen; *Polymeric membrane formation by*

- wet-phase separation; Turbidity and shrinkage phenomena as evidence for the elementary processes*; Polymer **41** (26) (2000) 9227–9237
- [24] W. Takarada, H. Ito, T. Kikutani and N. Okui; *Studies on high-speed melt spinning of noncircular cross-section fibers. III. Modeling of melt spinning process incorporating change in cross-sectional shape*; Journal of Applied Polymer Science **80** (9) (2001) 1589–1600
- [25] H. Zheng, W. Yu, C. Zhou and H. Zhang; *Numerical simulation of the melt spinning process of noncircular fibers incorporating surface tension*; Journal of Macromolecular Science, Part B: Physics **45 B** (6) (2006) 1099–1108
- [26] W. Takarada, H. Ito, T. Kikutani and N. Okui; *Studies on high-speed melt spinning of noncircular cross-section fibers. II. On-line measurement of the spin line, including change in cross-sectional shape*; Journal of Applied Polymer Science **80** (9) (2001) 1582–1588
- [27] A. Ziabicki; *Fundamentals of Fibre Formation* (1976); John Wiley&Sons
- [28] Z. Gou and A.J. McHugh; *Two-dimensional modeling of dry spinning of polymer fibers*; Journal of Non-Newtonian Fluid Mechanics **118** (2-3) (2004) 121–136
- [29] T. Oh; *Studies on melt spinning process of hollow polyethylene terephthalate fibers*; Polymer Engineering and Science **46** (5) (2006) 609–616
- [30] R.M. Boom, I.M. Wienk, T. van den Boomgaard and C.A. Smolders; *Microstructures in phase inversion membranes. Part 2. The role of a polymeric additive*; Journal of Membrane Science **73** (2-3) (1992) 277–292
- [31] N. Peng, T.-S. Chung and K.Y. Wang; *Macrovoid evolution and critical factors to form macrovoid-free hollow fiber membranes*; Journal of Membrane Science **318** (1-2) (2008) 363–372
- [32] C.A. Smolders, A.J. Reuvers, R.M. Boom and I.M. Wienk; *Microstructures in phase-inversion membranes. Part 1. Formation of macrovoids*; Journal of Membrane Science **73** (2-3) (1992) 259–275
- [33] N. Vogrin, C. Stropnik, V. Musil and M. Brumen; *The wet phase separation: The effect of cast solution thickness on the appearance of macrovoids in the membrane forming ternary cellulose acetate/acetone/water system*; Journal of Membrane Science **207** (1) (2002) 139–141
- [34] N. Widjojo and T.-S. Chung; *Thickness and air gap dependence of macrovoid evolution in phase-inversion asymmetric hollow fiber membranes*; Industrial and Engineering Chemistry Research **45** (22) (2006) 7618–7626

- [35] J.-J. Qin, F.-S. Wong, Y. Li and Y.-T. Liu; *A high flux ultrafiltration membrane spun from PSU/PVP (K90)/DMF/1,2-propanediol*; Journal of Membrane Science **211** (1) (2003) 139–147
- [36] B. Torrestiana-Sanchez, R.I. Ortiz-Basurto and E. Brito-De La Fuente; *Effect of nonsolvents on properties of spinning solutions and polyethersulfone hollow fiber ultrafiltration membranes*; Journal of Membrane Science **152** (1) (1999) 19–28
- [37] W.-L. Chou and M.-C. Yang; *Effect of take-up speed on physical properties and permeation performance of cellulose acetate hollow fibers*; Journal of Membrane Science **250** (1-2) (2005) 259–267
- [38] J. Ren, Z. Li, F.-S. Wong and D. Li; *Development of asymmetric BTDA-TDI/MDI (P84) co-polyimide hollow fiber membranes for ultrafiltration: The influence of shear rate and approaching ratio on membrane morphology and performance*; Journal of Membrane Science **248** (1-2) (2005) 177–188
- [39] K.Y. Wang and T.-S. Chung; *Polybenzimidazole nanofiltration hollow fiber for cephalixin separation*; AIChE Journal **52** (4) (2006) 1363–1377
- [40] T.-S. Chung; *The limitations of using Flory-Huggins equation for the states of solutions during asymmetric hollow-fiber formation*; Journal of Membrane Science **126** (1) (1997) 19–34

CHAPTER 3

Fouling behavior of microstructured hollow fiber membranes in dead-end filtrations: Critical flux determination and NMR imaging of particle deposition

THIS CHAPTER HAS BEEN SUBMITTED FOR PUBLICATION:

P.Z. Çulfaz, S. Buetehorn, L. Utiu, M. Kueppers, B. Bluemich, T. Melin, M. Wessling and R.G.H. Lammertink, *Fouling behavior of microstructured hollow fiber membranes in dead-end filtrations: Critical flux determination and NMR imaging of particle deposition*, Langmuir

ABSTRACT

The fouling behavior of microstructured hollow fibers was investigated in constant flux filtrations of colloidal silica and sodium alginate. It was observed that the fouling resistance increases faster with structured fibers than with round fibers. On the other hand, reversibility of structured fibers' fouling was similar during silica filtrations and better in sodium alginate filtrations when compared to round fibers. The deposition of two different silica sols on the membranes was observed by NMR imaging. The sols had different particle size and solution ionic strength and showed different deposition behaviors. For the smaller particle sized sol in deionized solution (Ludox-TMA), there was more deposition within the grooves of the structured fibers and much less on the fins. For the alkali-stabilized sol Bindzil 9950, which had larger particles, the deposition was homogeneous across the surface of the structured fiber and the thickness of the deposit was similar to that on the round fiber. This difference between the deposition behavior of the two sols is explained by differences in the back diffusion, which creates concentration polarization layers with different resistances. The Ludox sol formed a thick polarization layer with very low resistance. The Bindzil sol formed a slightly thinner polarization layer, however its resistance was much higher, of similar magnitude as the intrinsic membrane resistance. This high resistance of the polarization layer during the Bindzil sol filtration is considered to lead to quick flow regulation towards equalizing the resistance along the fiber surface. On the other hand, the Ludox particles were trapped at the bottom of the grooves as a result of reduced back diffusion. The fouling behavior in sodium alginate filtrations was explained by considering the size-dependent deposition within the broad alginate size distribution. The better reversibility of fouling in the structured fibers is thought to be the result of a looser deposit within the grooves which is more easily removed than a compressed deposit on the round fibers.

3.1 Introduction

Concentration polarization and succeeding particle deposition on the membrane surface are the main factors limiting the productivity of membranes [1–3]. Concentration polarization is inherent to all membrane separations, as it is a result of the accumulation of retained material near the membrane surface. For colloids (1–1000 nm), when the particle concentration near the membrane exceeds a certain value, the particles coagulate to form a cake or gel layer [4, 5]. This phase transition from the dispersed phase to the condensed phase is due to the surface interactions between the particles and depends strongly on solution properties such as pH and ionic strength, as well as the size and surface charge of the colloidal particles [6].

Membrane filtrations can be operated in dead-end or cross-flow modes. The choice depends on the optimization of the productivity versus the operational costs. For heavily fouling feeds cross flow is often necessary, while for feeds with lower fouling potential dead end operation is usually more economical. In a dead-end filtration, the retained particles continuously accumulate on the membrane surface as filtration proceeds. To prevent excessive performance decline, periodic backwashes are required to remove deposited particles from the membrane surface. For sustainable operation, the backwashing should be able to remove all the deposited particles, in which case the deposition on the membrane is classified as reversible fouling. Any irreversible fouling will deteriorate the membrane's performance in time, and is therefore undesired. In a dead-end filtration, the flux below which all fouling is reversible is defined as the critical flux [7, 8]. The critical flux for a certain membrane depends on the feed solution and the filtrate load between two backwashes.

To study fouling, the first approach is to monitor the transmembrane pressure increase at constant flux or flux decline at constant pressure and to determine the reversibility of the fouling. Complementary to these indirect methods of fouling detection, in recent years there have been efforts to observe particle deposition on membranes *in situ* [9]. One of these methods is NMR imaging, which is able to identify local concentration variations. The method has been used to visualize the formation of polarization layers during the filtration of oil-water emulsions, bentonite and colloidal silica particles [10, 11]. In bentonite and silica suspensions, the particles do not contribute to the NMR signal, but they alter the relaxation times (T_1 and T_2) of surrounding water protons.

By relating the particle concentration to T_1 and T_2 , information on concentration polarization and particle deposition can be obtained.

In this study, we characterize the fouling behavior of microstructured hollow fiber membranes in dead-end filtrations by using both critical flux determination methods and online NMR imaging of particle deposition. In the previous chapter, these microstructured membranes were shown to increase the productivity by increasing the membrane area per fiber length compared to round fibers [12]. The characterization of the fouling behavior of these membranes in dead-end systems provides insight into the productivity of these membranes in actual filtrations, as well as a starting point for understanding filtrations in cross-flow and submerged, aerated systems.

3.2 Experimental

3.2.1 Membranes

One microstructured and one round hollow fiber membrane made by the dry-wet phase inversion of the polymer dope 16.6% PES, 4.91% PVP K30, 4.91% PVP K90, 7.18% H_2O , 66.32% NMP, with water as the external coagulant were used throughout this study (Figure 3.1). Details of the fabrication are described in Chapter 2 [12]. The structured fiber has 60% higher surface area per length compared to the round fiber. The pure water permeability of the fibers are 235 ± 11 L/h.m².bar and 233 ± 12 L/h.m².bar for structured and round fibers, respectively. The mean pore diameter of both fibers was found to be 12 nm by permoporometry measurements (Figure 3.2).

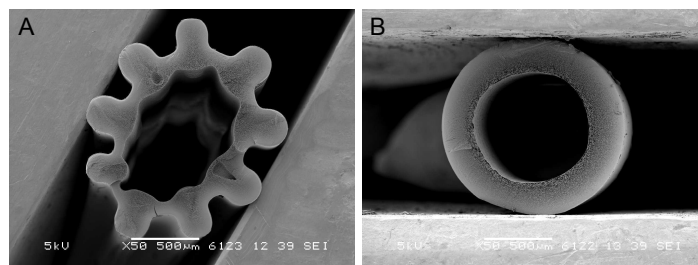


Figure 3.1: (a)Microstructured and (b)round hollow fibers used in this study

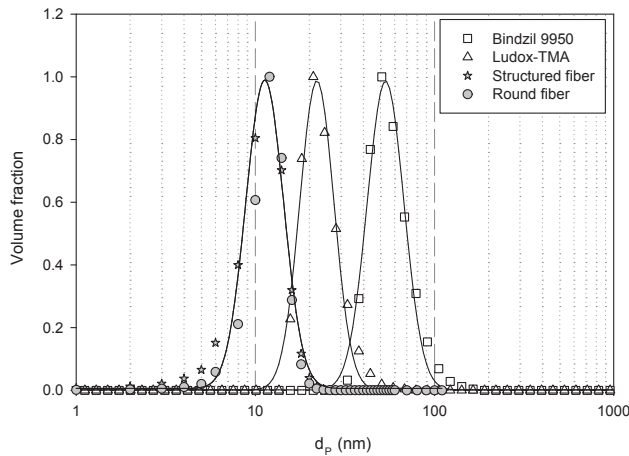


Figure 3.2: Particle size distributions of the silica sols and the pore size distributions of the membranes

3.2.2 Materials

Ludox-TMA colloidal silica was purchased from Sigma-Aldrich. The stock solution has 34 wt% silica in deionized water, with pH of 6-7. Bindzil-9950 colloidal silica was kindly provided by Eka Akzo Nobel. The stock solution contains 50 wt% silica, and is alkali-stabilized at a pH of 9. The particle size distribution and zeta potential of the sols were measured with a Malvern Zetasizer Nano-ZS instrument. The particle size distributions of the sols are shown in Figure 3.2 together with the pore size distribution of the membranes measured by permporometry. Although there is a small overlap between the particle size distribution of Ludox-TMA and the pore size distribution of the membranes, no silica was observed in the permeates.

Sodium alginate (A2158, low viscosity, ~ 250 cp at 2%) was purchased from Sigma-Aldrich. All feed solutions were prepared with ultrapure water ($18 \text{ m}\Omega\cdot\text{cm}$). The retention of sodium alginate was determined by total carbon analysis, using $TOC - V_{CPH}$ (Shimadzu).

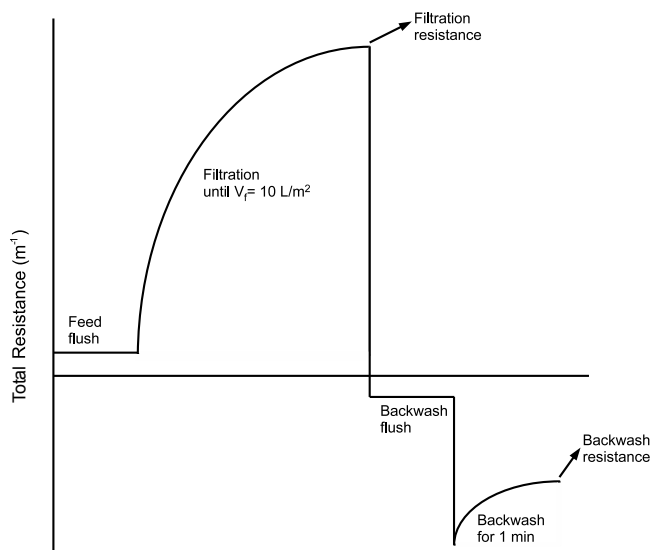


Figure 3.3: A single cycle used in flux-stepping experiments consisting of filtration and backwash

3.2.3 Flux-stepping Experiments

The experimental setup used in the flux-stepping experiments is described in [8]. Flux steps from 20 L/h.m^2 to 90 or 110 L/h.m^2 were applied, with 15 cycles at each flux consisting of a filtration period followed by a backwashing period (Figure 3.3). The filtration period was carried out until 10 L of permeate were filtered per m^2 membrane area. Backwashing was done for one minute at 200 L/h.m^2 for the silica feed and 175 L/h.m^2 for the sodium alginate feed. Fouling reversibility was assessed by comparing the filtration resistance or backwash resistance (Figure 3.3) of consequent cycles at constant flux.

3.2.4 Nuclear Magnetic Resonance (NMR) imaging

The particle deposition on the surface of the hollow fibers was non-invasively investigated by means of nuclear magnetic resonance imaging. For this purpose, the experimental setup shown in Figure 3.4 was used. The system was equipped with a single hollow fiber of 50 cm length and operated at constant permeate flux. The

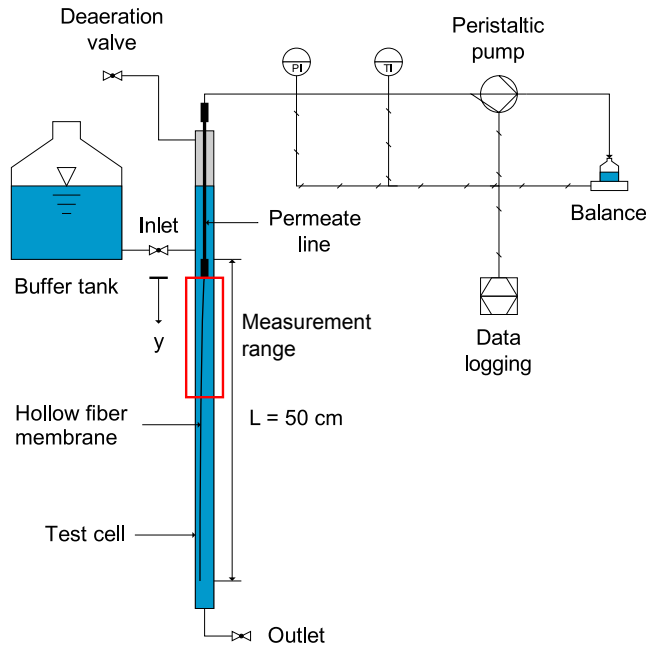


Figure 3.4: Schematic of the NMR setup [13]

pressure and the temperature were measured in the permeate line for monitoring the evolution of the fouling resistance over time. A number of consecutive NMR measurements was performed to capture the corresponding increase in cake layer thickness within 3 adjacent measurement slices. The centre-lines of these slices were located 5, 10 and 15 mm below the point of permeate extraction at the fiber top. A virgin membrane and a fresh silica suspension were used for each test run. For the silica filtration tests, a transmembrane pressure difference (TMP) of 800 mbar was chosen as an abort criterion. Details of the experimental setup and the test protocols used are explained in [13].

The NMR measurements presented in this paper are a follow-up of previous studies to visualise cake growth and removal in membrane filtration processes [13, 14]. For the observation of cake layers consisting of colloidal silica particles, a three-dimensional gradient echo pulse sequence was applied [14]. Since it is known that the silica particles do not contribute to the ^1H NMR signal [10], a proper cake-bulk contrast was facilitated. This image contrast is due to differences in the relaxation time

Table 3.1: NMR settings for cake growth visualization [14]

NMR settings	Cake growth pulse sequence
Sequence type	3D gradient echo
Data acquisition time (mm:ss)	03:25
Repetition time (TR) (ms)	100
Echo time (TE) (ms)	3
Flip angle ($^{\circ}$)	45
Number of images averaged	8
Field of view (FOV) (mm \times mm \times mm)	9 \times 9 \times 2
Matrix size before zero-filling (pix \times pix \times pix)	256 \times 256 \times 1
Matrix size after zero-filling (pix \times pix \times pix)	512 \times 512 \times 1
Spatial resolution before zero-filling (μm)	35.2 (radial direction)
Spatial resolution after zero-filling (μm)	17.6 (radial direction)

of water protons bounded to the silica particles as compared to that of free water protons. Within these images, the bulk phase is characterised by a relatively low signal intensity, whereas the signal originating from the cake is higher due to a higher solids concentration. The liquid within the membrane pores appears as a region of lower signal intensity due to the saturation of the free water signal. The membrane lumen, instead, is represented by a bright white spot, which is an image artefact caused by the permeate flow. Alterations in shape of this spot as the filtration progresses can be attributed to the passage of degassing products during data acquisition. The NMR settings are summarised in Table 3.1, whereas a more detailed description of the pulse sequence can be found elsewhere [14].

3.3 Results and Discussion

3.3.1 Flux-stepping experiments with colloidal silica

Figure 3.5 shows the membrane resistance at the end of the filtration and backwash periods (as illustrated in Figure 3.3) in the flux-stepping experiments with 0.05 wt% Ludox-TMA colloidal silica feed. Both of these resistances were essentially constant in the filtrations at all fluxes during the experiments, implying that there is no significant irreversible fouling in neither the structured nor the round fibers between fluxes of 20 to 90 L/h.m². In addition, the backwash resistances were close to the intrinsic membrane resistances of the fibers, which also implies that by the end of the backwash

all the deposit from the filtration period is removed from the membrane surface.

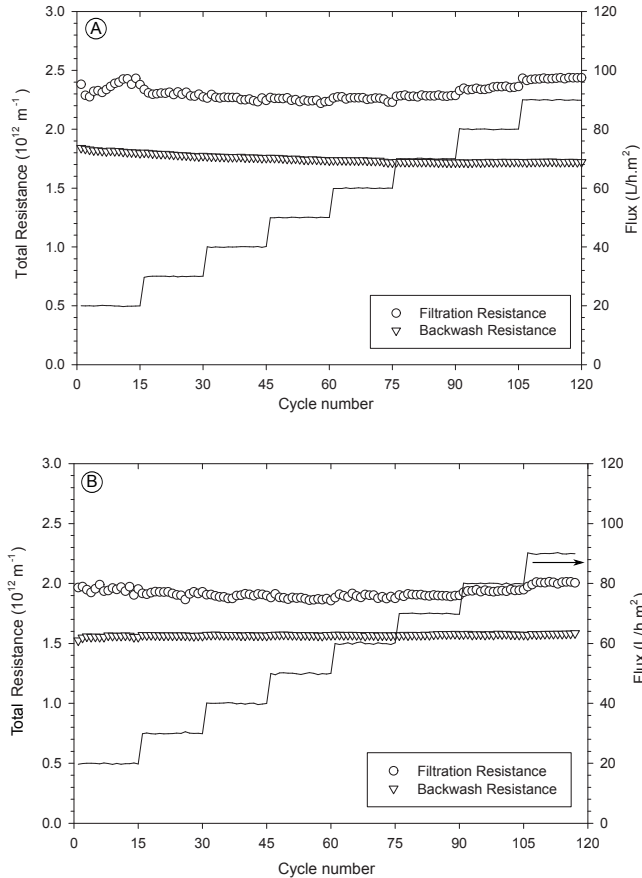


Figure 3.5: Flux-stepping experiments with 0.05 wt% Ludox-TMA colloidal silica feed. (a) Structured fibers (b) Round fibers

Figure 3.6 shows the increasing fouling resistance as a function of filtered permeate volume for the structured and round fibers, with 0.05 wt% and 0.1 wt% feeds at a flux of 70 L/h.m^2 . The resistance increase during the filtrations was steeper for the structured fibers compared to the round ones at all fluxes. The rate of resistance increase ($dR_{\text{fouling}}/dV_{\text{filtered}}$) also increased with increasing permeate flux for both of the fibers. For the structured fibers this increase was steeper (Figure 3.7).

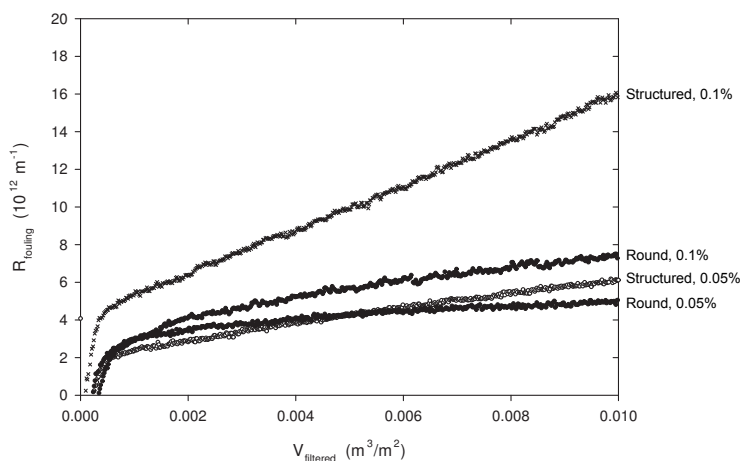


Figure 3.6: Increase of fouling resistance in a single filtration cycle at 70 L/h.m² for structured and round fibers, with 0.05 wt% and 0.1 wt% feeds

3.3.2 NMR imaging of silica deposition

NMR imaging of particle deposition was carried out with two different kinds of colloidal silica: Ludox-TMA, which was also used in flux-stepping experiments, and Bindzil 9950. As shown in Figure 3.2, the Ludox-TMA sol has smaller particles (mean particle diameter of 20 nm) and is deionized. According to the manufacturer, however, the stock solution contains 0.04 wt% of Na₂SO₄. Bindzil 9950, on the other hand, is composed of larger particles (mean particle diameter of 60 nm) and is alkali-stabilized with 0.1 wt% of Na₂O.

The particle deposition with these two silica sols was investigated under two conditions: Permeate flux of 70 L/h.m², with a 0.1 wt% feed concentration, and permeate flux of 20 L/h.m² with a 0.9 wt% feed concentration. It was observed that the deposition of the two sols followed different patterns. Figures 3.8 and 3.9 display the NMR images at different times of filtration together with the resistance increase as a function of filtrate volume. We must keep in mind that the images are recorded from the uppermost part of the fiber, whereas the resistance of the fouling layer reflects the whole fiber. In filtrations with hollow fibers, TMP, and therefore the deposit thickness often varies throughout the length of the fiber due to the pressure drop in the fiber

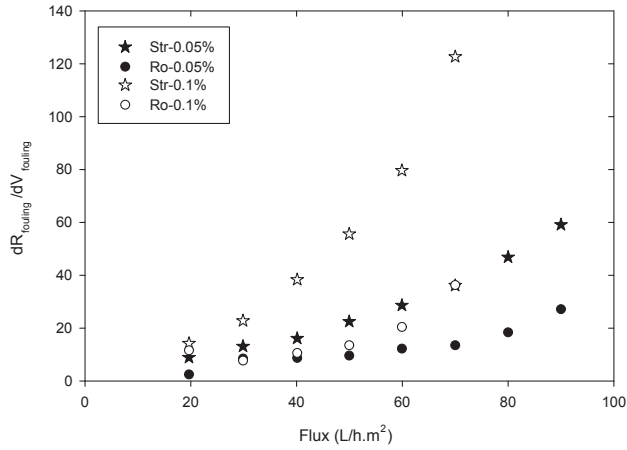


Figure 3.7: Fouling rate as a function of permeate flux, calculated as the slope of the $dR_{\text{fouling}}/dV_{\text{filtered}}$ vs dV_{filtered} plot (Figure 3.6) between $V_f=0.006-0.01 \text{ m}^3/\text{m}^2$

lumen [15].

During the filtration of the Bindzil sol, there is a homogeneous deposition of the cake throughout the surface of the structured fiber (Figures 3.8 and 3.9). The thickness of the cake is similar for both structured and round fibers at fluxes of 20 and 70 L/h.m². The thicker cake at 20 L/h.m² is due to the higher feed concentration.

On the other hand, during the filtration of the Ludox sol, within the grooves the deposit is more concentrated than on the fins and than the deposit on the round fibers. At 20 L/h.m², the deposit fills the whole groove starting from the first images, while at 70 L/h.m² it starts from the bottom of the groove and gradually fills it up. The deposition on the fins of the structured fiber and that on the round fiber appear much looser than that within the grooves. We must note that the calibrations for the particle concentration of the two sols with respect to the proton relaxation rates were different. Therefore the intensities of the cake layer in the Ludox and Bindzil filtrations cannot be compared directly.

In a dead-end filtration, the material balance for the filtered particles is:

$$\frac{\partial \phi}{\partial t} = \frac{\partial}{\partial x} \left[D(\phi) \frac{\partial \phi}{\partial x} - J\phi \right] \quad (3.1)$$

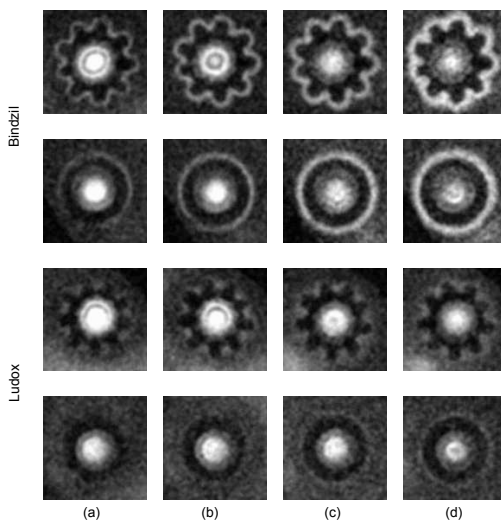
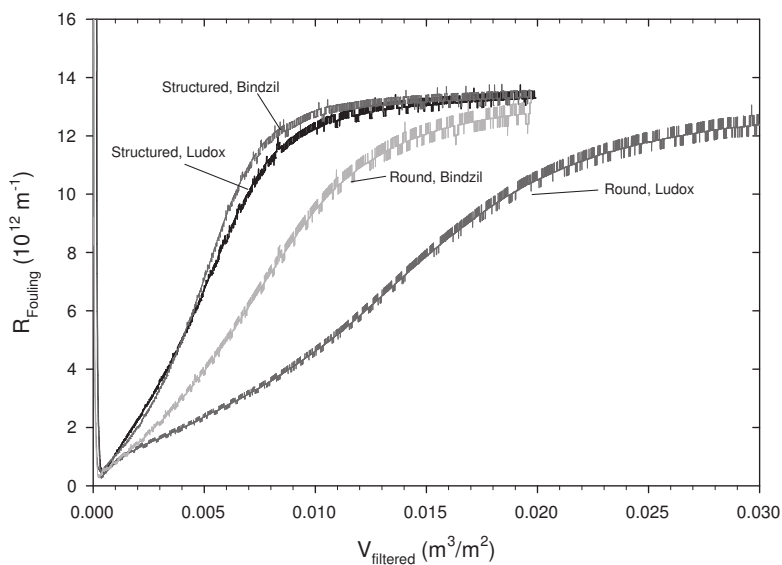


Figure 3.8: Particle deposition on structured and round fibers at 20 L/h.m² with 0.9 wt% Ludox and Bindzil sols. Images are from $V_{filtered} = 0.0035 \text{ m}^3/\text{m}^2$ (a), $0.007 \text{ m}^3/\text{m}^2$ (b), $0.0125 \text{ m}^3/\text{m}^2$ (c) and $0.018 \text{ m}^3/\text{m}^2$ (d)

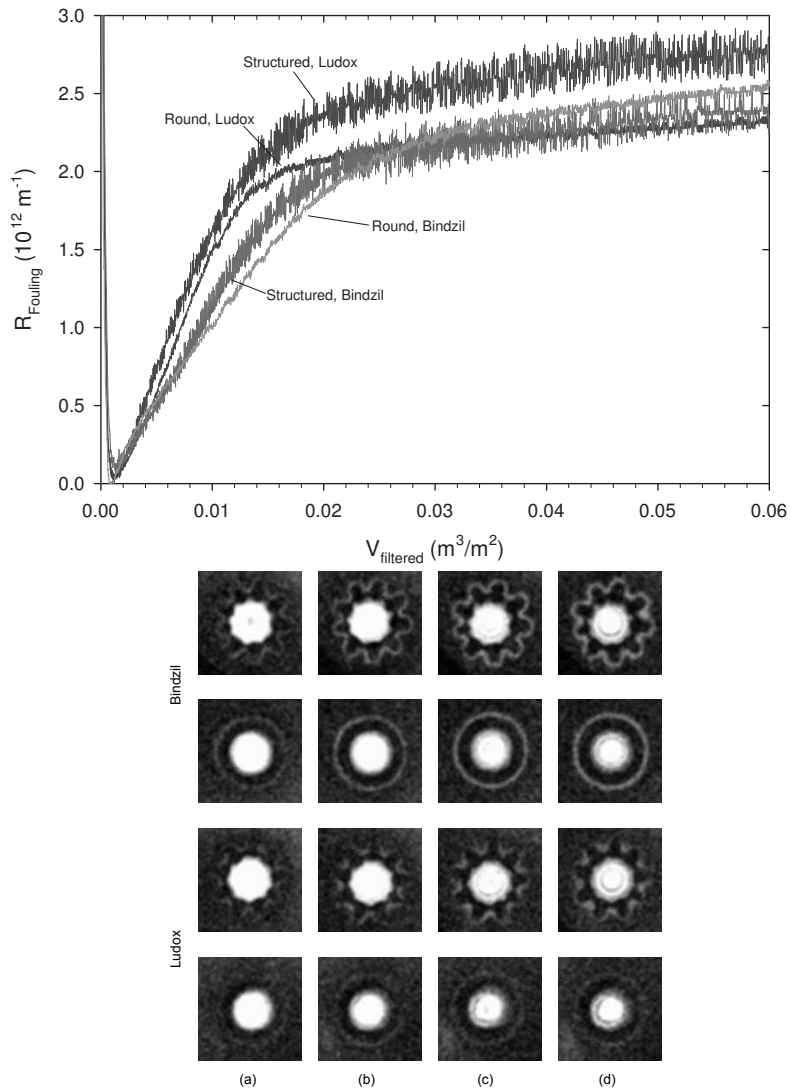


Figure 3.9: Particle deposition on structured and round fibers at 70 L/h.m^2 with $0.1 \text{ wt}\%$ Ludox and Bindzil sols. Images are from $V_{\text{filtered}} = 0.01 \text{ m}^3/\text{m}^2$ (a), $0.02 \text{ m}^3/\text{m}^2$ (b), $0.04 \text{ m}^3/\text{m}^2$ (c) and $0.06 \text{ m}^3/\text{m}^2$ (d)

where ϕ denotes the particle volume fraction, $D(\phi)$ the diffusion coefficient, J the permeate flux and x the coordinate perpendicular to the membrane surface.

The concentration-dependent diffusion coefficient, $D(\phi)$, can be estimated using the generalized Stokes-Einstein equation,

$$D(\phi) = \frac{V_p}{6\pi\mu a H(\phi)} \frac{d\Pi}{d\phi} \quad (3.2)$$

where V_p is the volume of the suspended particle, μ is the viscosity of the medium, a is the particle radius, $H(\phi)$ is the Happel function (see Appendix) and Π is the osmotic pressure. The details of the osmotic pressure calculation are given in the Appendix.

Equation (3.1) was solved for the evolution of the concentration polarization (CP) layer using MATLAB. The following boundary and initial conditions were used:

$$\text{at } x=0, \phi(0, t) = \phi_{wall}$$

$$\text{at } x=\infty, \phi(\infty, t) = \phi_{bulk}$$

$$\text{at } t=0, \phi(x, 0) = \phi_{bulk}$$

ϕ_{wall} is the maximum stable colloid concentration which corresponds to the maximum osmotic pressure, or equivalently zero diffusivity. The time for the wall concentration to reach the maximum value of ϕ_{wall} is found to be negligible with respect to the time it takes to form a steady-state polarization layer, based on the solution of Equation 3.1 using a rate of concentration increase at the wall. Also, at the time the wall concentration reaches ϕ_{wall} , the concentration away from the wall is assumed to be still the bulk concentration. After the formation of the concentration polarization layer, with continued filtration a cake layer starts to grow on the membrane wall, accompanied by a polarization layer on top of the cake.

At steady-state, the convective transport is equal to the diffusive back transport. In Table 3.2, the steady-state thickness of the polarization layers are given. For all cases, the thicknesses are on the order of the convolutions of the structured fibers and would immediately fill the grooves of these fibers from the beginning of the filtration. However, the structures of the polarization layers of the two sols are quite different (Figure 3.10). For the Bindzil sol, the polarization layer is highly concentrated throughout its whole

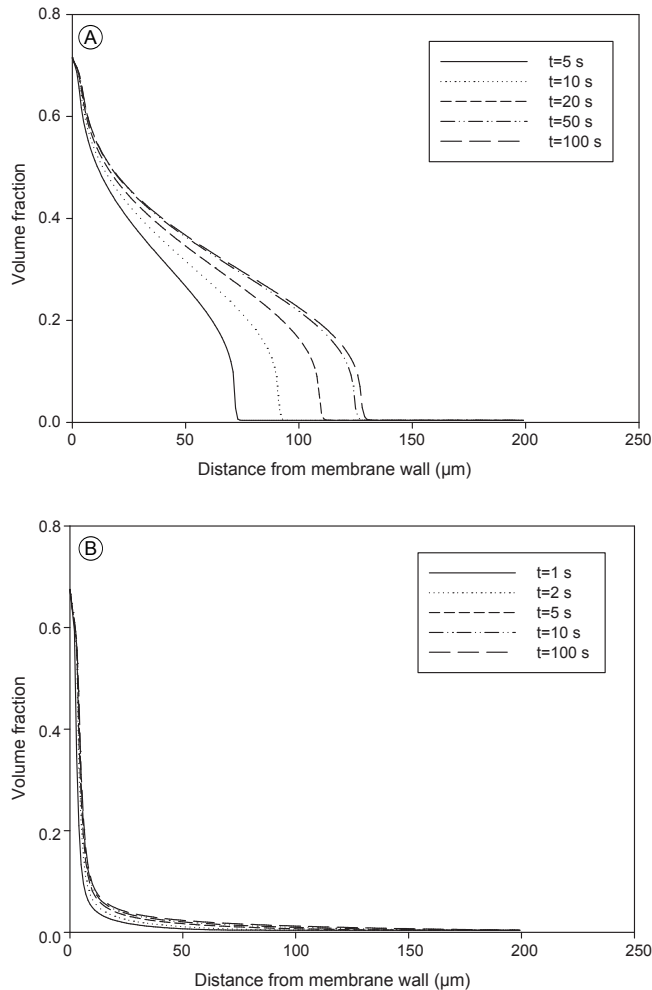


Figure 3.10: The formation of the concentration polarization layer during the filtration of 0.9 wt% Bindzil sol (a) and Ludox sol (b) at 20 L/h.m^2

thickness. For 20 L/h.m^2 , the total resistance of the polarization layer is estimated as $1.5 \times 10^{12} \text{ m}^{-1}$ using the Kozeny-Carman equation. This resistance is about the same magnitude as the intrinsic membrane resistance. On the other hand, the Ludox polarization layer, despite its high thickness, has very low concentrations in the majority of its thickness. The resistance of this dilute layer that extends throughout the groove is about two orders of magnitude smaller than the intrinsic membrane resistance. Consequently, when the filtration of the Bindzil sol starts, the polarization

Table 3.2: Steady-state concentration polarization layer thickness for the four feed solutions, found by solving Equation 3.1 with the transient term equal to zero and δ_{cp} as the distance x from the membrane where $\phi = \phi_{bulk}$

Feed	δ_{cp}
70 L/h.m ² , 0.1 wt% Ludox	65 μm
70 L/h.m ² , 0.1 wt% Bindzil	57 μm
20 L/h.m ² , 0.9 wt% Ludox	190 μm
20 L/h.m ² , 0.9 wt% Bindzil	130 μm

layer that forms immediately creates an imbalance between the total resistance in the grooves and on the fins of the fiber. When there is such an imbalance, the total flow will be regulated such that more of it permeates through the low-resistance regions, and less through the high-resistance regions. This self-regulation of the permeate flow acts towards equalizing the resistance throughout the surface, since more will deposit on the initially lower resistance regions, and vice versa. This results in a homogeneous cake thickness everywhere on the surface of the fiber.

On the other hand, for Ludox, with the polarization layer filling the grooves, the resistance is still essentially the same everywhere on the fiber due to the low resistance of this dilute polarization layer. As a result, equal amounts of permeate flow through the complete surface of the fiber. However, within the groove the concentration is higher than in the bulk, and as the groove is filled to the top, the total thickness of the CP layer for the bottom of the groove is twice that of the fins. Therefore, the concentration gradient for back diffusion is less compared to the fins. As a result, the convective flow due to permeation is more dominant over back diffusion and the deposit is more concentrated. As the inhomogeneities in cake thickness and porosity create an imbalance between the different locations, the flow will start to be self-regulated in this case as well. However, for whatever the amount that flows through the grooves, the back diffusion will be less compared to that on the fins, which keeps the initial deposit trapped within the grooves and allows further deposition on and compression of this layer.

At 20 L/h.m², the deposit in the grooves is looser than that at 70 L/h.m². At 70 L/h.m², convective flow is more dominant over back diffusion and the deposition in the grooves starts first from regions where the concentration gradient is lowest, i.e. the bottom of the grooves, since the polarization layer does not fill the groove totally.

As more cake deposits, the polarization layer starts to fill the whole groove and the deposition moves on to fill most of the groove.

In flux-stepping experiments and NMR filtrations we mostly see steeper resistance rise with structured fibers. For the Bindzil sol, where the cake thickness and porosity appear similar in both fibers, this is attributed to the fact that the effective filtration area, which is that of the membrane and the cake layer on top, changes as the cake deposits [16]. For the round fibers, as more cake deposits the area for filtration increases. On the other hand, for the structured fibers, with the grooves filled, soon the effective area becomes much less. Table 3.3 illustrates the change in membrane area, and the resulting effective flux for the round and structured fibers. Assuming constant specific cake resistance, the ratio of the fouling resistances in the structured and round fibers is estimated in the last column, and compared to the actual ratio observed. For the Bindzil sol, the estimate fits the actual values quite well. However, for the Ludox sol the fouling resistance on the structured fibers is more than twice the resistance on the round fibers, which is much more than the value estimated solely based on the changing effective membrane area. This inconsistency is because in the grooves of the structured fibers the cake is denser than that on the round fiber and the higher specific resistance of this cake further increases its resistance.

In the flux-stepping experiments shown in Figure 3.5, the fouling during the filtration of the Ludox-TMA silica sol was found to be fully reversible for both fibers, although we observe in the NMR images that there exists a more compact cake layer in the grooves of the structured fibers. This shows that although the thickness and porosity of the deposit varies throughout the surface of these fibers, the variation in the resistance of these deposits is not high, since in such a case backwashing would not be effective on the high resistance areas, as the water would preferentially flow through low resistance areas.

3.3.3 Flux-stepping experiments with sodium alginate

With a 20 ppm sodium alginate feed solution, two distinct fouling behaviors were observed for the structured and round fibers (Figure 3.11). In the structured fiber, at fluxes higher than 20 L/h.m², the resistance at the end of a filtration cycle is constant irrespective of the flux, whereas in the round fiber it increases with increasing flux.

Table 3.3: Estimated and experimentally observed ratios resistances of the structured-to-round fibers. A is the effective area for filtration after cake deposition, A_0 is the initial clean membrane area and J_{eff} is the effective flux through the altered membrane area, A .

0.9 wt% Bindzil at 20 L/h.m ²						
V_f	A/A_0		J_{eff}		$R_{\text{str}}/R_{\text{ro}}$	
	Str	Ro	Str	Ro	estimated	actual
0.0035	1.00	1.14	20.00	17.50	1.14	1.63
0.007	0.99	1.19	20.20	16.80	1.20	1.69
0.011	0.97	1.23	20.60	16.30	1.26	1.27
0.015	0.96	1.26	20.80	15.90	1.31	1.08
0.019	0.94	1.33	21.30	15.00	1.42	1.06
average:					1.27	1.35

0.9 wt% Ludox at 20 L/h.m ²						
V_f	A/A_0		J_{eff}		$R_{\text{str}}/R_{\text{ro}}$	
	Str	Ro	Str	Ro	estimated	actual
0.0035	0.85	1.00	24.40	20.00	1.22	2.41
0.007	0.85	1.07	23.50	18.70	1.26	3.19
0.011	0.87	1.10	23.00	18.20	1.26	2.44
0.015	0.87	1.17	23.00	17.10	1.35	1.67
0.019	0.85	1.14	23.50	17.50	1.34	1.35
average:					1.29	2.21

Also, in the structured fiber there is almost no irreversible fouling, whereas the round fiber starts to foul irreversibly from 70 L/h.m² on. The retention was similar for both fibers (Figure 3.12) and increased with increasing flux until 60 L/h.m², after which a maximum was reached around 90%. Although the low retention at 20 L/h.m² can partly explain the increasing resistance after this flux for both of the fibers, this cannot be the only reason for the difference between the two kinds of fibers since the retention is similar. Figure 3.13 shows the fouling resistance as a function of filtered volume for three different fluxes for the structured and round fibers. For the structured fiber, the resistance rises in a similar way at all fluxes, whereas in the round fiber the rise is slower at low fluxes and gets faster with increasing flux.

Sodium alginate is a mixture with a broad size distribution (10-100 nm) [8]. Within this broad distribution there are small molecules with high diffusivities and large molecules with low diffusivities. Due to the difference in back diffusion of these different size fractions, they will be fractionated in the deposited cake with larger molecules

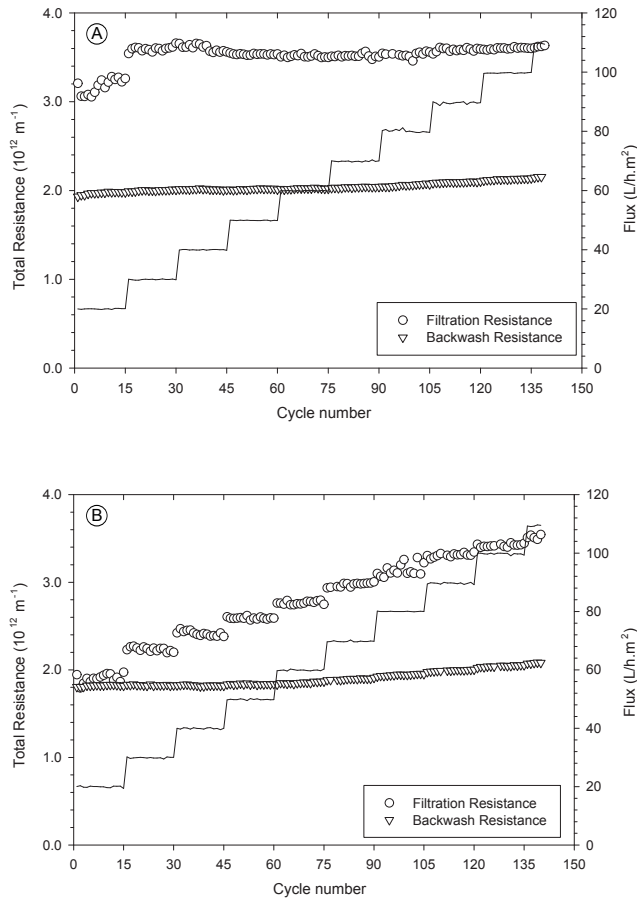


Figure 3.11: Flux-stepping experiments with 20 ppm sodium alginate. (a) Structured fibers
(b) Round fibers

closer to the membrane and smaller ones closer to the bulk [8, 17]. At low fluxes, most of the small alginates will be loosely packed at the cake-bulk interface. As flux increases, the permeate drag will start to be dominant over back diffusion also for the smaller fractions and the cake will be in a more compressed state.

For the structured fiber, based on the size range of the alginates, their negative surface charge and the low ionic strength of the medium, we can consider sodium alginate filtration as a superposition of the NMR observations with the Ludox and Bindzil silica sols. In this case, the large alginate fractions form a high resistance polarization layer

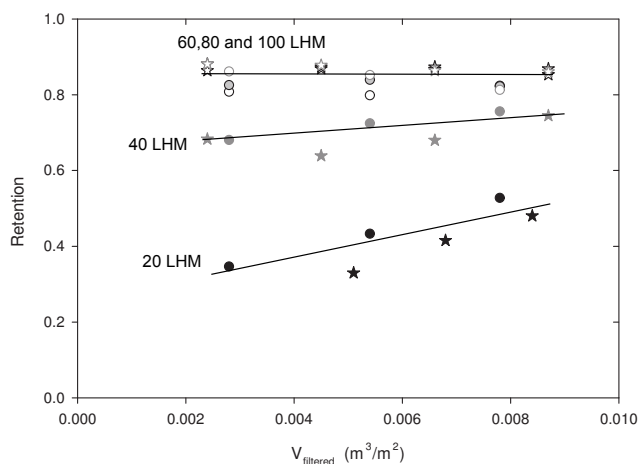


Figure 3.12: Sodium alginate retention of the fibers. Stars: Structured fibers, Circles: Round fibers

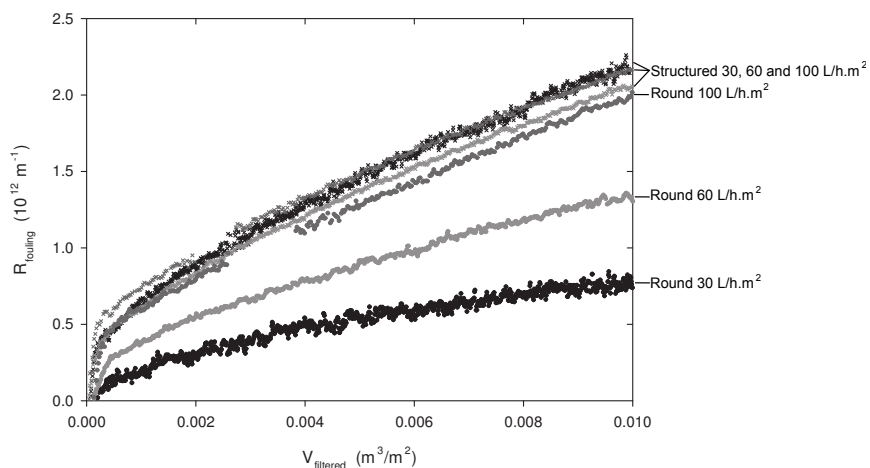


Figure 3.13: Increase of fouling resistance in separate sodium alginate filtration cycles at 30, 60 and 100 L/h.m² for the structured and round fibers

within the grooves, with small particles concentrated close to the bulk and in much lower concentrations further within the groove. The resistance of this polarization layer can be significant as in the case of the Bindzil sol, giving rise to the self-regulation

of the permeate flow, which continuously tends to equalize the resistance throughout the fiber's surface. The initial filling of the grooves is expected to be similar at all fluxes, which explains the invariant resistance increase behavior at all fluxes. The self-regulating flow can create differences in porosity of the deposit on different parts of the fiber. In the grooves, the deposit is probably looser and thicker, whereas towards the fins the porosity and thickness decrease, while the resistances are equal on both parts. The better reversibility of fouling can be attributed to the looseness of the majority of the deposit, which would make it easier to remove.

3.4 Conclusions

The fouling behavior of microstructured hollow fibers was investigated during constant flux filtrations of colloidal silica and sodium alginate. Additionally, NMR imaging was performed to study the deposition of two different silica sols. The deposition behavior was found to be different for the two sols of different particle size and solution ionic strength. For the smaller particle-sized sol in deionized solution (Ludox-TMA), the deposition within the grooves of the structured fibers was significantly higher than that on the fins. For the alkali-stabilized sol (Bindzil 9950), which had larger particles, the deposition was homogeneous throughout the surface of the structured fiber and the thickness of the deposit was similar to that on the round fiber. This difference between the deposition behavior of the two sols was explained by differences in back diffusion, which create concentration polarization layers with different resistances. Both of the silica sols form polarization layers thick enough to fill all or most of the grooves in the structured fibers. Nevertheless, the polarization layer formed by the Ludox sol has very low resistance, whereas that of the Bindzil sol has a much higher resistance. This high resistance polarization layer which fills the grooves is considered to lead to quick flow regulation during the Bindzil sol filtration, which drives the filtration towards equalizing the resistance over the fiber surface. On the other hand, the Ludox particles are trapped at the bottom of the grooves due to equally continuing filtration through the grooves and the fins, which results in a lowered concentration gradient in the grooves and leads to reduced back diffusion.

The structured fibers showed better fouling reversibility than round fibers in sodium alginate filtrations. This difference was explained by considering the size-dependent

deposition within the broad alginate size distribution. Filling of the grooves in the structured fibers with a high-resistance concentration polarization layer results in self-regulation of the permeate flow and consequently varying cake porosity throughout the fiber surface. Easier removal of the alginate deposit is thought to be caused by a looser structure which is easier to remove than a compressed deposit on the round fibers.

As a conclusion, although initially differences in particle deposition and cake porosity can be observed on the structured fibers, permeation will tend to be regulated to pass more through low resistance areas and less through high resistance areas. This will lead to an equalization of the resistances all along the structured fiber surface and therefore is not expected to be detrimental to the overall fouling performance. Furthermore, as seen in sodium alginate filtrations, this self regulation can cause better fouling reversibility. On the whole, we observed that in dead-end filtrations, although the fouling resistances were somewhat higher for structured fibers, the fouling reversibility was better. In considering the higher resistances of the structured fibers, we must also note that due to the enhanced surface area, the actual permeate flow at a certain flux setpoint is 60% higher than that with the round fibers of equal length. This enhancement is more than the increased fouling resistance of these fibers, and thus results in enhanced productivity.

3.5 References

- [1] V. Chen, A.G. Fane, S. Madaeni and I.G. Wenten; *Particle deposition during membrane filtration of colloids: Transition between concentration polarization and cake formation*; Journal of Membrane Science **125** (1) (1997) 109–122
- [2] M. Elimelech and S. Bhattacharjee; *A novel approach for modeling concentration polarization in crossflow membrane filtration based on the equivalence of osmotic pressure model and filtration theory*; Journal of Membrane Science **145** (2) (1998) 223–241
- [3] M.F.A. Goosen, S.S. Sablani, H. Al-Hinai, S. Al-Obeidani, R. Al-Belushi and D. Jackson; *Fouling of reverse osmosis and ultrafiltration membranes: A critical review*; Separation Science and Technology **39** (10) (2004) 2261–2297

- [4] P. Bacchin, M. Meireles and P. Aimar; *Modelling of filtration: From the polarised layer to deposit formation and compaction*; *Desalination* **145** (1-3) (2002) 139–146
- [5] A.-S. Jönsson and B. Jönsson; *Ultrafiltration of colloidal dispersions - A theoretical model of the concentration polarization phenomena*; *Journal of Colloid and Interface Science* **180** (2) (1996) 504–518
- [6] P. Bacchin, D. Si-Hassen, V. Starov, M.J. Clifton and P. Aimar; *A unifying model for concentration polarization, gel-layer formation and particle deposition in cross-flow membrane filtration of colloidal suspensions*; *Chemical Engineering Science* **57** (1) (2002) 77–91
- [7] Y. Bessiere, N. Abidine and P. Bacchin; *Low fouling conditions in dead-end filtration: Evidence for a critical filtered volume and interpretation using critical osmotic pressure*; *Journal of Membrane Science* **264** (1-2) (2005) 37–47
- [8] W.J.C. van de Ven, K. van Sant, I.G.M. Pünt, A. Zwijnenburg, A.J.B. Kemperman, W.G.J. van der Meer and M. Wessling; *Hollow fiber dead-end ultrafiltration: Influence of ionic environment on filtration of alginates*; *Journal of Membrane Science* **308** (1-2) (2008) 218–229
- [9] V. Chen, H. Li and A.G. Fane; *Non-invasive observation of synthetic membrane processes - A review of methods*; *Journal of Membrane Science* **241** (1) (2004) 23–44
- [10] D. Airey, S. Yao, J. Wu, V. Chen, A.G. Fane and J.M. Pope; *An investigation of concentration polarization phenomena in membrane filtration of colloidal silica suspensions by NMR micro-imaging*; *Journal of Membrane Science* **145** (2) (1998) 145–158
- [11] S. Yao, M. Costello, A.G. Fane and J.M. Pope; *Non-invasive observation of flow profiles and polarisation layers in hollow fibre membrane filtration modules using NMR micro-imaging*; *Journal of Membrane Science* **99** (3) (1995) 207–216
- [12] P.Z. Çulfaz, E. Rolevink, C. van Rijn, R.G.H. Lammertink and M. Wessling; *Microstructured hollow fibers for ultrafiltration*; *Journal of Membrane Science* **347** (1-2) (2009) 32–41
- [13] S. Buetehorn, L. Utiu, M. Kueppers, B. Bluemich, T. Wintgens, M. Wessling and T. Melin; *Non-invasive observation of permeate flux distribution and local cake growth in submerged microfiltration processes via Nuclear Magnetic Resonance (NMR) imaging*; Manuscript submitted to *Journal of Membrane Science*
- [14] L. Utiu; *Functional NMR and MRI for analysis of materials*; Ph.D. thesis; RWTH

- Aachen University (2011)
- [15] S.-H. Yoon, S. Lee and I.-T. Yeom; *Experimental verification of pressure drop models in hollow fiber membrane*; Journal of Membrane Science **310** (1-2) (2008) 7–12
- [16] G. Belfort, R.H. Davis and A.L. Zydney; *The behavior of suspensions and macromolecular solutions in crossflow microfiltration*; Journal of Membrane Science **96** (1-2) (1994) 1–58
- [17] W.J.C. van de Ven, I.G.M. Pünt, A.J.B. Kemperman and M. Wessling; *Unraveling ultrafiltration of polysaccharides with flow field flow fractionation*; Journal of Membrane Science **338** (1-2) (2009) 67–74
- [18] W.R. Bowen and F. Jenner; *Dynamic ultrafiltration model for charged colloidal dispersions: A Wigner-Seitz cell approach*; Chemical Engineering Science **50** (11) (1995) 1707–1736
- [19] B. Sarkar, S. DasGupta and S. De; *Prediction of permeate flux during osmotic pressure-controlled electric field-enhanced cross-flow ultrafiltration*; Journal of Colloid and Interface Science **319** (1) (2008) 236–246
- [20] W.R. Bowen and P.M. Williams; *The osmotic pressure of electrostatically stabilized colloidal dispersions*; Journal of Colloid and Interface Science **184** (1) (1996) 241–250

Appendix: Calculation of the diffusion coefficient

The concentration-dependent diffusion coefficient of colloidal particles is estimated using the generalized Stokes-Einstein equation;

$$D(\phi) = \frac{V_p}{6\pi\mu a H(\phi)} \frac{d\Pi}{d\phi} \quad (3.3)$$

where the Happel function, $H(\phi)$, is

$$H(\phi) = \frac{6 + 4\phi^{5/3}}{6 - 9\phi^{1/3} + 9\phi^{5/3} - 6\phi^2} \quad (3.4)$$

The osmotic pressure can be estimated by adding up the entropic, electrostatic and van der Waals contributions [5, 6, 18, 19]:

$$\Pi(\phi) = \Pi_{entropy} + \Pi_{vanderWaals} + \Pi_{electrostatic} \quad (3.5)$$

$$\Pi_{entropy} = \frac{3kT}{4\pi a^3} \phi \frac{1 + \phi + \phi^2 + 0.67825\phi^3 - \phi^4 - 0.5\phi^5 - X\phi^6}{1 - 3\phi + 3\phi^2 - 1.04305\phi^3} \quad (3.6)$$

where $X = 6.2028 \exp\{[\phi_{cp} - \phi][7.9 - 3.9(\phi_{cp} - \phi)]\}$ with $\phi_{cp} = 0.74048$ for hexagonal close packing. k is the Boltzmann constant and T is the absolute temperature.

$$\Pi_{vanderWaals} = -\frac{z_n A}{48\pi a^3} \frac{\phi^3}{[\phi_{cp} - (\phi_{cp})^{1/3}\phi^{2/3}]^2} \quad (3.7)$$

where $z_n = 12$ for hexagonal close packing and A is the Hamaker constant.

$$\Pi_{electrostatic} = \frac{\sqrt{6}}{A_h} f(D_1) \quad (3.8)$$

$$A_h = 2\sqrt{3} \left(a + \frac{D_1}{2} \right)^2 \quad (3.9)$$

$$D_1 = \left[\left(\frac{4\pi\sqrt{2}}{3\phi} \right)^{\frac{1}{3}} (a + d) - 2a \right] \quad (3.10)$$

$$f(D_1) = \frac{1}{3} S_{cell} N_{avo} I k T (\cosh \Psi_{r_{cell}} - 1) \quad (3.11)$$

$$S_{cell} = 4\pi r_{cell}^2 \quad (3.12)$$

$$r_{cell} = (2a + D_1) \left(\frac{3}{4\pi\sqrt{2}} \right)^{\frac{1}{3}} \quad (3.13)$$

$$\Psi_{r_{cell}} = \frac{A_1}{\beta} e^{\beta-\alpha} + \frac{(\xi^1 \alpha - A_1)}{\beta} e^{-(\beta-\alpha)} \quad (3.14)$$

$$A_1 = \frac{\xi^1 \alpha e^{-2(\beta-\alpha)}}{\frac{\beta-1}{\beta+1} + e^{-2(\beta-\alpha)}} \quad (3.15)$$

$$\xi^1 = \frac{ez\xi}{kT} \quad (3.16)$$

where d is the distance to the surface of shear, N_{avo} is Avogadro's number, I is the ionic strength, κ^{-1} is the Debye length, $\alpha = \kappa(a + d)$, $\beta = \kappa r_{cell}$, e is the elementary charge, z is the valence of the ions in solution and ξ is the zeta potential.

Table 3.4: Data used in calculations

μ	0.001 Pa.s
A	6.51×10^{-21} J
ξ	- 55 mV
d (for Na ions)	0.23 nm [20]
I (Ludox, 0.1 wt%)	0.006 mol/m ³
I (Ludox, 0.9 wt%)	0.055 mol/m ³
I (Bindzil, 0.1 wt%)	0.155 mol/m ³
I (Bindzil, 0.9 wt%)	1.363 mol/m ³

CHAPTER 4

Fouling behavior of microstructured hollow fibers in cross-flow filtrations: Critical flux determination and direct visual observation of particle deposition

THIS CHAPTER HAS BEEN SUBMITTED FOR PUBLICATION:

P.Z. Çulfaz, M. Haddad, M. Wessling and R.G.H. Lammertink, *Fouling behavior of microstructured hollow fibers in cross-flow filtrations: Critical flux determination and direct visual observation of particle deposition*, Journal of Membrane Science

ABSTRACT

The fouling behavior of microstructured hollow fiber membranes was investigated in cross-flow filtrations of colloidal silica and yeast. In addition to the as-fabricated microstructured fibers, twisted fibers made by twisting the microstructured fibers around their own axes were tested and compared to round fibers. In silica filtrations, the three different fibers showed similar behavior and increasing Reynolds number increased the critical fluxes significantly. In yeast filtrations, the twisted fiber performed similar to the round fiber and better than the structured fiber. Among the three fibers, during yeast filtrations the critical flux for irreversibility was highest for the twisted fiber. The Reynolds number had little effect on the critical fluxes for particle deposition, which was attributed to the strong adsorption of yeast particles on the membrane. On the other hand, the critical fluxes for irreversibility increased with increasing Reynolds number for all three fibers. Direct visual observation of yeast particles on the surface of the three different hollow fibers revealed that for the structured and twisted fibers, the initial deposition rate on the fins is much lower than that in the grooves. This is attributed to the shear-induced migration of the yeast particles from areas of high shear (fins) to those of low shear (grooves). Furthermore, on the fins of the twisted fiber the deposition rate was lower than that on the fins of the structured fiber. This observation, together with the observed high critical fluxes for the twisted fiber led to the conclusion that the twisting induces a secondary flow in the liquid. This secondary flow is effective in depolarizing the buildup of micron-sized yeast particles since the diffusion of these particles are strongly effected by gradients in shear rate. On the other hand, for the silica colloids which are much smaller, shear-induced diffusion is not significant and twisting does not have an improving effect on filtration.

4.1 Introduction

The performance of pressure-driven membrane processes for liquid-phase separations is adversely effected by concentration polarization and subsequent membrane fouling. Membrane fouling is one of the most important problems in a membrane process as it increases operational costs and reduces membrane lifetime. There are two main approaches to mitigate membrane fouling. By suitable choice of the membrane material or modification of the membrane surface, the adsorption of foulants on the membrane can be minimized [1, 2]. However, this approach by itself is not enough to prevent fouling. Even though a membrane may be repulsive to potential foulants, retained material will still accumulate near the membrane and form a concentration polarization layer which can initiate the formation of a cake or gel layer [3]. The extent of concentration polarization and cake/gel formation ultimately depends on the balance between attractive and repulsive surface interactions of the filtered material, which is determined by the material's properties (e.g. size, surface charge), solution properties (e.g. pH, ionic strength, concentration) and the hydrodynamics (e.g. permeation rate, pressure, cross-flow velocity, shear rate) [1, 4]. The latter can be modified such that concentration polarization is alleviated and cake or gel formation is prevented.

By applying cross-flow over the membrane, part of the foulant that would otherwise buildup on the membrane can be swept away. Laminar flow decreases concentration polarization and compared to dead-end operation it becomes possible to carry out filtrations for extended periods without performance loss. Turbulent flow is more effective in diminishing the concentration polarization layer and preventing fouling and therefore enables the use of higher permeate fluxes. However the energy consumption is much higher than for laminar flow. To make use of the mixing effect of turbulence in disrupting concentration polarization layers without bringing about a high energy input, several approaches have been suggested, such as the use of turbulence promoters [5], two-phase flow [6], pulsatile flow [7], corrugated membranes [8–12] and curvature-induced fluid instabilities [13–16].

A number of studies in literature have shown that introducing corrugations that lie normal to the feed flow direction on flat sheet membranes can promote turbulence and reduce concentration polarization significantly [8–12]. Apart from corrugated surfaces and turbulence promoting structures, turbulence can be passively created

by curvature as well. Dean vortices, which are centrifugal instabilities formed in curved ducts, have been shown to depolarize foulant buildup during microfiltration and ultrafiltration in spiral, coiled, meander-shaped and helically twisted tubes or channels [13–16]. Broussous et al. fabricated ceramic tubular membranes with helical grooves on the inner surface and observed significant flux improvement compared to tubular membranes with smooth walls. They attributed this improved fouling performance to the flow disturbance by the helical structure [17, 18].

In Chapter 2, the fabrication of hollow fiber membranes with microstructured outer surfaces was described. It was shown that these membranes can be fabricated with the same intrinsic properties as round fibers fabricated under the same conditions. Therefore, they enable the same separation, and due to the microstructured surface they can offer enhanced productivity. In this chapter, we investigate the fouling performance of microstructured fibers in cross-flow filtrations. Additionally, by twisting the microstructured fibers around their axis we investigate the effect of having helical grooves that lie at an angle to the feed flow on the particle deposition. We use a flux-cycling method to determine the critical flux and direct visual observation to observe the deposition of yeast particles on the surface of the membranes. Both straight and twisted microstructured fibers are compared to round fibers with the same intrinsic properties.

4.2 Experimental

4.2.1 Membranes and modules

The structured and round fibers used were made by the dry-wet phase inversion of the polymer dope 16.6% PES, 4.91% PVP K30, 4.91% PVP K90, 7.18% H₂O, 66.32% NMP, with water as the external coagulant. Details of the fabrication can be found in Chapter 2 [19]. The structured fiber has 60% higher surface area per length compared to the round fiber. The pure water permeability of the fibers are 235 ± 11 L/h.m².bar and 233 ± 12 L/h.m².bar for structured and round fibers, respectively. The mean pore diameter of both fibers was found to be 12 nm by permoporometry measurements. In addition to the structured fibers, twisted fibers were made by twisting each structured fiber around its own axis with about one full turn in 5 cm. The twisting was done

after fabrication, when the fibers were dry. The pure water permeability and the pore size distribution remain unchanged after twisting. For flux-cycling experiments single-fiber modules of 40 cm length were prepared in 3 mm inner-diameter tubes. For direct visual observation (DVO), a flowcell made of three transparent PMMA plates was used. The top plate was 2 mm thick, while the bottom and middle plates were 1 cm thick. The middle plate had an opening of 3 cm × 28 cm in the middle, and three 6-mm diameter holes on the two ends for potting the fibers. 6 mm outer-diameter tubes were glued into these holes in the middle plate to pot the fibers and extract the permeate. Three fibers were placed with equal spacing in the flowcell.

4.2.2 Flux-cycling experiments

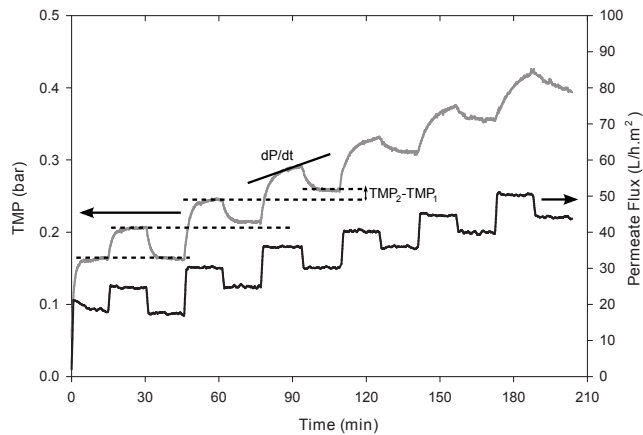


Figure 4.1: Example of TMP-flux behavior and the calculation of the fouling rate and degree of irreversibility

0.25 wt% Ludox-TMA colloidal silica (Sigma-Aldrich) and 0.025 wt% Baker's yeast, *Saccharomyces cerevisiae*, (dry active yeast of Dr. Oetker) was used as feed suspensions. The as-purchased yeast was washed, filtered and dried overnight under air flow before preparing the feed suspensions. A fresh feed suspension was prepared for each experiment.

Before each experiment the pure water permeability of the membranes was measured as a check of membrane integrity.

To determine the critical flux, a flux-cycling method was used (Figure 4.1) [20–22]. Flux steps of 5 L/h.m^2 were applied, each step lasting 15 minutes. Two critical fluxes were defined, one with respect to the onset of particle deposition and the other one regarding the reversibility of this deposition [23]. To determine the critical flux for particle deposition, the evolution of TMP at constant flux during upward flux steps was monitored. The slope of the TMP during the last five minutes of the flux step, where the increase of TMP was linear, was calculated and plotted as dP/dt versus permeate flux. The flux where dP/dt becomes nonzero was taken as the critical flux for particle deposition. The degree of fouling reversibility was assessed by comparing the TMP's at the same flux on the way up and down (Figure 4.1). For example, if the TMP on the way down is higher than that on the way up at 40 L/h.m^2 , then the critical flux for irreversibility was taken as 45 L/h.m^2 , as this is the flux step that caused irreversible deposition.

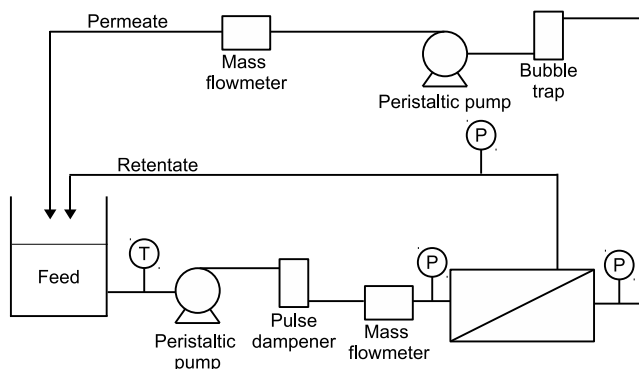


Figure 4.2: Schematic of the filtration setup

The experiments were done under laminar conditions with Reynolds numbers of 120 and 400. $Re=120$ corresponds to average cross flow velocities of 0.09 m/s for the structured and twisted fibers and 0.08 m/s for the round fiber. At $Re=400$, the cross flow velocity was 0.31 m/s for the structured and twisted fibers and 0.27 m/s for the round fiber.

The flux-cycling experiments were carried out in the setup shown in Figure 4.2. In this setup, the flowrates of feed and permeate as well as the pressures on the feed and permeate sides were logged every 5 seconds on a computer. The pressure on the retentate side was measured at the end of each experiment to calculate the TMP

taking into account the pressure drop along the module length. When the yeast suspension was used as the feed, the suspension was stirred mildly during the course of the experiment to prevent settling of the particles. The pulse dampener on the feed side was used only in experiments with silica colloids because yeast particles would settle inside the pulse dampener. The bubble trap on the permeate side was used to prevent degassing products from affecting the permeate flux setpoint and measurement.

4.2.3 Direct-visual observation (DVO) experiments

The direct-visual observation experiments were done in a setup similar to that used in flux-cycling experiments. Instead of computer-logging of the data, feed and permeate flowrates and the permeate pressure were manually checked several times during the experiment. A permeate flux of 55 L/h.m^2 and a Reynolds number of 120 was used. This Re corresponds to a lower velocity (11 mm/s) than that in the flux-cycling experiment modules as the hydraulic diameter was much larger in the flowcell. The permeate and retentate was recycled to the feed tank and each filtration was carried out for one hour. The surface of the membranes was observed with a NI 1744 Smart Camera (National Instruments) with a monochrome 1280×1024 CCD image sensor. The zoom system used (Optem Zoom 160, Qioptic Photonics) had a $2.0\times$ objective lens and $1.0\times$ dovetail tube, which allowed up to 16 times magnification with a 32 mm working distance. The resolution was 900 lp/mm or $1.11 \mu\text{m}$ and the depth-of-focus was $7 \mu\text{m}$ at the highest magnification. At the lowest magnification, the resolution was 54 lp/mm or $18.5 \mu\text{m}$ and the depth-of-focus was 1.75 mm. Illumination was done using fiber-optic bundles coaxially from behind the lens and outside, from above the observed area of the flow cell.

During filtration, 5 images with 1 second intervals were taken every 3 minutes. For the structured and twisted fibers, the zoomed area was switched manually from the bottom of the grooves and the top of the fins every 3 minutes, so that from each of these areas images were taken every 6 minutes. The images were analyzed to determine the fractional coverage of the membrane area with yeast particles using ImageJ.

A 0.005 wt% suspension of yeast cells in ultrapure water was used in the filtrations with DVO. The yeast cells were dyed with Coomassie Brilliant Blue R-250 (Acros)

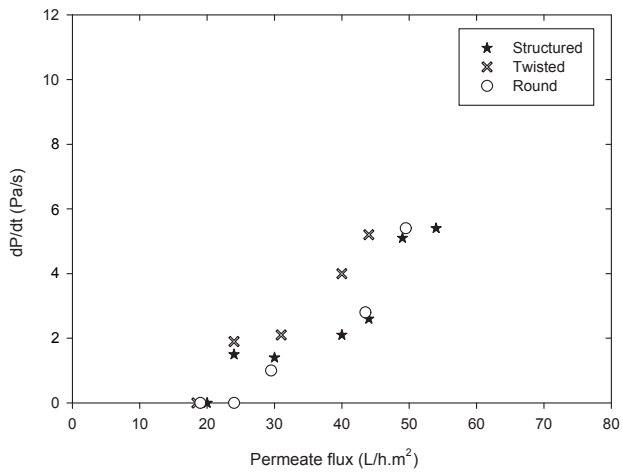


Figure 4.3: Fouling rate during silica filtration at $Re=120$

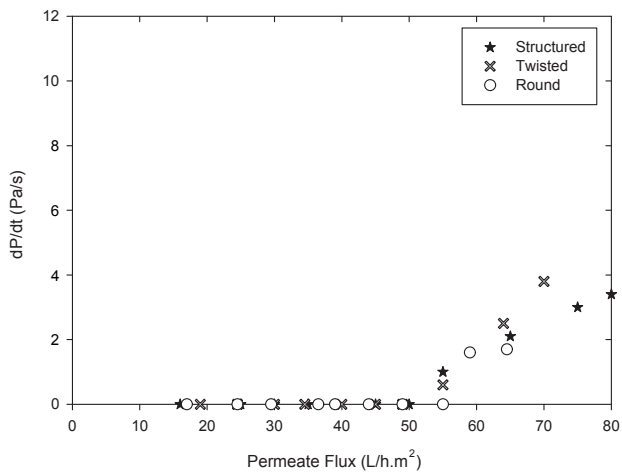


Figure 4.4: Fouling rate during silica filtration at $Re=400$

according to the procedure used by Kang et al. [24]. 1 gram of the as-purchased yeast was first diluted to 250 mL with ultrapure water and washed and centrifuged three times at 2500 rpm for 10 minutes, discarding the supernatant. The precipitated yeast was then dried and dispersed in a mixture of 0.15 gr Brilliant blue dye, 25 mL acetic acid, 62.5 mL isopropanol and 161.5 mL water. After mixing for 3 hours, the suspension was again centrifuged three times at 2500 rpm for 10 minutes, discarding the supernatant and redispersing the precipitate in ultrapure water each time. The final precipitate was dried for 24 hours under air flow.

4.3 Results and Discussion

4.3.1 Flux-cycling experiments

The experiments were done under laminar conditions with Reynolds numbers of 120 and 400. The reason for choosing Reynolds number instead of the cross-flow velocity as the fixed variable while comparing the different fibers is because Reynolds and Schmidt numbers determine the Sherwood number, which is the dimensionless number that characterizes the mass transfer behavior in this kind of systems [10, 25, 26]. As the feed concentrations and Schmidt numbers for colloidal silica particles and yeast are not the same, we cannot directly compare the behavior of these two feeds at the same Reynolds number. However, for a single feed suspension, at fixed Reynolds number, we can compare the effect of the microstructure and twist in the fibers on the mass transfer.

As explained before in section 4.2.2, to assess fouling reversibility we increase the permeate flux by 5 L/h.m², then reduce it to the flux step before and compare the TMPs before and after the increased flux step. We must note here that assigning whether or not the fouling is reversible depends on the method used to reverse the particle deposition. Backwashing, increasing cross-flow or continuing cross-flow while stopping permeation are some of the ways that can be used to resuspend the particles on the membrane to the bulk [27–29]. The degree of reversibility depends on which method is used, and the intensity of the method, i.e. backwash flux, cross-flow velocity, etc.. As the 5 L/h.m² decrease in flux is only a mild relaxation, what is found to be irreversible fouling in these experiments can still be reversible with other methods

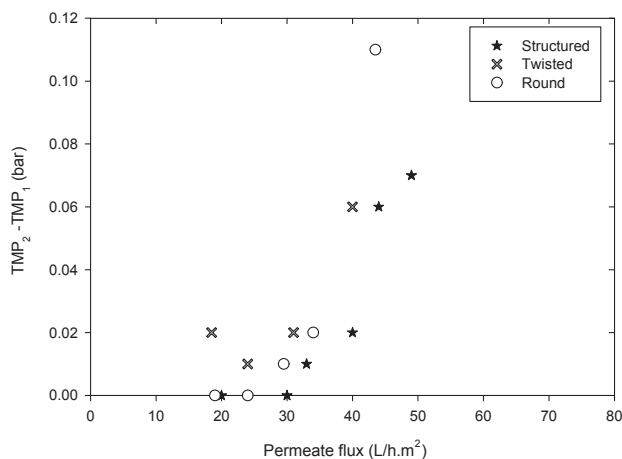


Figure 4.5: Fouling irreversibility during silica filtration at $Re=120$

mentioned before. However, it can distinguish between a loose, dynamic polarization layer and a stagnant cake [23, 30]

4.3.1.1 Colloidal silica filtration

During the filtrations of the silica sol, for both Reynolds numbers, particle deposition started at a lower flux for both the structured and twisted fibers compared to the round fibers (Figures 4.3 and 4.4). After this critical flux where the first particle deposition was observed by an increasing TMP, the particle deposition rate (as deduced from the dP/dt) was higher for the twisted fiber compared to the structured fiber. On the other hand, although particle deposition took place earlier in the structured fiber compared to the round one, at fluxes higher than the critical flux, the rate of particle deposition was similar for the two fibers.

In the structured fibers, when the feed flow is parallel to the direction of the grooves in the fiber, within these grooves the shear rate will be lower than that on the fins. The result of this is that concentration polarization is more intense, which causes the particle deposition to start first within the grooves. Nevertheless, after an initial deposition in the grooves, the deposition appears to be similar for the structured and round fibers.

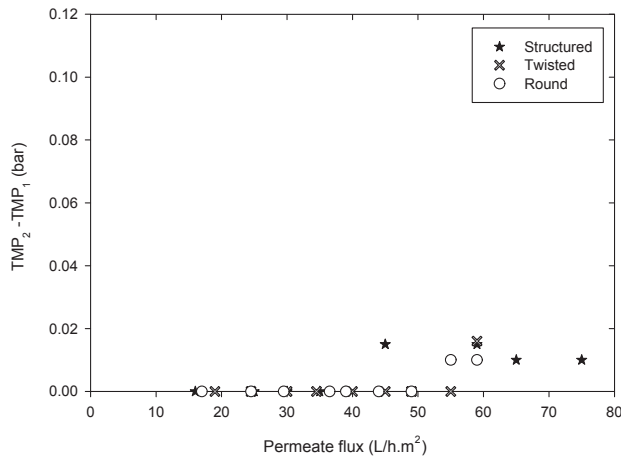


Figure 4.6: Fouling irreversibility during silica filtration at $Re=400$

At $Re=120$, the twisted fibers foul faster and more irreversibly than the structured and round fibers. In Chapter 3, we mentioned inhomogeneous deposition of this silica sol on the structured fibers in dead-end filtrations and attributed this to the concentration profile in the thick polarization layers. However, in cross-flow filtrations, the concentration polarization layers are expected to be much thinner. For the twisted fiber, due to the secondary flows that might result from the twisted surface one would expect more mixing and decreased concentration polarization. As will be explained in more detail later, at low Re only corner vortices form while after a critical Re these turn into Dean vortices, which are more effective in depolarizing the particle buildup [31]. If the effect of the secondary flow is little, then in the grooves of the twisted fibers it may only be able to homogenize the present concentration polarization layer without carrying particles out of the groove and back to the bulk.

At $Re=120$, the critical flux for irreversibility is higher than the critical flux for particle deposition for the structured fibers unlike for the twisted and round fibers (Figure 4.11). Although particle deposition starts in the grooves, when the flux is lowered, more of the permeate would flow towards the fins due to the higher resistance in the grooves. This balancing between the different local fluxes through the fins and the grooves can keep the fouling appear reversible until a similar deposit forms on the fins.

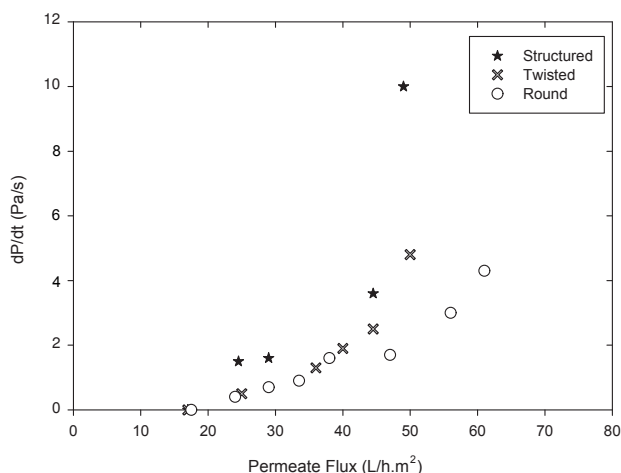


Figure 4.7: Fouling rate during yeast filtration at $Re=120$

At $Re=400$, although some irreversibility is observed for all three fibers, the TMP differences remain lower than 0.01 bar for the whole flux range, which is close to the detection limit of the pressure sensors (0.005 bar).

4.3.1.2 Yeast filtration

During the filtrations of the yeast suspension, there is a clear difference between the fouling behavior of structured and twisted fibers (Figures 4.7-4.10). At both Reynolds numbers, both the critical flux for particle deposition and for irreversibility are higher for the twisted fiber. The particle deposition rate is similar for twisted and round fibers, except for fluxes higher than 40 L/h.m² at $Re=120$. On the other hand, for the structured fiber, the particle deposition is faster at both Re throughout the whole flux range. Twisting the structured fibers also improves the reversibility of particle deposition, as at both Reynolds numbers, the critical flux for irreversible deposition is highest on the twisted fibers (Figure 4.12).

At $Re=120$, the degree of irreversibility is significantly higher on the structured fiber compared to the twisted and round fibers. For these latter fibers it is mostly similar after their critical fluxes for irreversible deposition. Increasing the Reynolds number

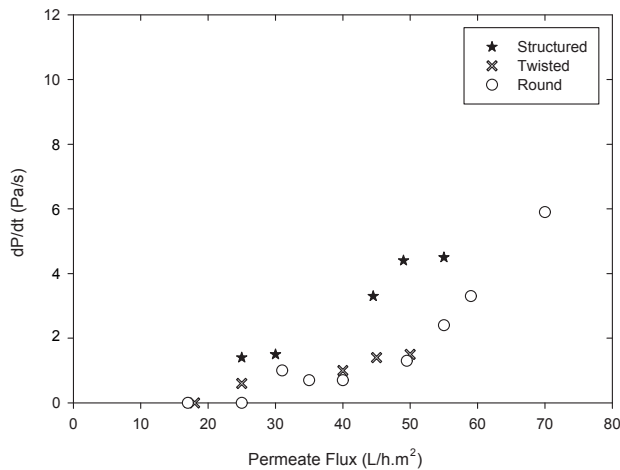


Figure 4.8: Fouling rate during yeast filtration at $Re=400$

improves the fouling reversibility for all the fibers (Figure 4.12).

Increasing the Reynolds number from 120 to 400 increases the critical fluxes about two-fold for all three fibers during silica filtration (Figure 4.11). During yeast filtration the critical flux is affected much less or not affected at all (Figure 4.12). For the structured and twisted fibers, the critical flux for particle deposition during yeast filtration is 25 L/h.m^2 at both Re and for the round fiber it only increases from 25 L/h.m^2 to 30 L/h.m^2 with increasing Re . Although the effect of Reynolds number on the critical flux for irreversibility is slightly more pronounced, it is still less than its effect during silica filtrations. Particle deposition rates and the degree of irreversibility with increasing flux are less at the higher Reynolds number. However, the critical fluxes where particle deposition first occurs (and is irreversible) are quite low in all cases of yeast filtration. This behavior is probably due to the stronger adsorption of yeast particles on the membrane [24, 32]. On the other hand, considering the particle deposition rate and reversibility of deposition, twisting the structured fibers results in a clear improvement during yeast filtration, while during silica filtration the differences between all three fibers is much less.

For the colloidal silica particles, the main depolarization mechanism is the entropic back-diffusion [4]. In Chapter 3, it was shown that in the absence of cross-flow the

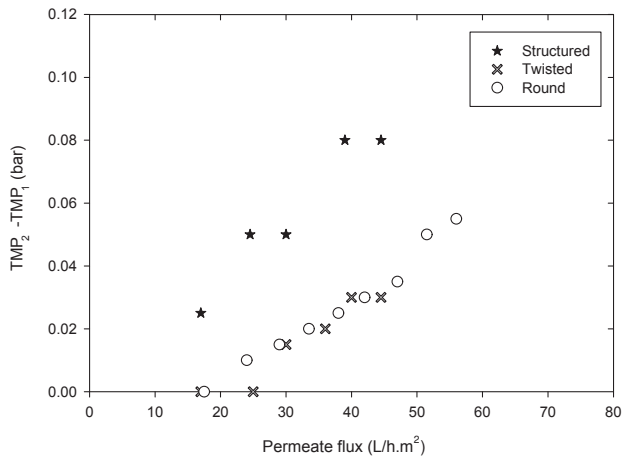


Figure 4.9: Fouling irreversibility during yeast filtration at $Re=120$

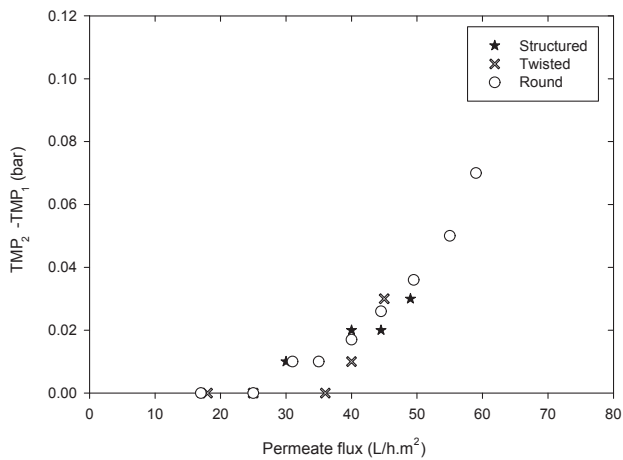


Figure 4.10: Fouling irreversibility during yeast filtration at $Re=400$

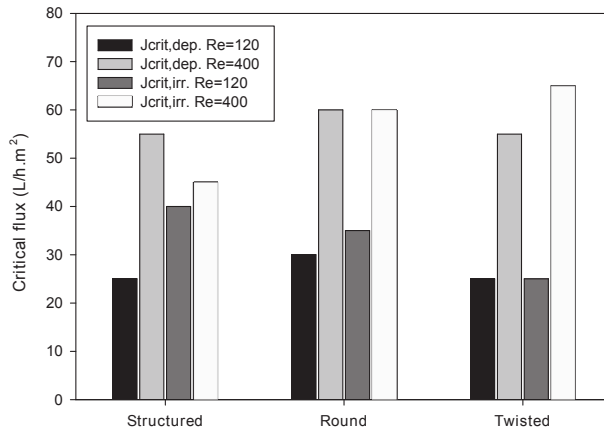


Figure 4.11: Critical flux for particle deposition and irreversibility for silica filtration

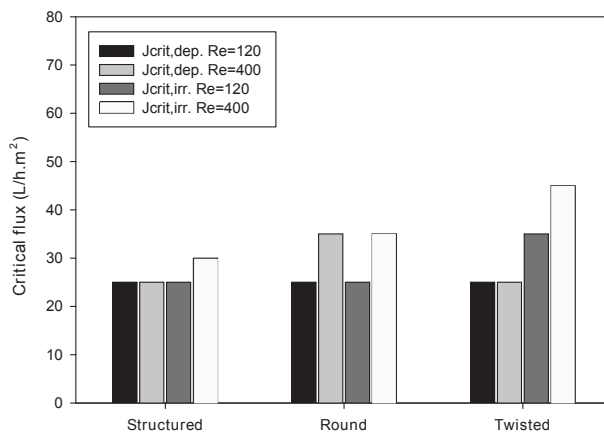


Figure 4.12: Critical flux for particle deposition and irreversibility for yeast filtration

concentration polarization layers with silica colloids can be as thick as the size of the convolutions in the structured fibers and this can give rise to inhomogeneous deposition patterns on the structured fibers. Although under the cross-flow conditions used here, the concentration polarization layers are thinner and probably do not create such inhomogeneous deposition patterns, they can still have significant resistance. The improvement in critical flux obtained with increasing Reynolds number for the silica filtrations is considered to be because increasing cross-flow suppresses polarization and therefore delays fouling.

For the micron-sized yeast particles, electrostatic repulsion and shear-induced diffusion are the main depolarization mechanisms [4, 24, 33]. The high shear-induced diffusivity can create a very thick concentration polarization layer. However the resistance of this layer would be very low (which can be deduced from the Kozeny-Carman relation or the low osmotic pressure), so the effect of the polarization layer would not be significant. In yeast filtrations, fouling starts to occur at low fluxes due to adsorption on the membrane surface. However, considering the whole flux range increasing shear decreases the particle deposition rates and the irreversibility of the deposit.

The difference between the structured and twisted fibers during yeast filtrations is attributed to secondary flows induced by the twisting. In general, when the flow direction is not parallel to the solid surface, the imbalance between viscous forces and centrifugal forces originating from the curvature of the surface creates secondary flows and forms vortices in the fluid. These vortices, which are called corner vortices or Ekman cells at low Re and Dean vortices after a critical Re , have been used to decrease concentration polarization in membrane processes and to improve mixing in microfluidic channels [14–16, 31, 34–36]. For the twisted fiber, although we do not have a fully coiled or helical channel, the twisting of the corrugations creates a helical half-channel. The Dean numbers calculated for $Re=120$ and 400 are 4 and 14 , respectively. A critical Dean number below which Dean vortices do not occur has been identified by several authors [14, 15]. On the other hand, Moulin et al. have shown that secondary flows occur even at very low Dean numbers, although they might not have clearly observable effects in the mass transfer [37]. Mallubhotla et al. suggest that in helical channels, the critical condition where the secondary flow pattern changes from a single pair of counter-rotating corner vortices to two pairs of vortices, which are called Dean vortices, depends on two dimensionless quantities, namely the

Dean number and the Germano number [15]. According to the criteria they suggest, if we would assume that in the half channels of the twisted fiber same criteria would hold as in twisted tubes of the same dimensions, at $Re=400$ Dean vortices might form. Although it is difficult to say if this actually happens or not, even in the case of corner vortices that form due to the twisting, the higher shear rates and shear rate gradients can affect the back diffusion of yeast particles.

4.3.2 Direct visual observation of yeast deposition

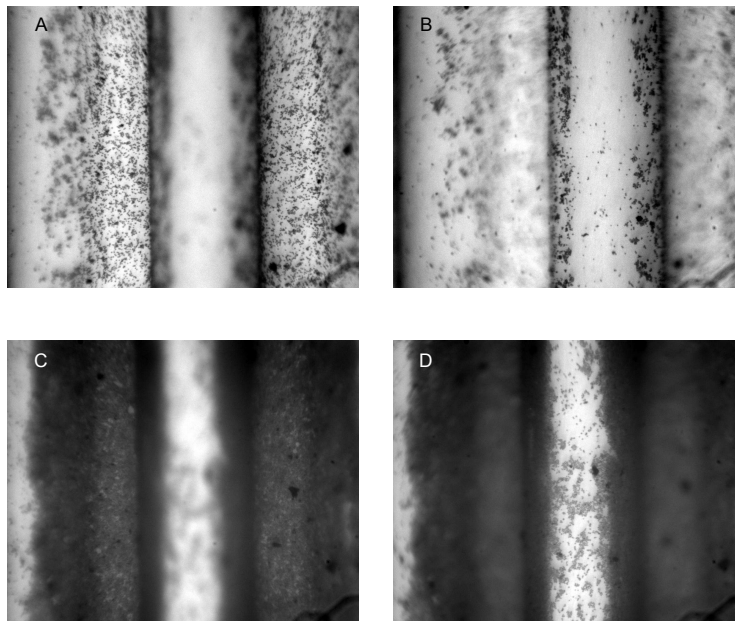


Figure 4.13: Images of the structured fiber surface during filtration of the yeast suspension. Bottom of grooves (a) after 9 min and (c) after 57 min. Top of fins (b) after 6 min and (d) after 60 min.

From the images taken during yeast filtration, it is observed that for both structured and twisted fibers the particle deposition rate is lower on the fins (Figures 4.13 and 4.14, (b) and (d)). This can be attributed to the higher shear rate on the fins, which allows less deposition. On the twisted fibers, the deposition rate on the fins is even lower than that of the structured fiber. Also, the particles appear to deposit in patches both in the grooves and on the fins on the twisted fiber, whereas on the structured

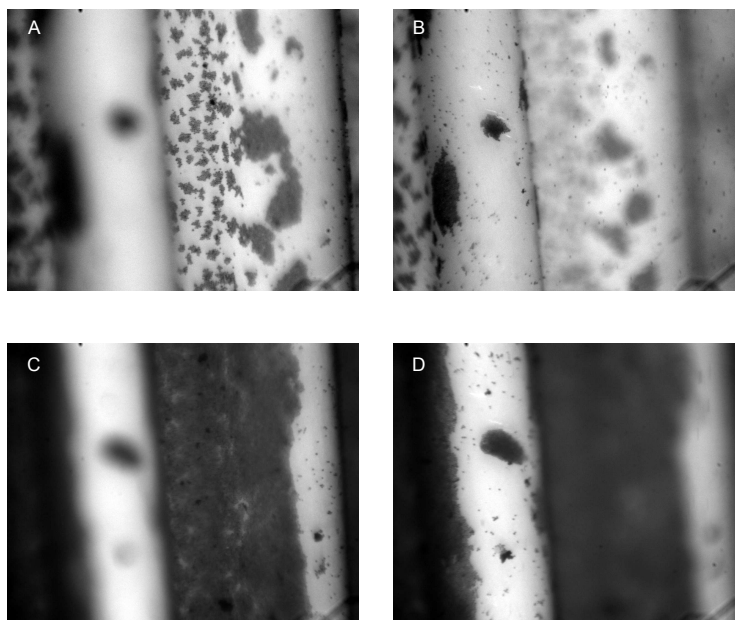


Figure 4.14: Images of the twisted fiber surface during filtration of the yeast suspension. Bottom of grooves (a) after 9 min and (c) after 57 min. Top of fins (b) after 6 min and (d) after 60 min.

fiber and the round fiber (images not shown here) the particles appear more randomly distributed over the whole surface. This aggregation can be due to the shear induced by secondary flows due to the twist [38–40]. It can also explain the better reversibility of fouling for the twisted fibers observed during the flux-cycling experiments, as clusters of particles are more easily swept away by the cross-flow as compared to individual particle deposits [27, 41]. This patchy deposition and the observation that on the fins of the twisted fibers there is less overall deposition is attributed to secondary flows forming due to the twist in the fiber surface.

Analysis of the images taken during filtration reveal that the particle deposition rate in the grooves of the structured and twisted fibers and that on the round fiber are similar (Figure 4.15). This seems unexpected at first thought, as the shear rate on the round fiber surface is similar to the shear rate on the fins of the structured fibers, which is higher than that in the grooves. Furthermore, even at Reynolds numbers as low as 10, on structured and twisted fibers the deposition rate on the fins was observed to be lower than that within the grooves. As the grooves fill up in time, the deposition

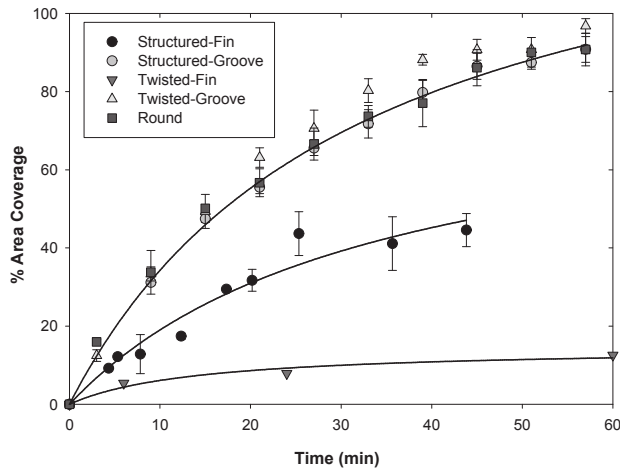


Figure 4.15: % Area coverage in time during yeast filtration

advances towards the fins from the sides towards the top. In dead-end filtrations, a homogeneous deposition was observed on fins and grooves. This can be explained by the shear-induced migration of particles in concentrated suspensions from high to low shear rate regions [33, 42]. For the round fibers the shear rate gradient is from the surface of the fiber towards the bulk. On the other hand, for the structured fibers the shear rate also increases from the grooves towards the fins and for the twisted fibers it varies within the vortices. In addition to the shear rate gradients, Kim et al. suggest that in suspensions under shear, particles also migrate due to curvature in the radially outward direction, which can also cause less particle deposition on the fins of the structured and twisted fibers [43].

4.4 Conclusions

The fouling behavior of microstructured hollow fiber membranes was investigated in cross-flow filtrations of colloidal silica and yeast. These microstructured fibers were compared to round fibers with the same intrinsic properties. Also the effect of twisting the microstructured fibers around their own axes on the particle deposition is investigated. During silica filtrations, the three different fibers showed similar behavior

and increasing Reynolds number increased the critical fluxes significantly. During yeast filtrations, the twisted fiber performed better than the structured fiber and similar to the round fiber. Among the three fibers, during yeast filtrations the critical flux for irreversibility was highest for the twisted fiber. The Reynolds number had little effect on the critical fluxes for particle deposition, which was attributed to the strong adsorption of yeast particles on the membrane. On the other hand, the critical fluxes for irreversibility increased with increasing Reynolds number for all three fibers. In direct visual observation experiments using yeast particles, we observed that on the fins of the structured and twisted fibers, the initial deposition rate is much lower than that in the grooves. This is mainly attributed to the shear-induced migration of the yeast particles from areas of high shear (fins) to those of low shear (grooves). Furthermore, the particle deposition rate on the fins of the twisted fiber was lower than that on the fins of the structured fiber. This observation, together with the observed high critical fluxes for the twisted fiber led to the conclusion that the twisted surface promotes secondary flows. These secondary flows can depolarize the buildup of micron-sized yeast particles since the diffusion of these particles are highly effected by gradients in shear rate. On the other hand, as shear-induced diffusion is not significant for the smaller silica colloids twisting does not have an improving effect on filtration.

4.5 References

- [1] N. Hilal, O.O. Ogunbiyi, N.J. Miles and R. Nigmatullin; *Methods employed for control of fouling in MF and UF membranes: A comprehensive review*; Separation Science and Technology **40** (10) (2005) 1957–2005
- [2] D. Rana and T. Matsuura; *Surface modifications for antifouling membranes*; Chemical Reviews **110** (4) (2010) 2448–2471
- [3] H.B. Winzeler and G. Belfort; *Enhanced performance for pressure-driven membrane processes: The argument for fluid instabilities*; Journal of Membrane Science **80** (1993) 35–48
- [4] P. Bacchin, D. Si-Hassen, V. Starov, M.J. Clifton and P. Aimar; *A unifying model for concentration polarization, gel-layer formation and particle deposition in cross-flow membrane filtration of colloidal suspensions*; Chemical Engineering Science **57** (1) (2002) 77–91

- [5] D.M. Krstic, M.N. Tekic, M.D. Caric and S.D. Milanovic; *The effect of turbulence promoter on cross-flow microfiltration of skim milk*; Journal of Membrane Science **208** (1-2) (2002) 303–314
- [6] Z.F. Cui, S. Chang and A.G. Fane; *The use of gas bubbling to enhance membrane processes*; Journal of Membrane Science **221** (1-2) (2003) 1–35
- [7] J.A. Howell, R.W. Field and D. Wu; *Yeast cell microfiltration: Flux enhancement in baffled and pulsatile flow systems*; Journal of Membrane Science **80** (1993) 59–72
- [8] J. Balster, M.H. Yildirim, D.F. Stamatialis, R. Ibanez, R.G.H. Lammertink, V. Jordan and M. Wessling; *Morphology and microtopology of cation-exchange polymers and the origin of the overlimiting current*; Journal of Physical Chemistry B **111** (9) (2007) 2152–2165
- [9] K. Scott, A.J. Mahmood, R.J. Jachuck and B. Hu; *Intensified membrane filtration with corrugated membranes*; Journal of Membrane Science **173** (1) (2000) 1–16
- [10] N. Tzanetakis, K. Scott, W.M. Taama and R.J.J. Jachuck; *Mass transfer characteristics of corrugated surfaces*; Applied Thermal Engineering **24** (13) (2004) 1865–1875u
- [11] M.J. van der Waal, S. Stevanovic and I.G. Racz; *Mass transfer in corrugated-plate membrane modules. II. Ultrafiltration experiments*; Journal of Membrane Science **40** (2) (1989) 261–275
- [12] L.-Z. Zhang; *Convective mass transport in cross-corrugated membrane exchangers*; Journal of Membrane Science **260** (1-2) (2005) 75–83
- [13] M.E. Brewster, K.-Y. Chung and G. Belfort; *Dean vortices with wall flux in a curved channel membrane system. 1. A new approach to membrane module design*; Journal of Membrane Science **81** (1-2) (1993) 127–137
- [14] J.N. Ghogomu, C. Guigui, J.C. Rouch, M.J. Clifton and P. Aptel; *Hollow-fibre membrane module design: Comparison of different curved geometries with Dean vortices*; Journal of Membrane Science **181** (1) (2001) 71–80
- [15] H. Mallubhotla, S. Hoffmann, M. Schmidt, J. Vente and G. Belfort; *Flux enhancement during dean vortex tubular membrane nanofiltration. 10. Design, construction and system characterization*; Journal of Membrane Science **141** (2) (1998) 183–195
- [16] H. Mallubhotla, E. Nunes and G. Belfort; *Microfiltration of yeast suspensions with self-cleaning spiral vortices: Possibilities for a new membrane module design*;

- Biotechnology and Bioengineering **48** (4) (1995) 375–385
- [17] L. Broussous, J.C. Ruiz, A. Larbot and L. Cot; *Stamped ceramic porous tubes for tangential filtration*; Separation and Purification Technology **14** (1-3) (1998) 53–57
- [18] L. Broussous, P. Schmitz, H. Boisson, E. Prouzet and A. Larbot; *Hydrodynamic aspects of filtration antifouling by helically corrugated membranes*; Chemical Engineering Science **55** (21) (2000) 5049–5057
- [19] P.Z. Çulfaz, E. Rolevink, C.J.M. van Rijn, R.G.H. Lammertink and M. Wessling; *Microstructured hollow fibers for ultrafiltration*; Journal of Membrane Science **347** (1-2) (2009) 32–41
- [20] P. Bacchin, P. Aimar and R.W. Field; *Critical and sustainable fluxes: Theory, experiments and applications*; Journal of Membrane Science **281** (1-2) (2006) 42–69
- [21] S. Metsamuuronen, J. Howell and M. Nystrom; *Critical flux in ultrafiltration of myoglobin and baker's yeast*; Journal of Membrane Science **196** (1) (2002) 13–25
- [22] D. Wu, J.A. Howell and R.W. Field; *Critical flux measurement for model colloids*; Journal of Membrane Science **152** (1) (1999) 89–98
- [23] V. Chen, A.G. Fane, S. Madaeni and I.G. Wenten; *Particle deposition during membrane filtration of colloids: Transition between concentration polarization and cake formation*; Journal of Membrane Science **125** (1) (1997) 109–122
- [24] S.-T. Kang, A. Subramani, E.M.V. Hoek, M.A. Deshusses and M.R. Matsumoto; *Direct observation of biofouling in cross-flow microfiltration: Mechanisms of deposition and release*; Journal of Membrane Science **244** (1-2) (2004) 151–165
- [25] P. Pradanos, J.I. Arribas and A. Hernandez; *Mass transfer coefficient and retention of PEGs in low pressure cross-flow ultrafiltration through asymmetric membranes*; Journal of Membrane Science **99** (1) (1995) 1–20
- [26] F.P. Incropera, D.P. DeWitt; *Fundamentals of Heat and Mass Transfer* (2002); Wiley, New York
- [27] H. Li, A.G. Fane, H.G.L. Coster and S. Vigneswaran; *Observation of deposition and removal behaviour of submicron bacteria on the membrane surface during crossflow microfiltration*; Journal of Membrane Science **217** (1-2) (2003) 29–41
- [28] Y. Marselina, Lifia, P. Le-Clech, R.M. Stuetz and V. Chen; *Characterisation of membrane fouling deposition and removal by direct observation technique*; Journal of Membrane Science **341** (1-2) (2009) 163–171

- [29] W.D. Mores and R.H. Davis; *Yeast-fouling effects in cross-flow microfiltration with periodic reverse filtration*; Industrial and Engineering Chemistry Research **42** (1) (2003) 130–139
- [30] Y. Bessiere, N. Abidine and P. Bacchin; *Low fouling conditions in dead-end filtration: Evidence for a critical filtered volume and interpretation using critical osmotic pressure*; Journal of Membrane Science **264** (1-2) (2005) 37–47
- [31] H. Fellouah, C. Castelain, A. Ould El Moctar and H. Peerhossaini; *A criterion for detection of the onset of Dean instability in Newtonian fluids*; European Journal of Mechanics, B/Fluids **25** (4) (2006) 505–531
- [32] S. Wang, G. Guillen and E.M.V. Hoek; *Direct observation of microbial adhesion to membranes*; Environmental Science and Technology **39** (17) (2005) 6461–6469
- [33] G. Belfort, R.H. Davis and A.L. Zydney; *The behavior of suspensions and macromolecular solutions in crossflow microfiltration*; Journal of Membrane Science **96** (1-2) (1994) 1–58
- [34] M. Lopez and M.D. Graham; *Enhancement of mixing and adsorption in microfluidic devices by shear-induced diffusion and topography-induced secondary flow*; Physics of Fluids **20** (5)
- [35] A.D. Stroock, S.K.W. Dertinger, A. Ajdari, I. Mezic, H.A. Stone and G.M. Whitesides; *Chaotic mixer for microchannels*; Science **295** (5555) (2002) 647–651
- [36] A.D. Stroock, S.K. Dertinger, G.M. Whitesides and A. Ajdari; *Patterning flows using grooved surfaces*; Analytical Chemistry **74** (20) (2002) 5306–5312
- [37] P. Moulin, P. Manno, J.C. Rouch, C. Serra, M.J. Clifton and P. Aptel; *Flux improvement by Dean vortices: Ultrafiltration of colloidal suspensions and macromolecular solutions*; Journal of Membrane Science **156** (1) (1999) 109–130
- [38] Y. Kikuchi, H. Yamada, H. Kunimori, T. Tsukada, M. Hozawa, C. Yokoyama and M. Kubo; *Aggregation behavior of latex particles in shear flow confined between two parallel plates*; Langmuir **21** (8) (2005) 3273–3278
- [39] P. Stamberger; *The mechanical stability of colloidal dispersions*; Journal of Colloid Science **17** (2) (1962) 146–154
- [40] D.L. Swift and S.K. Friedlander; *The coagulation of hydrosols by brownian motion and laminar shear flow*; Journal of Colloid Science **19** (7) (1964) 621–647
- [41] Y.P. Zhang, A.G. Fane, A.W.K. Law; *Critical flux and particle deposition of fractal*

- flocs during crossflow microfiltration*; Journal of Membrane Science **353** (1-2) (2010) 28–35
- [42] R.J. Phillips, R.C. Armstrong, R.A. Brown, A.L. Graham and J.R. Abbott; *A constitutive equation for concentrated suspensions that accounts for shear-induced particle migration*; Physics of Fluids A **4** (1) (1992) 30–40
- [43] J.M. Kim, S.G. Lee and C. Kim; *Numerical simulations of particle migration in suspension flows: Frame-invariant formulation of curvature-induced migration*; Journal of Non-Newtonian Fluid Mechanics **150** (2-3) (2008) 162–176

CHAPTER 5

Fouling behavior of microstructured hollow fiber membranes in submerged and aerated filtrations

THIS CHAPTER HAS BEEN SUBMITTED FOR PUBLICATION:

P.Z. Çulfaz, M. Wessling and R.G.H. Lammertink, *Fouling behavior of microstructured hollow fiber membranes in submerged and aerated filtrations*, Water Research

ABSTRACT

The performance of microstructured hollow fiber membranes in submerged and aerated systems was investigated using colloidal silica as a model foulant. The microstructured fibers were compared to round fibers and to twisted microstructured fibers in flux-stepping experiments. The fouling resistances in the structured fibers were found to be higher than those of round fibers. This was attributed to stagnant zones in the grooves of the structured fibers. As the bubble sizes were larger than the size of the grooves of the structured fibers, it is possible that neither the bubbles nor the secondary flow caused by the bubbles can reach the bottom parts of the grooves. Twisting the structured fibers around their axes resulted in decreased fouling resistances. Large, cap-shaped bubbles and slugs were found to be the most effective in fouling removal, while small bubbles of sizes similar to the convolutions in the structured fiber did not cause an improvement in these fibers. Modules in a vertical orientation performed better than horizontal modules when coarse bubbling was used. For small bubbles, the difference between vertical and horizontal modules was not significant. When the structured and twisted fibers were compared to round fibers with respect to the permeate flowrate produced per fiber length instead of the actual flux through the convoluted membrane area, they showed lower fouling resistance than round fibers. This is because the enhancement in surface area is more than the increase in resistance caused by stagnant zones in the grooves of the structured fibers. From a practical point of view, although the microstructure does not promote further turbulence in submerged and aerated systems, it can still be possible to enhance productivity per module with the microstructured fibers due to their high surface area-to-volume ratio.

5.1 Introduction

Membrane bioreactor (MBR) technology, which combines the activated sludge process in wastewater treatment with membrane separation, offers an attractive alternative for the conventional wastewater treatment process [1–3]. The most important advantages offered by MBRs are smaller footprint, high product quality and lower waste production [4–7]. Although the MBR process has found widespread use in wastewater treatment in the recent years, performance decline due to membrane fouling still remains the biggest challenge facing further development and application of this technology [4, 5, 7].

In membrane bioreactors, air bubbles which are supplied to the reactor to provide dissolved oxygen for the microorganisms and to maintain the solids in suspension also serve the purpose of reducing fouling. This is due to the shear created on the surface of the membranes as a result of the liquid flow caused by bubbles, the scouring action of the bubbles themselves, the secondary flows they induce in the liquid and the fiber movement induced by the passing bubbles [8]. Although aeration is a very effective way of reducing fouling, it also forms the main component of the operating costs [3, 5, 9]. Periodic backwashing or intermittent operation, which serves to relax the cake layer on the membranes during the time permeation is stopped, are other ways of preventing fouling. However both decrease the amount of permeate produced. In addition to these, filtration needs to be carried out below the “critical flux” or at a “sustainable flux”, at which no or little fouling occurs [5, 10]. This limits the productivity in the sense that the permeate flow is kept at a low value. However, due to reduced fouling this value can be sustained for a longer time.

In submerged membrane bioreactors, where the membranes are immersed directly in the bioreactor, either flat sheet or hollow fiber membranes are used. Although the operation of flat sheet membranes is simpler due to better control over the hydrodynamics in the more well-defined geometry of the modules, hollow fiber membranes are less expensive to produce, backflushable and offer higher packing density [8, 11]. Increasing the membrane area per module volume can reduce the module production cost significantly and is highly desired [2].

In Chapter 2, the fabrication of hollow fiber ultrafiltration membranes with a microstructured outer surface was described [12]. The membrane surface area in a

given volume could be increased by up to 90%, and due to the increased area of the membranes' skin layer this was shown to increase the productivity of the fibers. In this chapter, we report the performance of these microstructured hollow fibers in a submerged system with aeration, operated in different configurations, in comparison to round fibers with the same intrinsic properties.

5.2 Experimental

Microstructured and round hollow fiber membranes made by the dry-wet phase inversion of the polymer dope 16.6% PES, 4.91% PVP K30, 4.91% PVP K90, 7.18% H₂O, 66.32% NMP were used throughout this study. Details of the fabrication can be found in Chapter 2. The structured fiber has 60% higher surface area per volume compared to the round fiber. The pure water permeability of the fibers are 235 ± 11 L/h.m².bar and 233 ± 12 L/h.m².bar for structured and round fibers, respectively. The mean pore diameter of both fibers was found to be 12 nm by permoporometry.

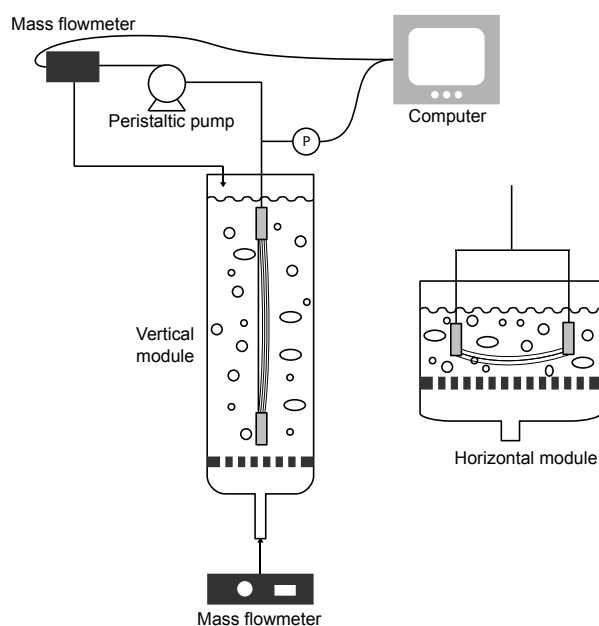


Figure 5.1: Experimental setup

The twisted membranes were made by twisting the structured fibers around their own axes, approximately one full turn per 10 cm. In the vertical module orientation, a steel tube was placed at the side of the fiber bundle to support the bundle. The fibers were fixed at the top and bottom ends and could move freely otherwise. The experimental setup, with drawings of both the vertical and horizontal module orientation is shown in Figure 5.1. Coarse bubbles were created by a perforated metal plate with 1 mm holes. Fine bubbles were created by a fritted ceramic plate with a nominal pore size of 0.1 mm.

The feed solution was 2 wt% Ludox-TMA colloidal silica (Sigma-Aldrich). The stock solution has 34 wt% silica in deionized water, with pH of 6-7.

5.2.1 Flux-stepping Experiments

In the flux-stepping method used, the permeate fluxes were stepwise increased and then decreased back in the same steps while recording the transmembrane pressure difference (TMP). Each flux step was continued for 20 minutes. To be able to compare whether the convolutions in the structured fiber have an improving effect on the hydrodynamics around the membrane, the permeate fluxes were set using the actual (convoluted, and therefore enhanced) surface area of the structured fibers. In the rest of the text, permeate flux refers to this flux calculated as the permeate flowrate through the actual surface area of the fibers. On the other hand, normalized permeate flux was calculated using the area of the circle passing through the middle of the fins for the structured fibers [12]. The latter is used to compare the fibers from a practical point of view, i.e. to compare the permeate volume that would be produced from the same module volume of round and structured fibers.

The fouling resistance was calculated using Darcy's law, expressing the total resistance during filtration as a resistance-in-series:

$$R_f = \frac{\text{TMP}}{\eta J_{\text{per}}} - R_m \quad (5.1)$$

where R_f is the fouling resistance which includes concentration polarization and/or particle deposition and R_m is the intrinsic membrane resistance determined by the pure water permeability.

5.3 Results and Discussion

Figure 5.2 shows the coarse and fine bubbles produced at different aeration rates. With the coarse bubbler, the bubbles formed had diverse size and shapes, from spherical to ellipsoid and cap-shaped. At 0.026 and 0.060 $\text{m}^3/\text{m}^2\cdot\text{s}$, gas slugs were also observed. With the fine bubbler, only spherical or ellipsoid-shaped bubbles formed. At 0.002 $\text{m}^3/\text{m}^2\cdot\text{s}$, the bubble size was between 0.3 and 4 mm, whereas at 0.008 $\text{m}^3/\text{m}^2\cdot\text{s}$ and 0.026 $\text{m}^3/\text{m}^2\cdot\text{s}$, the bubble sizes were between 1 and 10 mm.

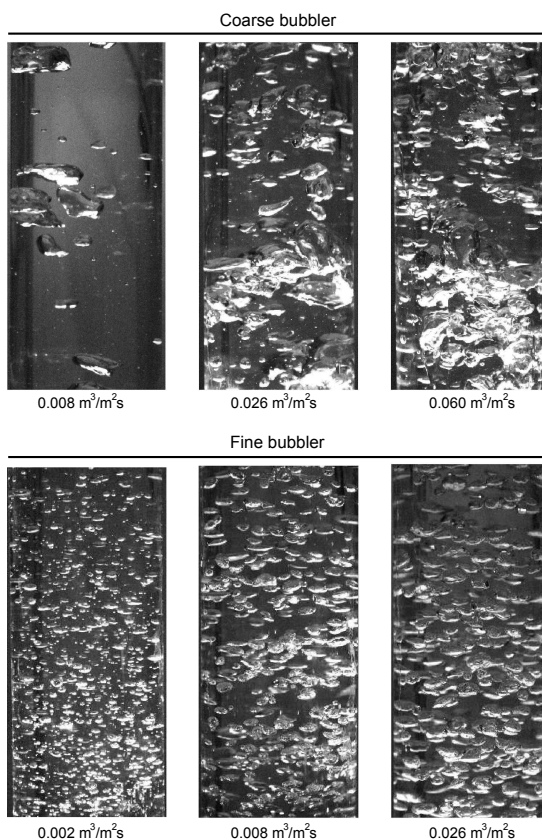


Figure 5.2: Bubbles produced by the coarse and fine bubblers at different rates

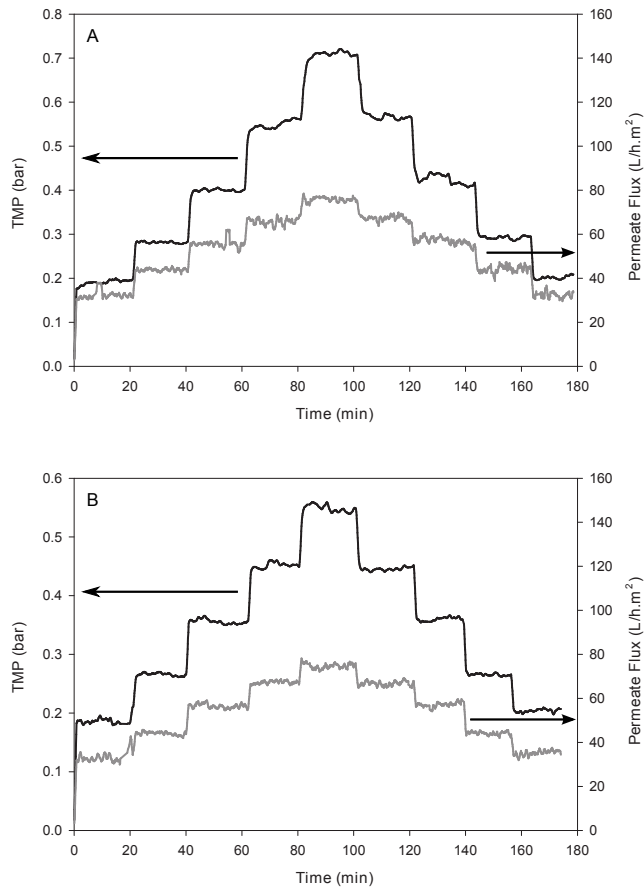


Figure 5.3: Flux-stepping experiments with (a) structured and (b) round fibers with vertical modules, large bubbles and an aeration rate of $0.008 \text{ m}^3/\text{m}^2.\text{s}$ ($0.8 \text{ L}/\text{min}$ air flowrate)

5.3.1 Comparison of round, structured and twisted fibers

Figure 5.3 shows flux-stepping experiments with the structured and round fibers. A vertical module, coarse bubbles and an aeration rate of $0.008 \text{ m}^3/\text{m}^2.\text{s}$ were used. At none of the fluxes, significant cake deposition was observed, which is indicated by a stable TMP at each flux, and equal TMP for a given flux both while stepping up and stepping down. However, the TMPs at each flux deviate from the pure water permeability values, indicating the presence of concentration polarization. This

deviation is plotted for the round, structured and structured-twisted membranes in Figure 5.4. Concentration polarization is highest in the structured fiber, less in the structured-twisted fiber and the lowest in the round fiber. Bubbles prevent polarization and fouling through a number of different mechanisms. The scouring action of the bubbles on the membrane surface and the liquid mixing caused by the secondary flow in the bubble wakes are mechanisms effective in the pathway of the bubbles [8]. Another factor that reduces particle deposition on the membrane is the fiber movement caused by the bubbles [13, 14]. Considering that the looseness of the fibers was similar for all three modules, this factor is not expected to create much difference between the fibers.

The higher concentration polarization on the structured fibers is related to the size of the bubbles in comparison to the size of the convolutions in the structured fibers. Since both the bubbles themselves and the wakes following the bubbles are much larger than the convolutions, the effect of the bubbles cannot reach the depths of the grooves, and leave stagnant areas more susceptible to concentration polarization and subsequent particle deposition. When the structured fibers were twisted, the polarization resistance is less than the structured fibers. In these twisted fibers, the convolutions are not parallel to the bubble trajectory as in the structured fibers. This can provide that more of the area within the grooves is within reach of the rising bubbles.

Figure 5.5(a) shows the polarization resistances calculated using Equation 5.1 for the data in Figure 5.4. In addition to the three modules in Figure 5.4, in a fourth module (twisted-tight), the fibers were fixed more tightly, thus disabling much of the fiber movement cause by the bubbles. It was seen that the polarization resistance in this tight module was significantly higher than those of the loose modules. This supports previous observations showing that the looseness of the fibers is important in preventing fouling [13, 14].

Considering that at a certain flux, the permeate production from the structured fibers is 60% more than the round fibers due to the enhanced surface area, the polarization resistances were also compared for the normalized fluxes, i.e. for equal amount of permeate production per fiber length or equivalently per module volume (Figure 5.5(b)). From this figure it is seen that for the same permeate production, the structured and twisted fiber modules have lower polarization resistances than the round fibers.

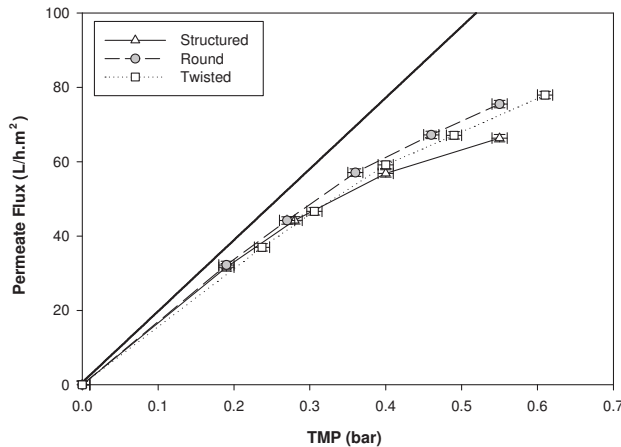


Figure 5.4: Pure water permeability of the membranes and the effect of concentration polarization causing deviation from pure water permeability. Vertical modules, large bubbles. Aeration rate: $0.008 \text{ m}^3/\text{m}^2.\text{s}$

5.3.2 Effect of aeration rate

Figure 5.6 compares the polarization resistance at three aeration rates with coarse bubbles at a normalized flux of 70 L/h.m^2 . When the aeration rate is increased from $0.008 \text{ m}^3/\text{m}^2.\text{s}$ to $0.026 \text{ m}^3/\text{m}^2.\text{s}$, the polarization resistance becomes less for the structured and round fibers, while it is not effected for twisted fibers. Increasing the aeration rate further to $0.060 \text{ m}^3/\text{m}^2.\text{s}$ increases the resistance to higher values than for both of the other two aeration rates. It is often seen that there exists a critical aeration rate below which severe fouling occurs. Above this aeration rate there is little or no improvement in fouling performance [15, 16]. A high shear rate due to extensive aeration can also have detrimental effects, as it increases the shear-induced diffusion and inertial lift forces for the large particles and causes small particles, which can induce severe pore blocking and irreversible gel formation, to become the major foulants. The size of the silica particles used in our experiments are between 10 and 40 nm, which is small and narrow enough to exclude this effect due to increased shear. In our case, the negative effect of high aeration rate is probably due to decreased contact between the feed solution and the membrane because of the over-occupation of the reactor volume with the bubbles. Assuming that the bubbles reach a terminal

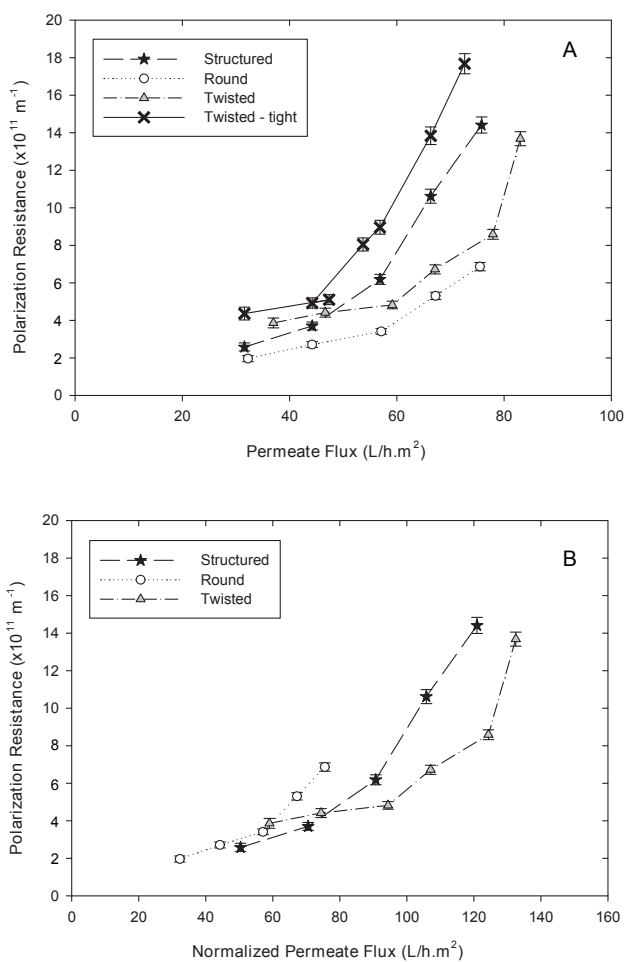


Figure 5.5: Polarization resistance as a function of permeate flux for four different types of membrane modules: Round, structured, twisted and twisted-tight. Vertical modules, large bubbles. Aeration rate: $0.008 \text{ m}^3/\text{m}^2 \cdot \text{s}$ (0.8 L/min air flowrate). (a) Permeate flux is the flux through the actual (convoluted) membrane area for structured fibers. (b) Permeate flux is normalized by using the perimeter of a circle passing through the middle of the fins of the structured fiber, corresponding to a similar effective membrane volume as the round fibers.

velocity of 0.2 m/s [17], the residence time of a bubble in the reactor is estimated as 2 s. Then, with this aeration rate, the bubbles should occupy about 30% of the total reactor volume, which can cause such over-occupation.

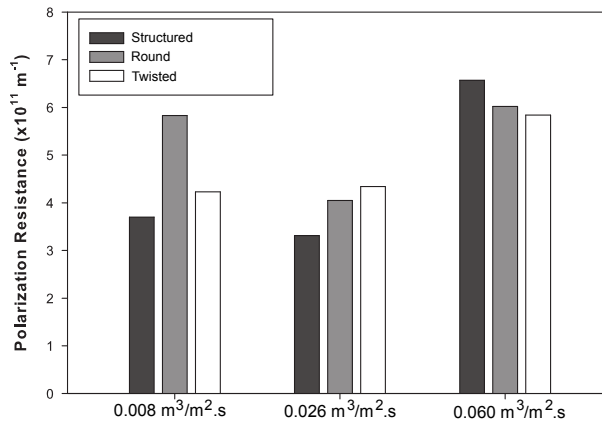


Figure 5.6: Polarization resistance at a normalized permeate flux of 70 L/h.m^2 for round, structured and twisted membrane modules at different aeration intensities. Vertical modules, large bubbles.

5.3.3 Effect of module orientation and bubble size

Figure 5.7 compares vertical and horizontal modules with large and small bubbles for an aeration rate of $0.026 \text{ m}^3/\text{m}^2.\text{s}$. When large bubbles were used, vertical modules performed significantly better than horizontal modules, as also reported by other researchers [18]. In vertical modules, larger bubbles were more effective in depolarizing particle buildup than small bubbles. This higher depolarizing efficiency of large bubbles is attributed to the turbulent wake behind these cap-shaped bubbles and slugs [8].

With small bubbles the behavior was similar in vertical and horizontal modules. In a vertical module, the bubbles can sweep the complete surface of the fibers, whereas when the bubbles move perpendicular to the fiber bundle, dead zones occur at the back of the fiber bundle [18, 19]. Such dead zones are more likely to occur when large bubbles are used, since the size of these bubbles (5-20 mm) is larger than the spacings between individual fibers in the bundle. In this case, the bubbles would preferentially sweep through the periphery of the module and not penetrate through the bundle, leaving the fibers in the inner parts of the bundle as well as the back of the fiber bundle more susceptible to polarization and fouling. For small bubbles (1-10 mm), at

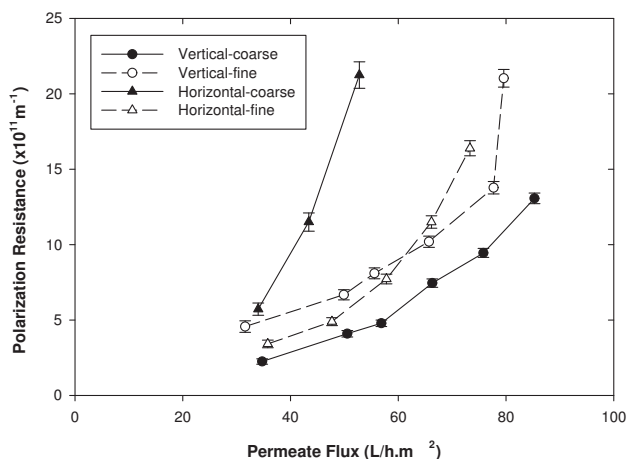


Figure 5.7: Polarization resistance as a function of permeate flux for vertical and horizontal membrane modules, large and small bubbles for the structured membrane. Aeration rate: $0.026 \text{ m}^3/\text{m}^2\cdot\text{s}$.

least part of the bubbles can penetrate between the fiber bundle, causing mixing and preventing polarization in an equivalent manner to vertical modules.

5.3.4 Effect of sub-mm sized bubbles

As shown in Figure 5.2, the bubble size was dependent on both the sparger used and the air flow rate. Using a fine bubbler and a low aeration rate of $0.002 \text{ m}^3/\text{m}^2\cdot\text{s}$, bubbles of sizes close to the size of the corrugations of the structured fibers could be formed. It was observed that the polarization resistances under these conditions were much higher than those for higher aeration rates used with the same bubbler (Figure 5.8). Furthermore, at the highest fluxes indicated for each fiber, cake deposition started to occur, observed as an increasing TMP during the constant flux filtration. Under these conditions, although the size of the bubbles were on the order of the size of the convolutions in the structured fiber, the bubbles did not cause any enhancement in preventing polarization in these fibers. If the bubbles would have been able to reach within the grooves in the structured fibers, we would see at least a comparable resistance in the structured and round fibers. However, the resistance in the structured fibers is much higher than that of the round fiber. Yeo et al. reported that small

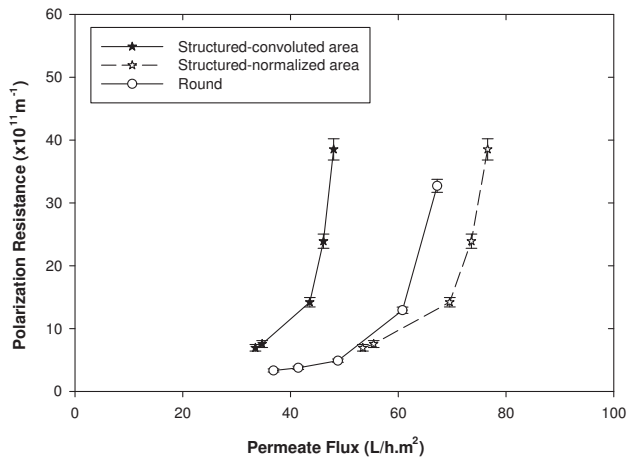


Figure 5.8: Polarization resistance as a function of permeate flux for small bubbles of 0.3-4 mm produced at an aeration rate of $0.002 \text{ m}^3/\text{m}^2\cdot\text{s}$. Vertical modules.

bubbles (0.11 cm^3 which corresponds to about 6 mm diameter in their experiments) seldom moved close to the fibers [14]. In addition to this, it has been shown that in a submerged membrane operation, the secondary flows caused by the bubbles are at least as effective as the scouring action of the bubbles themselves in fouling prevention [5, 8]. Around bubbles smaller than 1 mm, there are no wake structures, and therefore no secondary flows and mixing, but instead there are laminar streamlines, which can only be as effective as liquid cross flow over the membrane.

5.4 Conclusions

The performance of microstructured hollow fiber membranes in a submerged and aerated system was investigated using colloidal silica as a model foulant. The fouling in structured fibers was found to be less than round fibers for the same permeate production per module volume. However, when the fibers were compared at the actual permeate flux through the convoluted area of the structured fibers, the fouling resistance in the structured fibers were higher.

When large bubbles are used, since bubble size was much larger than the convolutions,

the bubbles and secondary flows they create are not able to reach the whole area of the structured fibers. This can create stagnant areas in the grooves, which results in a higher overall resistance. On the other hand, bubbles of sizes similar to the groove dimensions also did not improve the fouling performance in the structured fibers. In general, large, cap-shaped bubbles and slugs were found to be the most effective in fouling removal, as they produce the more turbulent wakes behind them and induce more fiber movement.

Twisting the structured fibers around their axes decreased the fouling resistance, since by twisting, more of the area within the grooves becomes within reach of the bubbles passing by.

Modules in a vertical orientation performed better than horizontal modules when coarse bubbles were used. On the other hand, for small bubbles, vertical and horizontal modules showed similar fouling behavior.

In general, the structured fibers, in their original straight form or as twisted around their own axes, did not cause further enhancement in liquid mixing in the aerated systems. Furthermore, in most of the cases, due to stagnant zones remaining within the grooves, the fouling resistance was higher for these fibers. However, the increase in fouling resistance for the structured and twisted fibers was lower compared to the surface area enhancement due to the microstructured surface. This implies that in submerged, aerated systems structured fibers can still offer enhanced productivity per module volume for the same permeate production compared to round fibers.

5.5 References

- [1] M.A. Shannon, P.W. Bohn, M. Elimelech, J.G. Georgiadis, B.J. Marias and A.M. Mayes; *Science and technology for water purification in the coming decades*; Nature **452** (7185) (2008) 301–310
- [2] T. Buer and J. Cumin; *MBR module design and operation*; Desalination **250** (3) (2010) 1073–1077
- [3] S. Judd; *The status of membrane bioreactor technology*; Trends in Biotechnology **26** (2) (2008) 109–116

- [4] C.-C. Ho and A.L. Zydney; *Overview of fouling phenomena and modeling approaches for membrane bioreactors*; Separation Science and Technology **41** (7) (2006) 1231–1251
- [5] P. Le-Clech, V. Chen and A.G. Fane; *Fouling in membrane bioreactors used in wastewater treatment*; Journal of Membrane Science **284** (1-2) (2006) 17–53
- [6] T. Melin, B. Jefferson, D. Bixio, C. Thoeye, W. De Wilde, J. De Koning, J. van der Graaf and T. Wintgens; *Membrane bioreactor technology for wastewater treatment and reuse*; Desalination **187** (1-3) (2006) 271–282
- [7] F. Meng, S.-R. Chae, A. Drews, M. Kraume, H.-S. Shin and F. Yang; *Recent advances in membrane bioreactors (MBRs): Membrane fouling and membrane material*; Water Research **43** (6) (2009) 1489–1512
- [8] Z.F. Cui, S. Chang and A.G. Fane; *The use of gas bubbling to enhance membrane processes*; Journal of Membrane Science **221** (1-2) (2003) 1–35
- [9] A. Sofia, W.J. Ng and S.L. Ong; *Engineering design approaches for minimum fouling in submerged MBR*; Desalination **160** (1) (2004) 67–74
- [10] P. Bacchin, P. Aimar and R.W. Field; *Critical and sustainable fluxes: Theory, experiments and applications*; Journal of Membrane Science **281** (1-2) (2006) 42–69
- [11] S. Judd; *Submerged membrane bioreactors: Flat plate or hollow fibre?*; Filtration and Separation **39** (5) (2002) 30–31
- [12] P. Çulfaz, E. Rolevink, C.J.M. van Rijn, R.G.H. Lammertink and M. Wessling; *Microstructured hollow fibers for ultrafiltration*; Journal of Membrane Science **347** (1-2) (2009) 32–41
- [13] F. Wicaksana, A.G. Fane and V. Chen; *Fibre movement induced by bubbling using submerged hollow fibre membranes*; Journal of Membrane Science **271** (1-2) (2006) 186–195
- [14] A.P.S. Yeo, A.W.K. Law and A.G. Fane; *The relationship between performance of submerged hollow fibers and bubble-induced phenomena examined by particle image velocimetry*; Journal of Membrane Science **304** (1-2) (2007) 125–137
- [15] N.V. Ndinisa, A.G. Fane and D.E. Wiley; *Fouling control in a submerged flat sheet membrane system: Part I - Bubbling and hydrodynamic effects*; Separation Science and Technology **41** (7) (2006) 1383–1409
- [16] T. Ueda, K. Hata, Y. Kikuoka and O. Seino; *Effects of aeration on suction pressure in a submerged membrane bioreactor*; Water Research **31** (3) (1997)

489–494

- [17] L. Fan and K. Tsuchiya; *Bubble wake dynamics in liquids and liquid-solid suspensions* (1990); Butterworth
- [18] S. Chang, A.G. Fane and S. Vigneswaran; *Experimental assessment of filtration of biomass with transverse and axial fibres*; *Chemical Engineering Journal* **87** (1) (2002) 121–127
- [19] Y. Murai, T. Sasaki, M.-A. Ishikawa and F. Yamamoto; *Bubble-driven convection around cylinders confined in a channel*; *Journal of Fluids Engineering, Transactions of the ASME* **127** (1) (2005) 117–123

CHAPTER 6

Hollow fiber ultrafiltration membranes with microstructured inner skin

THIS CHAPTER HAS BEEN SUBMITTED FOR PUBLICATION:

P.Z. Çulfaz, M. Wessling and R.G.H. Lammertink, *Hollow fiber ultrafiltration membranes with microstructured inner skin*, Journal of Membrane Science

ABSTRACT

Hollow fiber membranes with microstructured inner surfaces were fabricated from a PES/PVP blend using a spinneret with a microstructured needle. The effect of spinning parameters such as polymer dope flow rate, bore liquid flowrate, air gap and take-up speed on the microstructure and shape of the bore and its deformation were investigated. It was found that when a high bore flowrate was used, the microstructure in the bore surface was destroyed. The bores were deformed to an oval shape when the fiber walls were thick. This was attributed to buckling of the fiber shell as a result of the coagulation and shrinkage of the outer surface. Fibers were also fabricated with a round-needled spinneret for comparison. The intrinsic pure water permeabilities (based on the actual bore surface areas) of fibers with structured and round bores were found to be similar. On the other hand, the structured fibers have larger pores in the skin layer. Smaller pores on the round fibers are considered to form when the inner surface coagulates and the skin layer is pulled inwards due to the shrinkage caused by phase separation. When the bore is structured, the wavy shape can dampen this contraction effect resulting in larger pores. The skin layer thickness of the fibers was investigated using a colloidal filtration method. It was shown that fibers with microstructured bores which have mostly uniform skin layer thickness and reasonably narrow pore size distribution can be fabricated.

6.1 Introduction

Channels with microstructured surfaces are interesting for many applications. For asymmetric membranes, microstructuring the skin surface can enhance area-to-volume ratio and increase the productivity of the membrane [1–4]. Furthermore, the microstructure can create secondary flows that improve liquid mixing and therefore reduce concentration polarization [5–9]. Other applications include cell culturing for tissue engineering, where the microstructure or micropattern helps cell attachment and orientation [10–13], and microfluidic channels, where grooves on channel walls can improve mixing [14–16].

In literature there are a number of studies illustrating that introducing corrugations that lie normal to the feed flow direction on flat sheet membranes can promote secondary flows and reduce concentration polarization [7–9, 17, 18]. Although microstructuring flat sheet membranes has been done more often, microstructuring tubular membranes is more rare. Broussous et al. reported the fabrication of ceramic tubular membranes with helical grooves on the inner surface. They observed significant flux improvement compared to tubular membranes with smooth walls and attributed this improved fouling performance to the flow disturbance by the helical structure [5, 6]. Ceramic microfiltration membranes with star-shaped channels are also commercially available [19, 20].

Several researchers reported that when spinning hollow fiber membranes, under some conditions the bore becomes corrugated [21–25]. While this was mostly seen as an undesired irregularity in membrane research, for tissue engineering this phenomenon was exploited to fabricate porous fibers with well-aligned grooves which facilitate cell orientation in scaffolds [10, 11, 13].

Hollow fiber membranes with microstructured surfaces can also be fabricated using microstructured spinnerets. Fabrication of hollow fibers with microstructured outer surfaces has been reported for gas separation and ultrafiltration applications [2, 4]. The spinneret used contains an insert with a microstructured hole in the middle, which transfers its shape to the membrane during phase separation. Nijdam et al. demonstrated that it is also possible to make fibers with microstructures on the bore side by using a spinneret with a microstructured needle made by electroplating on an

outside-structured fiber template.

In this study, we use a spinneret with a microstructured needle fabricated by laser ablation to make hollow fibers with microstructured bore for ultrafiltration applications. The parameters affecting the replication of the microstructure and deformation of the bore shape are investigated. The fibers were characterized with respect to permeability, pore size distribution and skin layer thickness and compared to round hollow fibers with inner skin.

6.2 Experimental

6.2.1 Fiber Fabrication

The fibers were fabricated with the polymer dope 16.6% PES, 4.91% PVP K30, 4.91% PVP K90, 7.18% H₂O, 66.32% NMP. Water at room temperature was used as bore liquid. The external coagulation bath was water at 57±5 °C. The spinning conditions for the fabrication of different fibers are summarized in Table 6.1. The spinneret used for fibers with microstructured bore is shown in Figure 6.1. The needle was fabricated by laser ablation (Ligtmotif, Enschede-Netherlands). The dimensions of the microstructured spinneret and the round-needled spinneret used to spin round-bore fibers is given in Table 6.2.

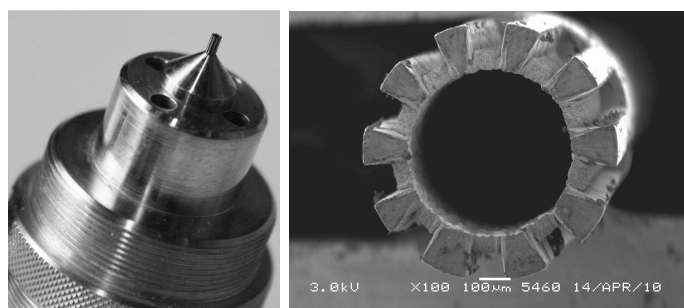


Figure 6.1: The spinneret and the microstructured needle

After spinning, the fibers were washed in water for 24 hours. Then they were placed in 4000 ppm NaOCl solution for 48 hours. After washing in water overnight,

Table 6.1: Fiber spinning parameters

Fiber	Needle	Dope flowrate (mL/min)	Bore flowrate (mL/min)	Take-up speed (m/min)	Air gap (cm)	Residence time in air gap (s)*
SN1	structured	5.35	1.76	4.0	11	1.7
SN2	structured	2.28	1.76	4.0	11	2.3
SN3	structured	2.28	1.76	2.0	11	3.6
SN4	structured	2.28	1.76	4.0	5	1.1
SN5	structured	5.35	1.76	4.0	35	5.2
SN6	structured	5.35	1.76	8.0	35	3.5
SN7	structured	5.35	1.76	8.0	11	1.1
SN8	structured	5.35	2.81	4.0	11	1.6
SN9	structured	2.28	2.81	4.0	11	2.3
RN1	round	2.28	1.76	4.0	11	2.3
RN2	round	2.28	2.81	4.0	35	7.2

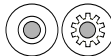
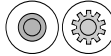

*To calculate the residence time in the air gap, the velocity in the air gap was estimated as the average of the polymer dope velocity exiting the spinneret and the take-up velocity

they were kept in 10% glycerol solution for 24 hours and then dried under ambient atmosphere.

6.2.2 Fiber Characterization

The morphology of the fibers was examined using Scanning Electron Microscopy (JEOL JSM 5600LV). The dimensions of the fibers were measured from the SEM images using ImageJ software.

Table 6.2: Spinneret dimensions

		Microstructured spinneret	Round-bore spinneret
$A_{\text{needle,in}}$ (mm ²)		0.22	0.20
$A_{\text{needle,out}}$ (mm ²)		0.44	0.50
A_{dope} (mm ²)		1.33	1.27

The pure water permeabilities were measured using MilliQ water with 3-fiber modules of 20 cm length and under transmembrane pressure differences of 0.5 and 1.0 bars. Three modules were tested for each fiber batch. The permeabilities reported for the

structured fibers were calculated using the actual convoluted surface area. In other words, the intrinsic permeabilities of the membranes, in units of L/h.m².bar, are reported for both structured and round fibers.

The pore size distribution of the fibers were measured by permoporometry [4]. For skin layer thickness determination the colloidal gold filtration method was used [4]. Colloidal solutions of 20 nm gold particles were purchased from Sigma-Aldrich. Membrane modules of 3 cm² area (corresponding to single-fiber modules of ca. 10 cm) were prepared and 15 mL of 25 ppm gold solution was filtered from the shell side towards the bore under a transmembrane pressure difference of 1.5 bar. After filtration, the membranes were dried overnight in vacuum at 30°C and fractured in liquid nitrogen. No further coating was applied on the cross section of the samples which were examined with the backscattered electron detector in the JEOL JSM 5600LV Scanning Electron Microscope under low vacuum (20-25 Pa).

6.3 Results and Discussion

6.3.1 Fiber morphology

Figure 6.2 shows the outer surface of fiber SN2. The outer surface of this fiber and all the other fibers are highly porous while the inner surfaces have a denser skin.

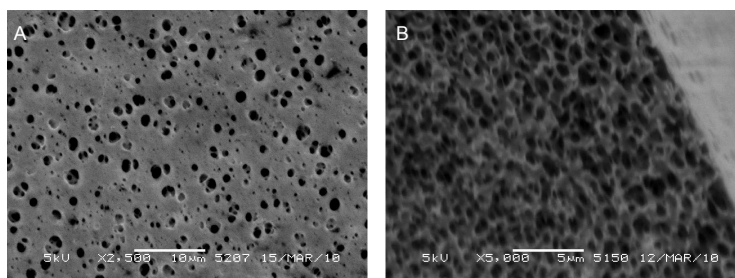


Figure 6.2: The outer surface (a) and cross-section (b) of fiber B

In Table 6.3, the inner perimeter and total cross-sectional area of the fibers with structured and round bores are given. The ratio of these two values, which is equivalent to the membrane area per membrane volume, is shown in the last column. The

structured-bore fiber SN2 has 16% higher membrane area-to-volume ratio than the round fiber RN1. The replication of the needle structure is similar for all structured fibers. Since the other four structured fibers (SN1, 5, 6 and 7) shown in Table 6.3 have thicker walls, and therefore higher volume, the area-to-volume ratios are lower.

Table 6.3: Membrane area per fiber volume for fibers with structured and round bore as an indicator of surface area enhancement

Fiber	Bore perimeter (mm)	Cross-sectional area (mm ²)	Membrane area per fiber volume (m ² /m ³)
SN1	2.90	1.33	2.18
SN2	2.53	0.95	2.67
SN5	2.67	1.34	1.99
SN6	2.60	1.26	2.06
SN7	2.65	1.22	2.18
RN1	2.15	0.93	2.31
RN2	2.09	0.90	2.31

Among the fibers spun with the microstructured spinneret, different bore structures were observed. The fibers SN1, SN5, SN6 and SN7, shown in Figure 6.3 were spun using the same dope and bore flowrates (Table 6.1). The fibers SN1 and SN7 are spun with an 11 cm air gap and take-up speeds of 4.0 and 8.0 m/min, respectively. SN5 was spun with a 35 cm air gap and take-up speed of 4.0 m/min, and SN6 was spun with a 35 cm air gap and take-up speed of 8.0 m/min. In all of these fibers, the microstructure of the bore is retained, however the bore shape is oval. In SN7, the bore is deformed the most and in SN5 the least. The bore of the fiber SN5 was observed to be round after spinning and even after a few hours of washing in water. The oval shape set in after the overnight washing.

On the bore of the fibers, coagulation starts the moment the dope and the bore liquid exit the spinneret. Then, when the fibers enter the water bath, the outer surfaces also coagulate. Although the vapor in the air gap can already initiate phase separation, it is in the water bath that phase separation on the outer surface is complete. When the outer surface coagulates, it is pulled inwards due to the shrinkage after the solvent-nonsolvent exchange [26, 27]. This pulling can deform the shape of the bore if the skin and the fiber shell are soft. A similar explanation was suggested by Bonyadi et al. who investigated the irregularity of fiber bores spun using a standard spinneret with a round needle [21]. They attributed the corrugations or irregularities in the bore

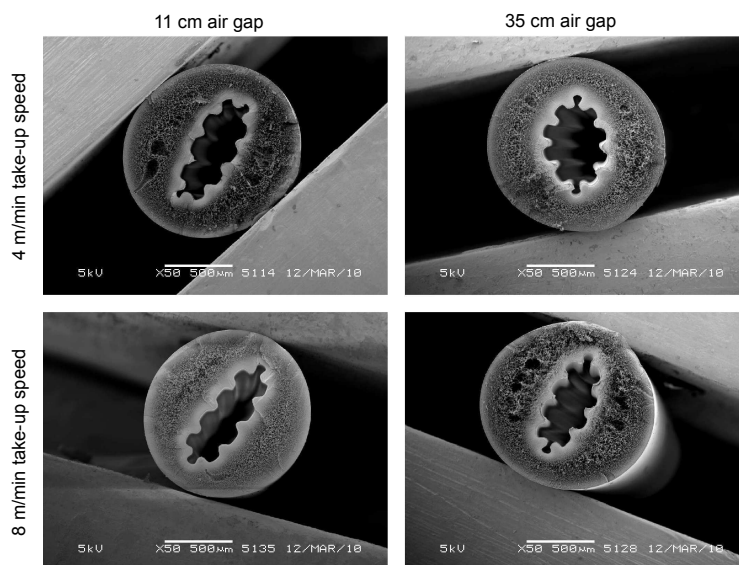


Figure 6.3: Structured fibers SN1, SN5, SN6 and SN7 fabricated using a dope flowrate of 5.35 ml/min, a bore flowrate of 1.76 ml/min with varying take-up speed or air gap.

to buckling of the elastic skin on the inner surface of the fibers. Among these four fibers, SN7 spends the least time in the air gap, and therefore by the time it enters the water bath, the skin formed on the inner surface of the fiber is the softest and the polymer dope constituting the fiber shell is still of relatively low viscosity. There had been little time for nonsolvent liquid induced phase separation from the inside and vapor induced phase separation from the outside. As a result, coagulation of the outer surface of the fiber deforms the bore of this fiber the most. For the fibers that spend more time in the air gap, the skin becomes more rigid, the polymer dope in the shell becomes more viscous and there is less deformation. The least deformation is seen in the fiber SN5, which spends the longest time in the air gap.

The fiber SN2 (Figure 6.4) was spun with a lower dope flowrate than the fiber SN1 (Table 6.1) and the bore of this fiber is round, with the microstructure retained. The wall of the fiber is thinner and therefore by the time the fiber enters the water bath, the part of the shell that has undergone phase separation forms a higher fraction of the total. So when the outer surface coagulates, the shell is more viscous compared to SN1 and does not deform.

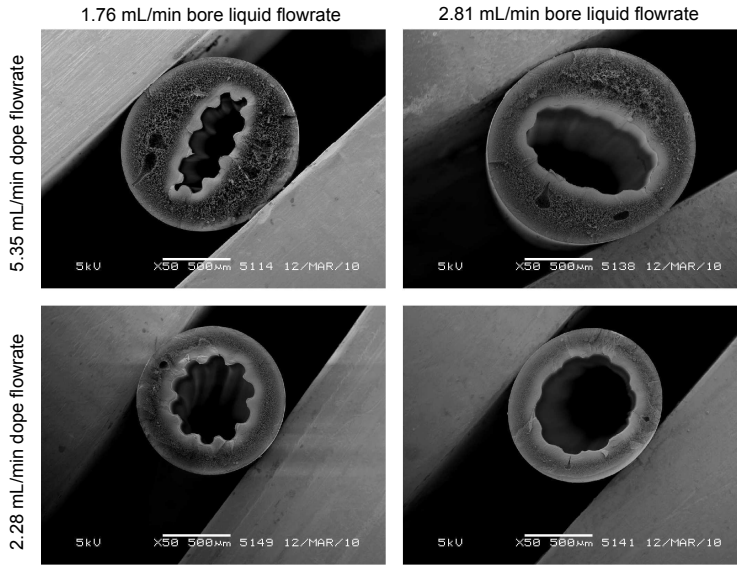


Figure 6.4: Structured fibers SN1, SN2, SN8 and SN9 fabricated using a take-up speed of 4 m/min, air gap of 11 cm and varying dope or bore flowrates

The fibers SN8 and SN9 were spun with a higher bore flowrate than the fibers SN1 and SN2, respectively (Table 6.1, Figure 6.4). The deformation of the bores are similar in SN1-SN8 (oval), and SN2-SN9 (round). However, for the fibers SN8 and SN9 spun with high bore flowrates, the microstructured shape of the bore is destroyed. A higher bore flowrate exerts a higher pressure towards the outer radial direction. This pressure can destroy the structure before the skin can solidify and become rigid.

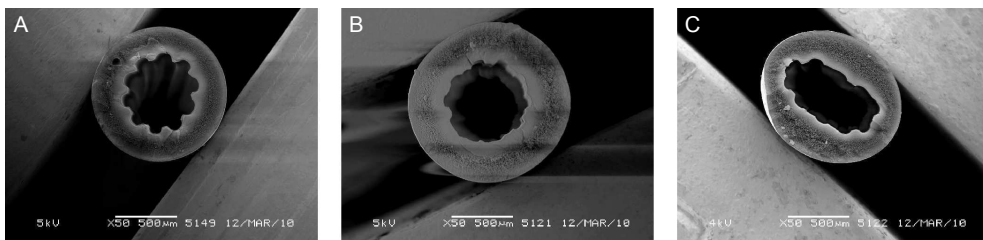


Figure 6.5: Structured fibers SN2, SN3 and SN4 fabricated using a dope flowrate of 2.28 ml/min, a bore flowrate of 1.76 ml/min and (a) 11 cm air gap, 4 m/min take-up speed, (b) 11 cm air gap, 2 m/min take-up speed, (c) 5 cm air gap, 4 m/min take-up speed.

The fiber SN3 (Figure 6.5(b)) was spun using a lower take-up speed than fiber SN2,

with the rest of the spinning parameters the same (Table 6.1). The fiber has a thicker wall and the microstructure in the bore is destroyed although the overall shape is round. With a lower take-up speed there is expected to be more die swell, which can push the bore towards inside and destroy the microstructure [28].

The fiber SN4 (Figure 6.5(c)) was spun using a lower air gap than fiber SN2, while the rest of the spinning parameters were kept the same (Table 6.1). With a short air gap of 5 cm, the skin can be so soft that it is both deformed to an oval shape and its microstructure is destroyed upon the coagulation of the outer surface.

In general, it was observed that a high bore flowrate can destroy the microstructure on the inside surface. Also, when the skin on the inner surface of the fiber has not solidified to a certain extent, or when the fiber shell is still soft, the coagulation of the outer surface can deform the shape of the bore.

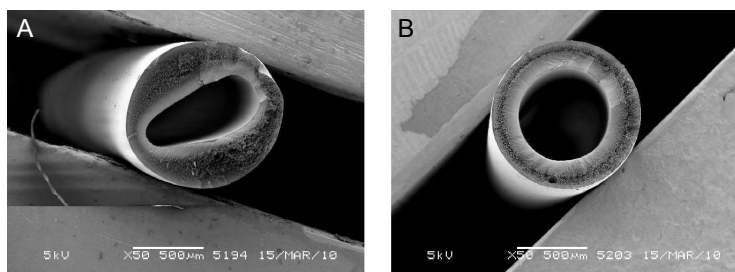


Figure 6.6: The fibers RN1(a) and RN2(b)

The fiber RN1 spun with the round needle with the same spinning parameters as the structured fiber SN2 has a deformed bore (Figure 6.6). This implies that although the spinning conditions are the same, the phase separation process can be different for the fibers spun with the round and structured needle. The fiber RN2, spun using the round needle has a round bore and is used for further comparison with the structured fibers.

6.3.2 Fiber performance

The intrinsic pure water permeability of all the fibers are similar (Figure 6.7). This indicates that the resistance of the skin layers should be comparable, since the skin forms the main contribution to the membrane resistance.

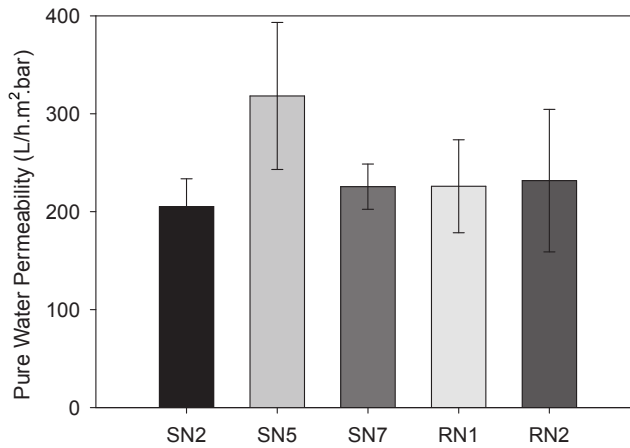


Figure 6.7: Pure water permeability of fibers SN2, SN5, SN7, RN1 and RN2

On the other hand, the mean pore size of the round fibers RN1 and RN2 are both lower than the structured fibers SN2, SN5 and SN7 (Figure 6.8). The broadness of the pore size distributions are mostly similar. The full width at half maximum is $\pm 65\%$ of the mean for all fibers except for SN5, for which it is $\pm 85\%$ of the mean. The difference between the structured and round fibers may be ascribed to the shrinkage of the polymer solution in the bore side upon coagulation. When the polymer dope contacts the bore liquid and the skin is formed, the bore is pulled inwards due to the shrinkage caused by phase-separation [26, 27]. When the bore is round, this pulling force can compress the pores being formed. However for a structured fiber, the wavy shape of the bore can damp the compressing effect of shrinkage.

Table 6.4: Skin layer thickness of the fibers measured with 20 nm gold particles

Fiber	Bottom of groove (μm)	Wall of groove (μm)	Top of fin (μm)	Corner of groove (μm)
SN2	2	2	2	2
SN5	6	-	9	3
SN7	2	2	2	2
RN2	2 μm			

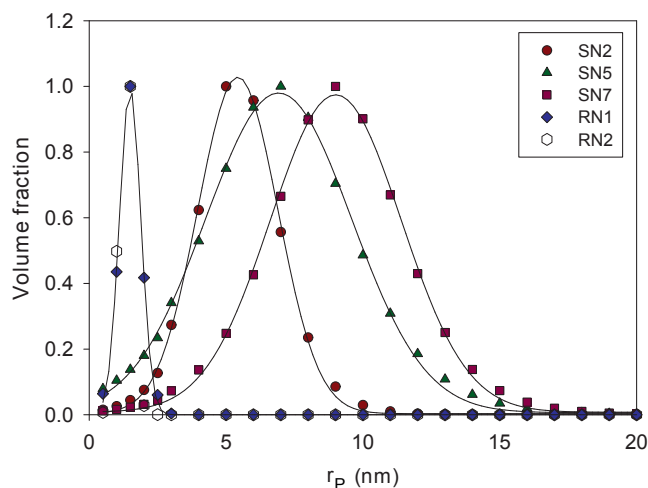


Figure 6.8: Pore size distribution of fibers SN2, SN5, SN7, RN1 and RN2

Table 6.4 summarizes the skin layer thickness measured by the colloidal gold filtration method for a number of structured fibers and the round fiber RN2. Figures 6.9-6.11 show the SEM pictures of the skin layers of the fibers SN2, RN2 and SN5 visualized by 20 nm gold particles.

For the structured fibers SN2 and SN7, the skin layer is 2 μm thick and this thickness is mostly constant throughout the surface. Only on the corner of the fins of SN2, it is locally thicker (Figure 6.9(b)). The round fiber RN2 also has a skin layer of 2 μm (Figure 6.10). On the other hand, for the fiber SN5, the skin is thickest on the top of the fins (9 μm) and gradually gets thinner towards the grooves (6 μm). In the corner

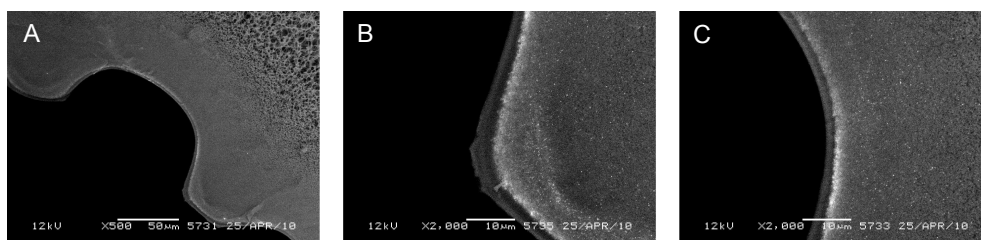


Figure 6.9: Skin layer of fiber SN2: (a) One fin and groove (b) corner of a fin (c) corner of a groove

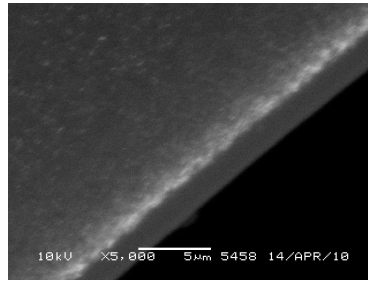


Figure 6.10: Skin layer of fiber RN2

of the grooves there is further thinning of the skin, where it becomes 3 μm (Figure 6.11).

For the structured fibers with deformed bore shapes, the skin thicknesses are similar in all the grooves and fins. This supports the previous discussion that the deformation of the bore towards an oval shape happens due to the coagulation on the outer surface of the fibers, by which time the pore size in the skin should have mostly set in.

The thick skin layer of the fiber SN5 can be attributed to the thicker fiber wall caused by the high polymer dope flowrate used in spinning this fiber. Reuvers et al. who modelled the diffusion processes that occur after the immersion of a polymer solution in a nonsolvent bath predicted that the rate of diffusion in the coagulation bath and in the polymer solution is inversely proportional to the square of the initially cast film thickness [29]. From the moment the polymer solution is brought in contact with the nonsolvent bath until phase separation starts, a top layer with a high polymer concentration forms as a result of the solvent-nonsolvent exchange. With the onset of phase separation, this layer forms the skin of the membrane. For slower diffusion

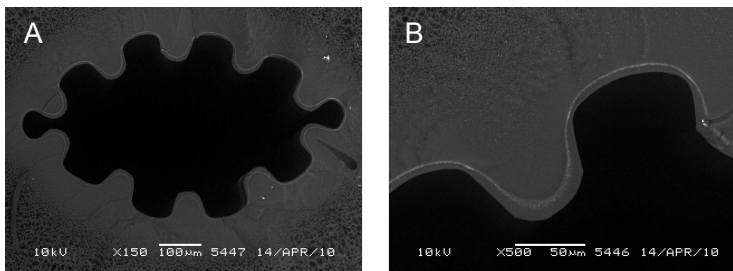


Figure 6.11: Skin layer of fiber SN5: (a) Full bore (b) One fin and groove

of the solvent and nonsolvent, the top layer has more time to grow and therefore is thicker. While this may offer an explanation to the thick skin layer of SN5, the fiber SN7 which has similar wall thickness, has a thinner skin layer. We must note that the skin layer thickness measured by the 20 nm gold colloids only indicates the location of the membrane where the pores are 20 nm in size. Considering that the mean pore diameter of the fiber SN5 is 14 nm and that of SN7 is 18 nm, and that both fibers have pores up to 30 nm in their skin layers (Figure 6.8), the thickness measured from the SEM images should correspond to a location within the skin layer. Looking at the pore size distributions, a higher fraction of the skin layer of fiber SN7 has 20 nm pores compared to SN5, which can be the reason for the thinner “skin” measured with the gold colloids. On the other hand, the variation in the thickness of the “skin” layer, or more correctly the location of 20-nm pores in fiber SN5 is interesting. In Chapter 2, we reported thinning of the skin layer locally in the corner of the grooves or gradual thinning from the fins towards the bottom of the grooves when we used polymer dopes of low coagulation value to fabricate outside-structured fibers. This thinning was attributed to the coagulant being enriched in solvent in the corner of the grooves due to the concave curvature. With the polymer dope used in this chapter, which has 95% coagulation value, the variation in skin thickness was minimized. For outside structured fibers, the coagulation bath has constant composition since it is much larger than the fiber moving through it. For inside-structured fibers, the bore is continuously enriched in solvent until phase separation is complete. For this reason, the coagulation processes can be different for inside and outside-skinned fibers although the same polymer dope and coagulant are used.

6.4 Conclusions

Fabrication of hollow fiber membranes with microstructured inner surfaces using a spinneret with a microstructured needle was reported. Fibers were spun using different polymer dope flow rate, bore liquid flowrate, air gap and take-up speeds. The effect of spinning parameters on the microstructure of the surface, the deformation of the bore and the permeability, pore size distribution and skin layer thickness of the fibers was investigated. It was observed that using a high bore liquid flowrate can destroy the microstructure in the bore. When the skin on the inner surface of the fiber has not

solidified to a certain extent, or when the fiber shell is still soft, the coagulation of the outer surface can deform the shape of the bore. This was attributed to buckling of the fiber shell as a result of the coagulation of the outer surface.

The intrinsic pure water permeabilities of fibers with structured and round bores were found to be similar. On the other hand, the pore size in the skin layer of the structured fibers was larger compared to the round fibers. Smaller pores on the round fibers are considered to form when the inner surface coagulates and the skin layer is pulled inwards due to the shrinkage caused by phase separation. When the bore is structured, the wavy shape can dampen this contraction which may result in larger pores. The skin layer thickness of some of the structured fibers was observed to vary along the surface. This variation follows the same pattern observed with outside-structured fibers spun with low coagulation value polymer dopes. On the other hand, it was also shown that hollow fibers with microstructured bore can be fabricated with a uniform skin layer thickness and reasonably narrow pore size distribution. These fibers enhance the membrane area-to-volume ratio. In addition, as was observed with outside-structured hollow fibers in Chapters 3 and 4, they may offer improved fouling behavior compared to fibers with round bores.

6.5 References

- [1] A.M. Gronda, S. Buechel and E.L. Cussler; *Mass transfer in corrugated membranes*; Journal of Membrane Science **165** (2) (2000) 177–187
- [2] W. Nijdam, J. De Jong, C.J.M. Van Rijn, T. Visser, L. Versteeg, G. Kapantaidakis, G.-H. Koops and M. Wessling; *High performance micro-engineered hollow fiber membranes by smart spinneret design*; Journal of Membrane Science **256** (1-2) (2005) 209–215
- [3] A.M. Peters, R.G.H. Lammertink and M. Wessling; *Comparing flat and micro-patterned surfaces: Gas permeation and tensile stress measurements*; Journal of Membrane Science **320** (1-2) (2008) 173–178
- [4] P.Z. Çulfaz, E. Rolevink, C. van Rijn, R.G.H. Lammertink and M. Wessling; *Microstructured hollow fibers for ultrafiltration*; Journal of Membrane Science **347** (1-2) (2009) 32–41

- [5] L. Broussous, J.c. Ruiz, A. Larbot and L. Cot; *Stamped ceramic porous tubes for tangential filtration*; Separation and Purification Technology **14** (1-3) (1998) 53–57
- [6] L. Broussous, P. Schmitz, H. Boisson, E. Prouzet and A. Larbot; *Hydrodynamic aspects of filtration antifouling by helically corrugated membranes*; Chemical Engineering Science **55** (21) (2000) 5049–5057
- [7] K. Scott, A.J. Mahmood, R.J. Jachuck and B. Hu; *Intensified membrane filtration with corrugated membranes*; Journal of Membrane Science **173** (1) (2000) 1–16
- [8] M.J. van der Waal, S. Stevanovic and I.G. Racz; *Mass transfer in corrugated-plate membrane modules. II. Ultrafiltration experiments*; Journal of Membrane Science **40** (2) (1989) 261–275
- [9] L.-Z. Zhang; *Convective mass transport in cross-corrugated membrane exchangers*; Journal of Membrane Science **260** (1-2) (2005) 75–83
- [10] A. Chwojnowski, C. Wojciechowski, K. Dudzinski and E. Lukowska; *Polysulphone and polyethersulphone hollow fiber membranes with developed inner surface as material for bio-medical applications*; Biocybernetics and Biomedical Engineering **29** (3) (2009) 47–59
- [11] Y. Long, N. Zhang, Y. Huang and X. Wen; *Formation of highly aligned grooves on inner surface of semipermeable hollow fiber membrane for directional axonal outgrowth*; Journal of Manufacturing Science and Engineering, Transactions of the ASME **130** (2) (2008) 0210111–0210118
- [12] B.J. Papenburg, L. Vogelaar, L.A.M. Bolhuis-Versteeg, R.G.H. Lammertink, D. Stamatialis and M. Wessling; *One-step fabrication of porous micropatterned scaffolds to control cell behavior*; Biomaterials **28** (11) (2007) 1998–2009
- [13] N. Zhang, C. Zhang and X. Wen; *Fabrication of semipermeable hollow fiber membranes with highly aligned texture for nerve guidance*; Journal of Biomedical Materials Research - Part A **75** (4) (2005) 941–949
- [14] M. Lopez and M.D. Graham; *Enhancement of mixing and adsorption in microfluidic devices by shear-induced diffusion and topography-induced secondary flow*; Physics of Fluids **20** (5)
- [15] A.D. Stroock, S.K.W. Dertinger, A. Ajdari, I. Mezic, H.A. Stone and G.M. Whitesides; *Chaotic mixer for microchannels*; Science **295** (5555) (2002) 647–651
- [16] A.D. Stroock, S.K. Dertinger, G.M. Whitesides and A. Ajdari; *Patterning flows*

- using grooved surfaces*; Analytical Chemistry **74** (20) (2002) 5306–5312
- [17] J. Balster, M.H. Yildırım, D.F. Stamatialis, R. Ibanez, R.G.H. Lammertink, V. Jordan and M. Wessling; *Morphology and microtopology of cation-exchange polymers and the origin of the overlimiting current*; Journal of Physical Chemistry B **111** (9) (2007) 2152–2165
- [18] N. Tzanetakis, K. Scott, W.M. Taama and R.J.J. Jachuck; *Mass transfer characteristics of corrugated surfaces*; Applied Thermal Engineering **24** (13) (2004) 1865–1875
- [19] T.Y. Chiu and A.E. James; *Critical flux determination of non-circular multi-channel ceramic membranes using TiO₂ suspensions*; Journal of Membrane Science **254** (1-2) (2005) 295–301
- [20] F.J.G. Garcia and T.Y. Chiu; *Economic aspects of critical flux operability in star shaped microfiltration membranes: Influence of some operating conditions*; Journal of Membrane Science **325** (2) (2008) 641–646
- [21] S. Bonyadi, T.S. Chung, W.B. Krantz; *Investigation of corrugation phenomenon in the inner contour of hollow fibers during the non-solvent induced phase-separation process*; Journal of Membrane Science **299** (1-2) (2007) 200–210
- [22] J.P. van't Hoff; *Wet spinning of polyethersulfone gas separation membranes*; Ph.D. thesis; University of Twente (1988)
- [23] S.A. McKelvey, D.T. Clausi and W.J. Koros; *A guide to establishing hollow fiber macroscopic properties for membrane applications*; Journal of Membrane Science **124** (2) (1997) 223–232
- [24] Y.E. Santoso, T.S. Chung, K.Y. Wang and M. Weber; *The investigation of irregular inner skin morphology of hollow fiber membranes at high-speed spinning and the solutions to overcome it*; Journal of Membrane Science **282** (1-2) (2006) 383–392
- [25] L. Shi, R. Wang, Y. Cao, C. Feng, D.T. Liang and J.H. Tay; *Fabrication of poly(vinylidene fluoride-co-hexafluoropropylene) (PVDF-HFP) asymmetric microporous hollow fiber membranes*; Journal of Membrane Science **305** (1-2) (2007) 215–225
- [26] M. Bikel, I.G.M. Pünt, R.G.H. Lammertink and M. Wessling; *Shrinkage effects during polymer phase separation on microfabricated molds*; Journal of Membrane Science **347** (1-2) (2009) 141–149
- [27] A. Stropnik, V. Musil and M. Brumen; *Polymeric membrane formation by*

- wet-phase separation: Turbidity and shrinkage phenomena as evidence for the elementary processes*; *Polymer* **41** (26) (2000) 9227–9237
- [28] A. Ziabicki; *Fundamentals of Fibre Formation* (1976); John Wiley&Sons
- [29] A.J. Reuvers and C.A. Smolders; *Formation of membranes by means of immersion precipitation. Part II. The mechanism of formation of membranes prepared from the system cellulose acetate-acetone-water*; *Journal of Membrane Science* **34** (1) (1987) 67–86

CHAPTER 7

Polymeric microsieves made by phase separation micromolding: Downscaling perforation size by solvent-shrinking and optimizing mold design for easier release

PART OF THIS CHAPTER HAS BEEN PUBLISHED:

M. Bikel, P.Z. Çulfaz, L.A.M. Bolhuis-Versteeg, J. Garduño Pérez, R.G.H. Lammertink and M. Wessling, *Polymeric microsieves via phase separation microfabrication: Process and design optimization*, *Journal of Membrane Science* **347** (1-2) (2009) **347** (1-2) (2009) 93–100.

ABSTRACT

Phase separation micromolding, a versatile technique to make microstructured films, can also be used to make polymeric microsieves. While in lab scale, microsieves can be successfully fabricated, improvement is necessary for practical applications and large scale production. The perforation size needs to be decreased from several microns to below a micron for relevant separations. Here, we show that immersing the fabricated PES-PVP microsieves in pure acetone and NMP-acetone mixtures can decrease the size of the perforations. The shrinkage effect in acetone is mainly attributed to the swelling of PVP and removal of PVP-bound water in acetone, while the effect of NMP addition in acetone is based on the dissolution of both polymers. With a 5 wt.% NMP- 95 wt.% acetone solution, around 70% decrease in pore size could be obtained in two hours with microsieves of 5 and 10 μm starting perforation diameter. However, at these long immersion times and for the NMP concentration used, inhomogeneous shrinkage in different parts of the microsieves was observed. With the same solution, 2 μm perforations could be reduced to 1 μm in 30 minutes without inhomogeneities. The second issue addressed was that peeling of the microsieve from the mold after phase separation is difficult, especially for large areas. To investigate the factors affecting the peeling force, different molds were designed and peeling forces were measured with a custom-made peeling device. It was observed that the distance between pillars in a row being peeled and distance between consequent rows normal to the peeling direction both affect the magnitude of the peeling force. For both, longer distances decreased the peeling force. It was observed that in general low pillar densities favor low peeling forces. The arrangement of pillars was also found to be important. When pillars were arranged in swirling lines, in small circles or in one full circle, the peeling force was almost half of that for the standard square arrangement. This is ascribed to the effect of uninterrupted shrinking lines in the square arrangement pulling the film towards the pillars as opposed to broken shrinking lines in the other arrangements mentioned. It was also observed that when the pillars have noncircular shapes, while the microsieve perforations are round, the peeling forces were lower. This was attributed to the decreased contact between the polymer and the pillars.

7.1 Introduction

Microsieves are microfiltration membranes with straight-through pores of well-defined size, which can provide very specific separation performance and high fluxes. Today, examples of both inorganic and polymeric microsieves exist. Inorganic microsieves are made of silicon-based materials via lithographic techniques. Microsieves with pores larger than 1 μm are fabricated using standard mask lithography, while laser interference lithography is used to form submicron pores [1].

The main drawback of inorganic microsieves is the elaborate and expensive fabrication route. On the other hand, polymeric microsieves can be fabricated at lower costs. Several routes to prepare polymeric microsieves have been reported. One approach is to take an existing polymer film and form pores through it. Track etching is one of these routes, which has also made its way to the commercial fabrication of membranes. The method is based on irradiation of a polymeric material with fragments from the fission of heavy nuclei such as californium or uranium, or with ion beams from accelerators. The irradiation forms tracks in the polymer layer, which are later etched to form the membrane pores [2]. Polymeric nano- and microsieves can also be produced via interference holography [3].

The use of spherical templates to form pores in polymers has been reported by several research groups. Self-standing porous polymer layers with pores in the nano- or micrometer range were produced via different routes. Hydrophobized silica colloids [7], glass beads [4], polystyrene microspheres [6] or water-based sessile drops [5] were used as pore formers and were later removed by etching or dissolving.

Another approach is to deposit a polymer solution on a substrate with pillars, which stick through the solution and form the pores after formation of the polymer film. Yan et al. formed pillar arrays of ZnO and polystyrene on selected substrates and deposited polysulfone or nylon 6/6 solutions which were solidified via solvent evaporation [8]. The pillars were then selectively removed by etching in acid or dissolving in a solvent.

Phase separation microfabrication (PS μ F) is a technique which can be used to fabricate films with various microstructures [9]. First, a polymer solution is cast on a microstructured silicon mold. Subsequent phase separation of the solution on the mold transfers the microstructure of the mold to the phase separated film. In

most cases, the shrinkage of the polymer solution upon phase separation enables the microstructured film to be easily peeled off the mold, which can then be used many times. The molds are fabricated by photolithographic techniques and deep reactive ion etching [10].

Phase separation microfabrication can also be used to make microsieves [9, 11]. A volatile additive is used in the polymer solution, which evaporates before phase separation to ensure that the pillars of the mold perforate the polymer solution. Upon phase separation, the perforations made by the pillars form the pores of the microsieve.

In this chapter two aspects of microsieve fabrication by PS μ F are addressed. In the first part downscaling of the perforation diameter by solvent shrinkage is reported. The perforation size in microsieves is limited by the features of the mold. Shrinkage of the microsieve after fabrication can be used to decrease the perforations to below a micron, which would make the membranes suitable for more applications. Gironés et al. used thermal shrinking to decrease the perforation size of the microsieves. They could reduce 2.5 μm perforations down to 0.5 μm by heating the microsieves above their glass transition temperature. During this thermal treatment, pore collapse caused shrinking of the originally porous film. Here we suggest solvent shrinkage as a simple and less energy-intensive alternative. Immersing the microsieves in acetone and acetone-NMP mixtures causes shrinking in perforation size similar to thermal shrinkage.

In the second part, we investigate the effect of mold design on the ease of microsieve release from the molds after phase separation. While with most of the microstructures fabricated by PS μ F, the phase separated films readily release from the mold, when fabricating microsieves, it is more difficult to peel the microsieves from the molds. Several different molds were designed with different pillar spacings, densities, shapes and arrangements and the peeling forces were measured.

7.2 Experimental

7.2.1 Microsieve preparation

For shrinking experiments, microsieves were made from a solution of 10 wt.% polyether-sulfone (PES, Ultrason 6020), 1 wt.% polyvinylpyrrolidone, PVP K30 (Fluka, $M_w \approx 40$ kDa), 1 wt.% polyvinylpyrrolidone, PVP K90 (Fluka, $M_w \approx 360$ kDa), 39 wt.% acetone (Merck, analytical grade) and 49 wt.% N-methylpyrrolidone (NMP, 99% purity, Acros Organics). For peeling experiments, microsieves were made from a solution of 9 wt.% PES, 3 wt.% PVP K90, 40 wt.% acetone and 48 wt.% NMP.

The microsieves were made by casting the solution on silicon molds using a custom-made casting machine with an adjustable knife height. Casting thickness was varied between 20 and 100 μm until perforation was obtained. After casting, the mold with the cast polymer solution was kept under dry nitrogen flow for 3 minutes. This step ensures that the acetone in the solution evaporates and the thickness of the solution on the mold decreases below the pillar height. The solution on the mold was then exposed to a stream of nitrogen at 40°C saturated with water vapor for 3 minutes. In this step, vapor-induced phase separation takes place, which avoids the formation of macrovoids [12]. This step was followed by coagulation in water. After peeling from the molds, the microsieves were rinsed in water overnight.

7.2.2 Molds

Three different molds were used for the microsieves used in shrinking experiments. The pillars were arranged in a square array. The first mold had pillars of 10 μm diameter and 40 μm height located every 20 μm , center to center. The total area with pillars was a square of 6 cm by 6 cm. The second mold had pillars of 5 μm diameter and 20 μm height located every 10 μm , center to center. The third mold had pillars of 2 μm diameter and 20 μm height located every 10 μm , center to center. In the second and third molds the total area with pillars was a circle of 3-cm diameter. The pillars were placed in square-shaped grids of 450 μm by 450 μm containing about 2000 pillars each. The corridors between the grids were at the same level of the bottom of the pillars.

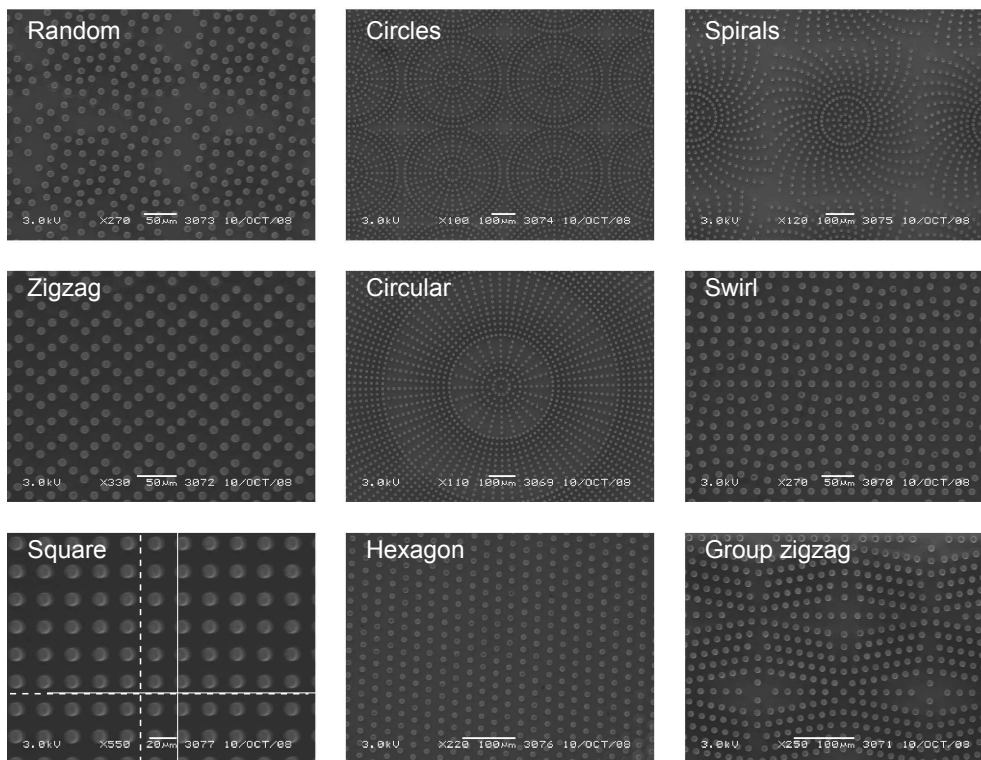


Figure 7.1: Different pillar arrangements used in mold C. Within the square array the shrinkage lines are illustrated.

Four different molds were used while making the microsieves for peeling experiments:

Mold A: 16 fields of round pillars, 10 μm in diameter, 50 μm in height. Pillars were arranged in a rectangular array. In one direction the center-to-center distance between pillars was 20 μm , whereas in the other direction it was varied between 30 to 150 μm .

Mold B: 16 fields of round pillars, 10 μm in diameter, 50 μm in height. Pillars were arranged in a rectangular array. In one direction the center-to-center distances between pillars were 20, 25, 30 and 40 μm . In the other direction the distances were 15, 20, 25 and 30 μm .

Mold C: 9 fields of round pillars, 10 μm in diameter, 40 μm in height. Pillars were

arranged in different arrays, while the pillar density in each field was approximately constant and equal to that in a standard square array with pillars spaced every 20 μm . The SEM images of each of the fields are shown in Figure 7.1.

Mold D: 9 fields of pillars, 10 μm in characteristic length, 40 μm in height. Four of the fields were of round-shaped pillars in a square array with pillar spacing of 50 μm , center to center. Another three had the pillar arrangements “circles”, “circular” and “swirl” as in the mold C, but with pillar spacings of 50 μm instead of 20. The last two fields had pillars with different shapes (cross and hexagon, schematically shown in Figure 7.14).

7.2.3 Microsieve shrinkage

Microsieve shrinkage experiments were done using either pure acetone (Merck, analytical grade), or a solution of 5 wt.% NMP (99% purity, Acros Organics) in acetone. The microsieves were placed between two nonwovens, which were stapled from two sides in order to keep them flat and prevent them from crimpling. Then they were placed in the solutions to shrink for 15, 30, 60 and 120 minutes. After the shrinking they were rinsed overnight in water.

7.2.4 Peeling test

The peeling experiments were done in a custom-made peeling device shown in Figure 7.2. The device is equipped with two stepper motors that move at a set velocity. The vertical motor moves the force sensor (range 0 to 2 N) clamped to the microsieve. The horizontal motor moves the mold with the microsieve on top. By moving the two motors at the same velocity, peeling was done at a constant angle. The force applied during peeling and the positions of the motors was logged on a computer.

7.2.5 Membrane inspection

The microsieves shrunk in solvent and some of the microsieves used in peeling experiments were analyzed by a Scanning Electron Microscope (SEM, Jeol JSM 5600LV). The shrinking in perforation diameter, periodicity and thickness was determined using

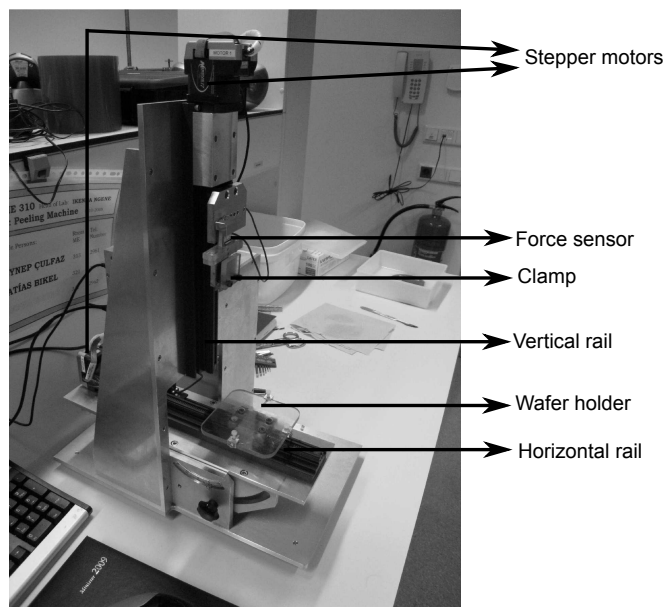


Figure 7.2: The peeling device

ImageJ software. The shrinking in volume was calculated using the periodicity and thickness before and after shrinking.

7.3 Results and Discussion

7.3.1 Downscaling of perforation size by solvent shrinking

Microsieves made with molds of 2, 5 and 10 μm pillars had perforation diameters of 2.1, 5.3 and 11.3 μm , respectively. These microsieves were shrunk in solutions of pure acetone or 5 wt.% NMP in acetone, in order to reduce the perforation diameter. Figure 7.3 shows the surface and cross-section views of the 10 μm microsieve before shrinking (A and E) and after shrinking in acetone for 15 (B and F), 60 (C and G) and 120 minutes (D and H). Both the perforation diameter and thickness decrease upon placing in acetone. The size of the internal pores in the microsieve also decreases. However, the shrinking duration appears to have little effect, as all the microsieves shrunk at different times in acetone have similar internal pore size.

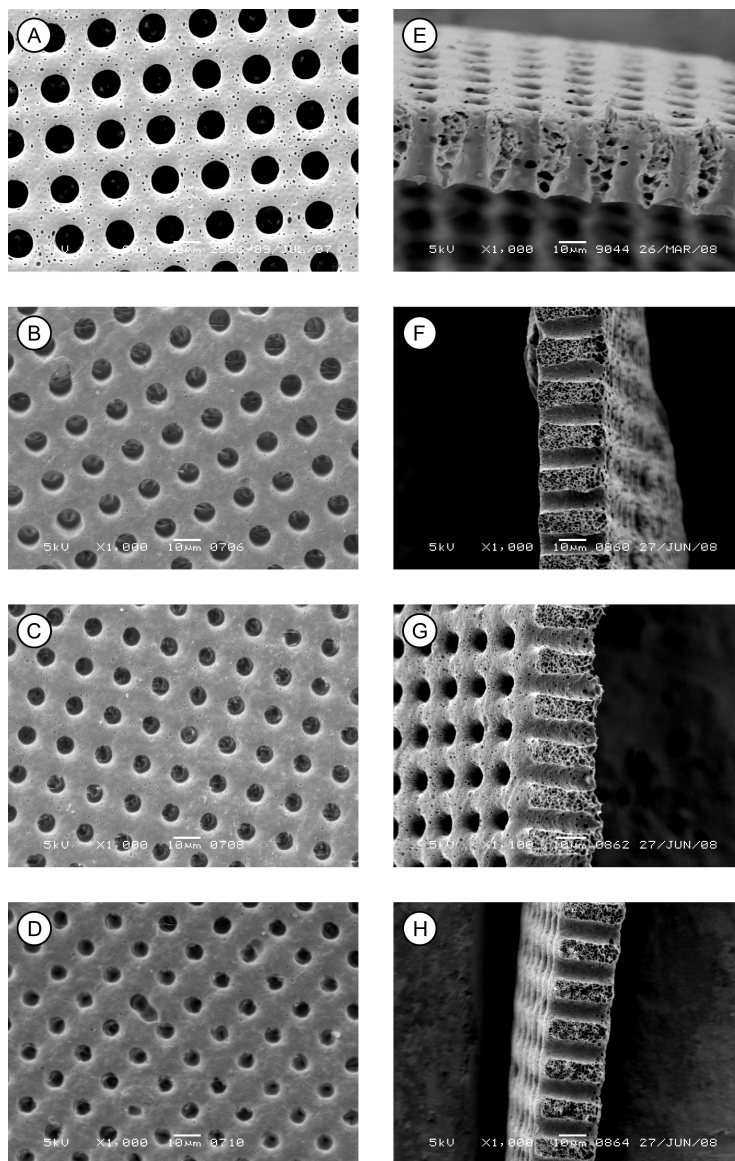


Figure 7.3: The surface and cross-section views of the microsieve with 10 μm perforations before shrinking (A and E) and after shrinking in acetone for 15 (B and F), 60 (C and G) and 120 minutes (D and H)

Figure 7.4 shows the surface and cross-section views of the 10 μm microsieve before shrinking (A and E) and after shrinking in a solution of 5 wt.% NMP in acetone for 15 (B and F), 60 (C and G) and 120 minutes (D and H). The shrinkage in both perforation diameter and thickness is more than with only acetone. The decrease in size of internal pores in the microsieve is also higher and shows a continuous decrease in time. In the microsieves exposed to the 5 wt.% NMP in acetone solution for 120 minutes, inhomogeneous shrinkage was observed. For a few of the microsieves, some inhomogeneities were observed even after 60 minutes. Solutions more concentrated in NMP (up to 10 wt.%) also had the same effect.

Microsieves with starting perforation diameters of 2 and 5 μm were also shrunk in the same solutions. Figure 7.5 shows these microsieves before shrinking (A and D) and after 30 minutes of shrinking in acetone (B and E) and in 5 wt.% NMP-95 wt.% acetone solution (C and F). For these microsieves as well, shrinkage is observed with both solutions. The solution with 5 wt.% NMP decreases the perforation diameter more than only acetone. With 5 wt.% NMP in acetone, the perforation diameter of 2 μm could be reduced to 1 μm .

Figure 7.6 shows the shrinkage in perforation diameter as a function of time for the 5 and 10 μm microsieves shrunk in acetone and in 5 wt.% NMP-95 wt.% acetone solution. Shrinkage in any dimension was defined as,

$$\text{Shrinkage} = \frac{X_{\text{initial}} - X_{\text{final}}}{X_{\text{initial}}} \quad (7.1)$$

For the 2 μm microsieve, shrinkage was only done for 30 minutes and this point is also included in this graph. The degree of shrinking follows a similar pattern for all the microsieves with acetone. After 30 minutes, the shrinkage is more or less constant at about 35-40 %. On the other hand, when 5 wt.% NMP was added to the solution, more shrinking was observed. For the microsieve with 10 μm starting perforation diameter, the shrinkage was slightly less than the other two microsieves. For the 10 μm microsieve, at the end of 2 hours, the shrinkage was 65%, which corresponds to a perforation diameter of 4 μm . For the 5 μm microsieve, the shrinkage at the end of 2 hours was 75% and the resulting perforation diameter was 1.3 μm . For this solution, the perforation diameter appears to decrease continuously. However, due to the inhomogeneous shrinkage observed, no experiments were done at longer times.

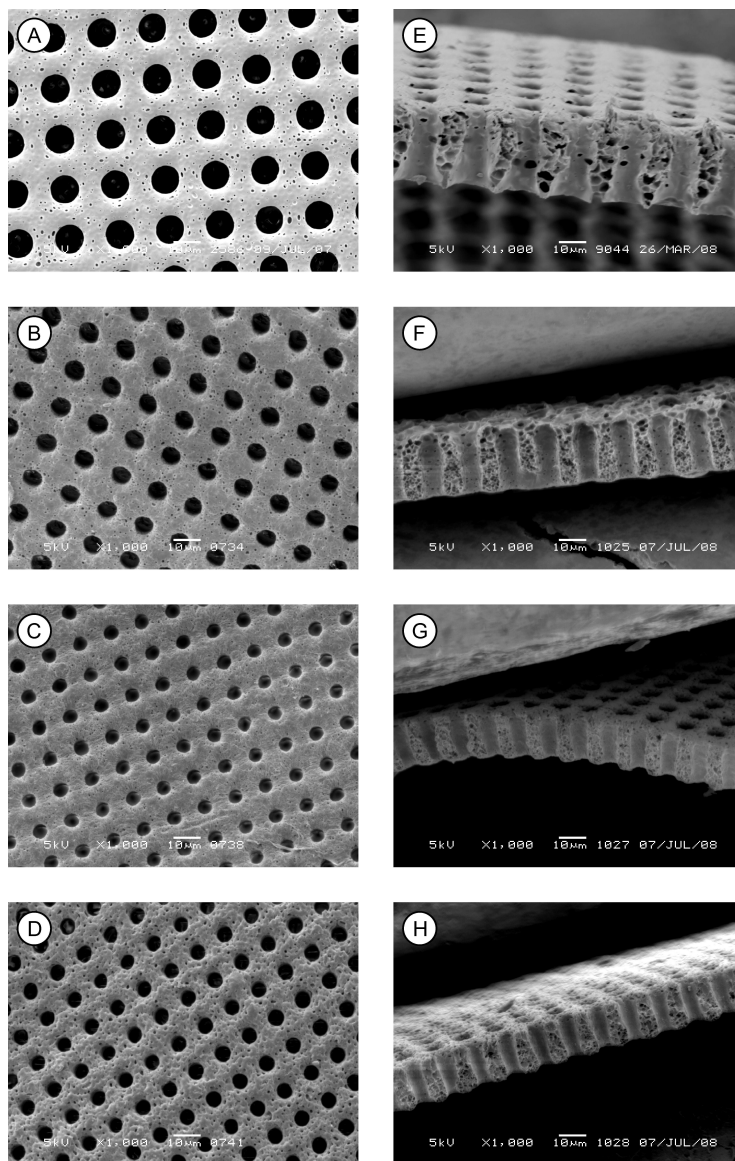


Figure 7.4: The surface and cross-section views of the microsieve with 10 μm perforations before shrinking (A and E) and after shrinking in 5 wt.% NMP-95 wt.% acetone solution for 15 (B and F), 60 (C and G) and 120 minutes (D and H)

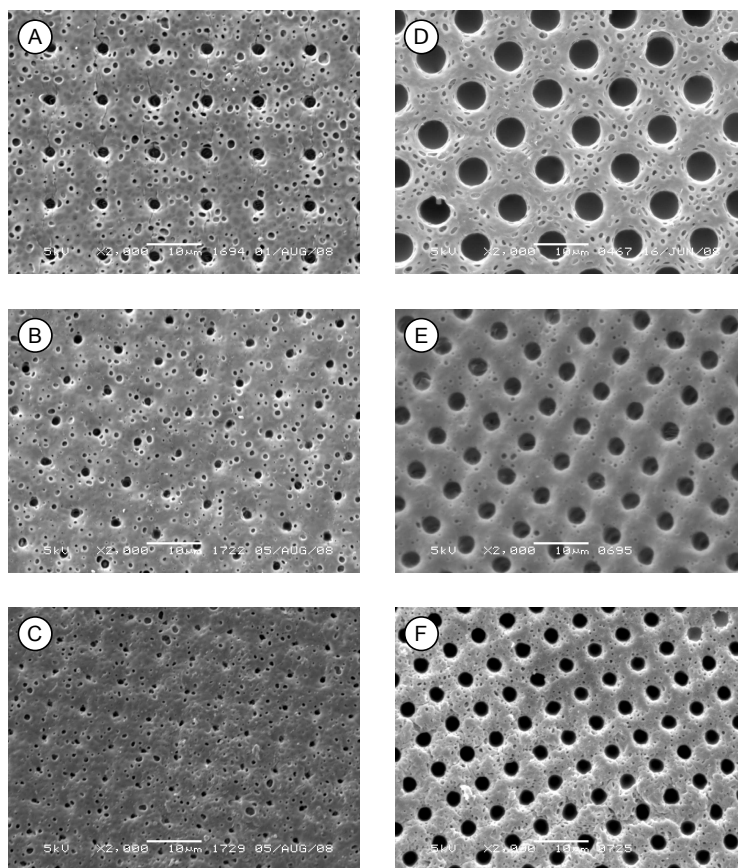


Figure 7.5: The surface views of the microsieves with 2 and 5 μm perforations before shrinking (A and D), after shrinking in acetone for 30 minutes (B and E) and in 5 wt.% NMP-95 wt.% acetone solution for 30 minutes (C and F)

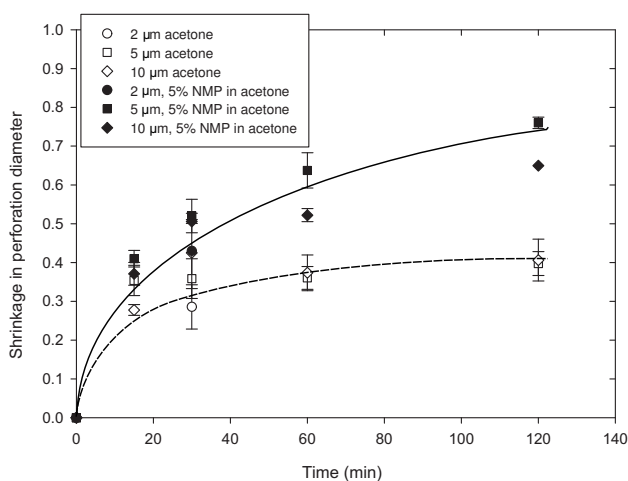


Figure 7.6: Change in the perforation diameter as a function of time for the 2, 5 and 10 μm microsieves immersed in acetone and in 5 wt.% NMP-95 wt.% acetone solution

Figure 7.7 shows the change in perforation diameter, periodicity, thickness and volume as a function of time for the 10 μm microsieve in 5 wt.% NMP-95 wt.% acetone solution. On the whole, the decrease in thickness is the least. The perforation diameter shrinks more than the periodicity and the thickness. At the end of 2 hours, the shrinkage in all dimensions results in about 40% shrinkage in the total volume of the microsieve. The reason for the different degrees of shrinking in different dimensions is because the perforations shrink faster than the internal pores [11]. Plotting the change in periodicity versus the change in perforation diameter (Figure 7.8), we can see more clearly that the shrinkage is not isotropic.

Acetone is only a poor solvent for PVP, whereas NMP is a good solvent for both PES and PVP. When the sieves are immersed in acetone, it will swell the PVP, narrowing the perforations. It was reported in earlier studies with membranes of PES-PVP blends that PVP is present in higher concentrations on the surface [13]. This is due to the hydrophilicity of this polymer, which diffuses towards the polymer-lean phase during phase separation. As the molecular weights of both PVP additives are high, they do not leach out totally and phase separation arrests part of the PVP in the membrane. As it is more abundant in the surface, it is also possible that acetone

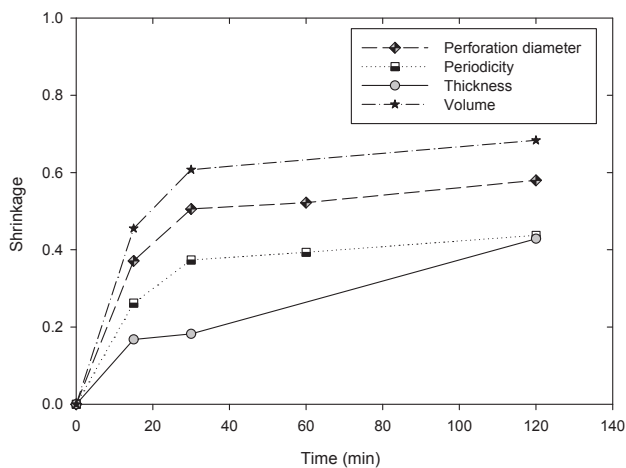


Figure 7.7: Change in the perforation diameter, periodicity, thickness and volume as a function of time for the 10 μm microsieve immersed in 5 wt.% NMP-95 wt.% acetone solution

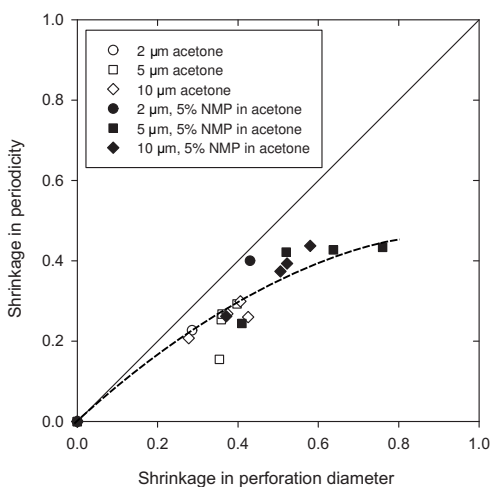


Figure 7.8: The periodicity as a function of perforation diameter (expressed as the ratio of the values after shrinking to the values before shrinking) for the 2, 5 and 10 μm microsieves immersed in acetone and in 5 wt.% NMP-95 wt.% acetone solution. The diagonal represents isotropic shrinkage.

dissolves some of the PVP. Furthermore, Roesink suggested that acetone removes the PVP-bound water in the membrane structure, which can also explain the shrinkage in acetone [14]. Since NMP is a good solvent for both of the polymers, it causes a higher amount of shrinkage by partly dissolving the microsieve and causing pore collapse.

7.3.2 Influence of mold design on release

To peel the microsieves from the molds after phase separation is difficult especially when large pillar areas are used. Often, the sieves do not come off, get torn or break pillars from the mold. Four different mold designs were tried to see their effect on the force needed to peel the microsieves from the molds. More details about this part of the work can be found elsewhere [15, 16].

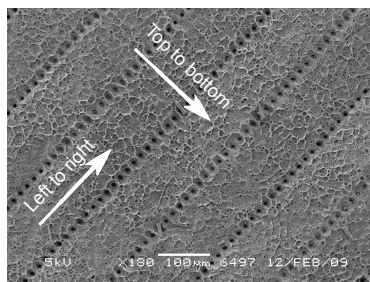


Figure 7.9: Microsieve made using mold A. The figure shows the two peeling directions used.

Microsieves made on mold A, which has constant inter-pillar spacing ($20\ \mu\text{m}$) in one direction and varying spacings ($30\text{--}150\ \mu\text{m}$) in the other direction, were peeled in separate experiments from two directions. These directions are shown in Figure 7.9. Figure 7.10 shows the force needed for each field, for the two peeling directions. It can be seen that in both directions, the peeling force decreases as pillars in one row get further away from each other. In the left-to-right direction, although the sieve is peeled from less pillars at a time, the peeling force is higher than for the top-to-bottom direction for inter-row spacings up to $50\ \mu\text{m}$. To eliminate the effect of peeling different number of pillars in each row, we expressed the peeling forces per pillar in Figure 7.11. It is observed that the peeling force per pillar is still higher in the left-to-right direction than the top-to-bottom direction. This implies that the distance between

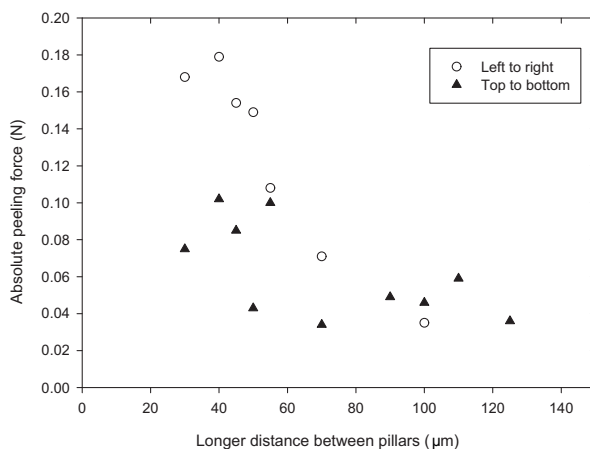


Figure 7.10: Absolute force needed to peel microsieves from mold A. Two different peeling directions showed separately.

consequent rows in the peeling direction has a significant effect. When peeling in the direction where there is 10 μm space between consecutive rows (20 μm spacing from center to center), the peeling force is higher. However the peeling force per pillar decreases with increasing spacing between pillars in each row being peeled.

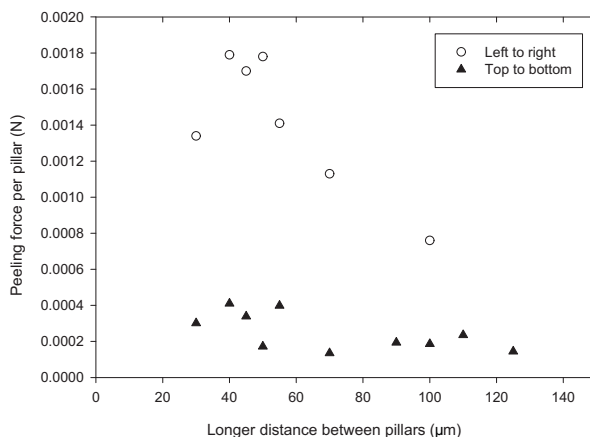


Figure 7.11: Peeling force normalized for the number of pillars in each row peeled at a time for microsieves peeled from mold A.

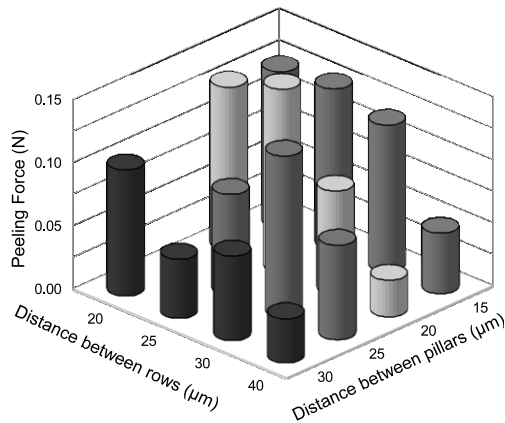


Figure 7.12: Force needed to peel microsieves from fields of different pillar densities on mold B.

Figure 7.12 shows the peeling forces for the 16 different fields on mold B. The graph shows the forces obtained in one peeling direction. In the other direction the trend was the same. With decreasing distance between rows and pillars in one row, the peeling force increases. This is seen in figure 7.12 as increasing forces toward the back corner of the graph, where the pillar density is highest.

Microsieves made with mold C show that the pillar disposition has a noticeable effect on the peeling force. This is considered to be related to the shrinkage accompanying the phase separation of the polymer solution. When the pillars are placed in a regular square array, the shrinkage in the lateral direction pulls the film towards the pillars. As the distance between pillars is the same in all directions, leaving long corridors without pillars causes uninterrupted shrinkage lines (illustrated on the square array in Figure 7.1) as long as the pillar field [16]. With the other pillar arrangements in this mold, the pillars are placed in more “irregular” arrangements, breaking shrinking lines.

The highest peeling forces were observed in the fields where pillars were spaced randomly, in zigzags and in grouped zigzags. For these three fields, the peeling force was higher than for the square array. This may be attributed to the small inter-pillar spacings in some parts of these fields, which make the peeling difficult as observed with mold A. The fields with pillars placed in small circles, in one big circle and in a swirling arrangement required the lowest forces for peeling.

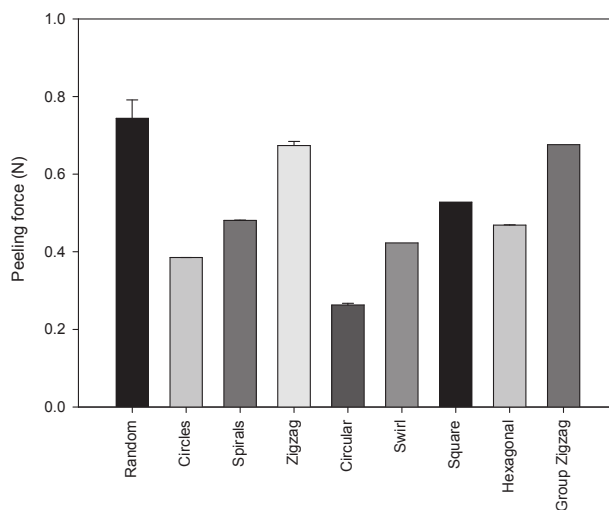


Figure 7.13: Force needed to peel microsieves from fields of different pillar arrangements on mold C.

Figure 7.14 shows the peeling forces for the noncircular shaped pillars, as well as the round pillars in “circles”, “circular” and “swirl” arrangements with 50 μm average pillar spacing. The fields with cross and hexagon pillars needed lower peeling forces. It was observed that in the microsieves made from these molds, the sieves still had round pores. When coagulating, the polymer shrinks slightly away from the pillar, reducing its contact with it. Therefore, for these fields the microsieve has less contact with the pillar during peeling, which can explain the lower peeling forces measured. For the “circles”, “circular” and “swirl” arrangements, the trend observed was the same as what was observed with mold C.

7.4 Conclusions

Phase separation micromolding was used to make microsieves. Two issues that are important for practical applications and large scale production of these microsieves were addressed. The first is the need to decrease the perforation size from several microns to below a micron. It was shown that immersing the fabricated PES/PVP

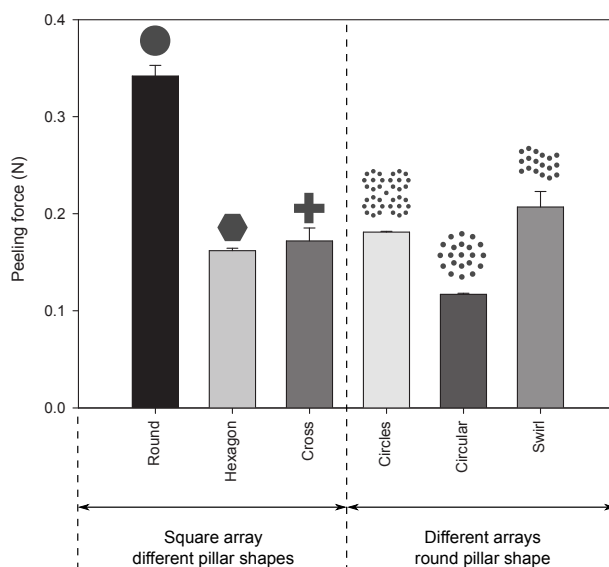


Figure 7.14: Force needed to peel microsieves from mold D, which has three different arrangements of round-shaped pillars as in mold C and fields of cross and hexagon shaped pillars

microsieves in pure acetone and in NMP-acetone mixtures can decrease the size of the perforations. The shrinkage in acetone is mainly attributed to the swelling of PVP and removal of PVP-bound water in acetone, while the effect of NMP addition in acetone is based on the dissolution of both polymers. In two hours, with a 5 wt.% NMP- 95 wt.% acetone solution, around 70 % decrease in pore size could be obtained with microsieves of 5 and 10 μm starting perforation diameter. However, at these long immersion times and for the NMP concentration used, inhomogeneous shrinkage in different parts of the microsieves were observed. Starting from a microsieve with 2 μm perforations, 1 μm perforations could be obtained in 30 minutes without inhomogeneities using the 5 wt.% NMP- 95 wt.% acetone solution. The shrinkage technique is very simple and therefore promising.

Another issue that is important for large scale production of microsieves with phase separation micromolding is that peeling of the microsieve from the mold after phase separation is difficult and often results in partial release, tearing of the film or breaking the pillars of the mold. To investigate the factors affecting peeling forces, different

molds were designed and the peeling forces were measured with a custom-made peeling device. It was observed that the distance between pillars in a row being peeled and distance between consequent rows normal to the peeling direction both affect the magnitude of the peeling force. For both, longer distances decreased the peeling force. It was also observed that lower pillar densities favor low peeling forces.

The arrangement of pillars was found to be important. When pillars were arranged in swirling lines, in small circles or in one full circle, the peeling force was almost half of that for the standard square arrangement. This is ascribed to the effect of uninterrupted shrinking lines in the square arrangement pulling the film towards the pillars as opposed to broken shrinking lines in the other arrangements mentioned. It was also observed that when the pillars have noncircular shapes, while the microsieve perforations are round, the peeling forces were lower. This was attributed to the decreased contact between the microsieve and the pillars.

7.5 References

- [1] S. Kuiper, C.J.M. Van Rijn, W. Nijdam and M. Elwenspoek; *Development and applications of very high flux microfiltration membranes*; Journal of Membrane Science **150** (1) (1998) 1–8
- [2] P. Apel; *Track etching technique in membrane technology*; Radiation Measurements **34** (1-6) (2001) 559–566
- [3] A.M. Prenen, J.C.A.H. Van der Werf, C.W.M. Bastiaansen and D.J. Broer; *Monodisperse, polymeric nano- and microsieves produced with interference holography*; Advanced Materials **21** (17) (2009) 1751–1755
- [4] C. Greiser, S. Ebert and W.A. Goedel; *Using breath figure patterns on structured substrates for the preparation of hierarchically structured microsieves*; Langmuir **24** (3) (2008) 617–620
- [5] S.F. Jahn, L. Engisch, R.R. Baumann, S. Ebert and W.A. Goedel; *Polymer microsieves manufactured by inkjet technology*; Langmuir **25** (1) (2009) 606–610
- [6] J. Li and Y. Zhang; *Porous polymer films with size-tunable surface pores*; Chemistry of Materials **19** (10) (2007) 2581–2584
- [7] H. Xu and W.A. Goedel; *Polymer-silica hybrid monolayers as precursors for ultrathin free-standing porous membranes*; Langmuir **18** (6) (2002) 2363–2367

-
- [8] X. Yan, G. Liu, M. Dickey and C.G. Willson; *Preparation of porous polymer membranes using nano- or micro-pillar arrays as templates*; *Polymer* **45** (25) (2004) 8469–8474
- [9] L. Vogelaar, R.G.H. Lammertink, J.N. Barsema, W. Nijdam, L.A.M. Bolhuis-Versteeg, C.J.M. Van Rijn and M. Wessling; *Phase separation micromolding: A new generic approach for microstructuring various materials*; *Small* **1** (6) (2005) 645–655
- [10] L. Vogelaar, J.N. Barsema, C.J.M. Van Rijn, W. Nijdam and M. Wessling; *Phase Separation Micromolding - PS μ M*; *Advanced Materials* **15** (16) (2003) 1385–1389
- [11] M. Gironés, I.J. Akbarsyah, W. Nijdam, C.J.M. van Rijn, H.V. Jansen, R.G.H. Lammertink and M. Wessling; *Polymeric microsieves produced by phase separation micromolding*; *Journal of Membrane Science* **283** (1-2) (2006) 411–424
- [12] L. Vogelaar; *Phase Separation Micromolding*; Ph.D. thesis; University of Twente (2005)
- [13] I.M. Wienk; *Ultrafiltration membranes from a polymer blend: Hollow fiber preparation and characterization*; Ph.D. thesis; University of Twente (1993)
- [14] H.D.W. Roesink; *Microfiltration: Membrane development and module design*; Ph.D. thesis; University of Twente (1989)
- [15] M. Bikel; *Fundamental aspects of Phase Separation Microfabrication*; Ph.D. thesis; University of Twente (2009)
- [16] M. Bikel, P. Çulfaz, L.A.M. Bolhuis-Versteeg, J. Garduño Pérez, R.G.H. Lammertink and M. Wessling; *Polymeric microsieves via phase separation microfabrication: Process and design optimization*; *Journal of Membrane Science* **347** (1-2) (2009) 93–100

CHAPTER 8

Summary and Outlook

8.1 Prologue

Microstructured surfaces are ubiquitous in nature. The *villi* in the walls of mammalian small intestines increases the surface area for absorption of nutrients [1]. The lotus (*Nelumbo nucifera*) leaf owes its self-cleaning effect to the microscopic bumps on its low-energy surface [2]. While nature takes its time in evolving these structures, it has always inspired people in evolving technology. With such inspirations, this thesis focuses on the effect of microstructured surfaces on membranes.

8.2 Summary

In **Chapter 2**, the fabrication of hollow fiber membranes with a microstructured outer surface is described. Microstructured fibers with up to 90% higher surface area per volume could be fabricated. The intrinsic permeability and pore size distribution of these membranes were found to be similar to round hollow fibers spun under the same conditions. As the skin of these asymmetric membranes were on the outer surface, a higher surface area of the skin with the same separation properties implies that the productivity per membrane (or module) volume can be increased by almost twofold. The skin layers of the membranes were further inspected locally using a colloidal filtration method with gold particles. It was seen that the skin layer thickness of the structured fibers can show variations throughout the surface. This variation was attributed to the confinement of the coagulation medium in the grooves resulting in increased solvent concentrations as the solvent-nonsolvent exchange takes place. The variation was suppressed by using a polymer solution very close to the cloud point. Rapid coagulation is considered to form the skin before local concentration gradients can form around the membrane surface.

In **Chapter 3** these microstructured membranes were tested in dead-end filtrations. NMR imaging was used to visualize silica deposition on the membranes. It was observed that the two different silica sols used showed different deposition patterns. The silica sol with smaller particles which was dispersed in a deionized solution (Ludox-TMA) deposited inhomogeneously on the structured fiber surface, with a more compact deposit within the grooves and a much looser and thinner deposit on

the fins. The sol with larger particles in alkaline solution (Bindzil-9950) deposited homogeneously. The difference between the behavior of the two sols was explained by the concentration profiles forming on the membrane surface with the onset of filtration. The concentration profiles in the polarized layer that forms prior to coagulation and cake deposition on the membrane surface were obtained by solving the material balance equation for the particles, which consists of the convective drag towards the membrane, the back diffusion and accumulation. While the concentration polarization layers of both of the sols had high thicknesses on the order of the fiber convolutions, the concentration polarization layer of the Bindzil 9950 sol was found to be more concentrated throughout its whole thickness, while that of the Ludox-TMA sol was much more dilute. The resistance of the polarization layers estimated from the volume fractions using Kozeny-Carman equation revealed that the polarization layer of the Bindzil-9950 sol had a resistance similar to the intrinsic membrane resistance. On the other hand, the resistance of the Ludox-TMA polarization layer was about two orders of magnitude lower. The high resistance of the polarization layer during the Bindzil sol filtration is considered to lead to flow regulation towards equalizing the resistance along the fiber surface. On the other hand, the Ludox particles were trapped at the bottom of the grooves as a result of reduced back diffusion. In filtrations of a sodium alginate solution, the fouling on the structured fibers was observed to be more reversible. This was attributed to the formation of a looser deposit within the grooves, which is more easily removed than a compressed deposit on the round fibers.

In **Chapter 4**, the microstructured fibers were tested in cross-flow filtrations and their performance was compared to round fibers. Additionally, in separate modules, the structured fibers were twisted around their own axes to see the effect of helical grooves under cross-flow. The critical fluxes for the onset of particle deposition and for the onset of irreversible deposition were determined in flux-cycling experiments using colloidal silica and yeast suspensions as feed solutions. The difference between the three fibers was more pronounced during yeast filtrations, which was attributed to the stronger correlation of diffusion of micron-sized particles to shear. Structured fibers showed lower critical fluxes for both particle deposition and irreversibility, while twisted fibers performed either similar to round fibers or better. The improved performance of the twisted fibers was attributed to secondary flows caused by the twisting of the membrane surface with respect to the cross-flow direction. The deposition of

yeast particles on the membrane surface was also observed using a camera. On the structured and twisted fibers less deposition was observed on the fins. This was ascribed to the diffusion of the particles from high shear areas (fins) towards low shear areas (grooves). Furthermore, on the fins of the twisted fibers much less deposition was observed, which supports the argument for secondary flow formation around the twisted structure.

In **Chapter 5**, the structured, round and twisted fibers were compared in submerged filtrations of colloidal silica with aeration. It was found that both structured and twisted fibers had higher resistance to filtration. Twisting improved fouling performance in these systems as well. The higher resistances were attributed to the size of the bubbles being larger than the sizes of the fins and grooves on these fibers. Since the bubbles are larger, they cannot reach the grooves, leaving stagnant areas with a higher degree of polarization. The use of small bubbles close to the size of the features on the structured and twisted fibers did not cause any enhancement, as with small bubbles no turbulence is created in the liquid. Although the structure resulted to be a disadvantage in constant flux, submerged and aerated filtrations, it was shown that the enhancement in surface area of the structured fibers compensates for the increase in resistance and when compared on the flow per fiber length (or equivalently per module volume) basis, the productivity can still be enhanced by using microstructured fibers.

In **Chapter 6**, the fabrication of hollow fibers with microstructured surface on the bore side is described. It was shown that although a strong coagulant (pure water) initiates phase separation immediately on the bore, the replication of the microstructure was not granted. Deformation of the bore towards an oval or slit shape was observed in some of the fibers. This deformation was attributed to the thick walls of these fibers, leaving a soft fiber shell at the moment of phase separation of the outer surface and the resultant buckling of the fiber shell. It was also shown that a high bore liquid flowrate can destroy the microstructure in the bore. The permeability of structured and round fibers was found to be similar, however the pore size distribution and thickness of the skin layer showed differences between different fibers.

In **Chapter 7**, two aspects of polymeric microsieve fabrication by phase separation microfabrication is covered. The immersion of PES/PVP microsieves in acetone and mixtures of acetone and NMP was shown to decrease the pore size by slowly dissolving the polymer matrix and collapsing the pores. The effect of mold design on the ease

of microsieve release after phase separation was described in the second part of this chapter. The distance between pillars in the direction parallel and normal to the peeling direction was observed to affect the force needed for peeling. Longer inter-pillar distances and lower pillar densities decreased peeling forces. The arrangement of the pillars also affected the ease of release. When the pillars were arranged in circles or in swirling curves, the peeling forces were found to be about half of that for the standard square array. Pillars with cross and hexagon shapes also helped easier release when the microsieve pores were round. This was ascribed to the decreased contact between the pillars and the microsieve.

8.3 Reflections

8.3.1 Fabrication of microstructured hollow fibers

Microstructuring hollow fibers is shown to enhance the membrane area-to-volume ratio up to almost two-fold, which can increase permeate production per module and decrease module volumes. The exact shape of the fiber structure is determined by the insert used while spinning and the spinning conditions. In **Chapter 2**, a simple

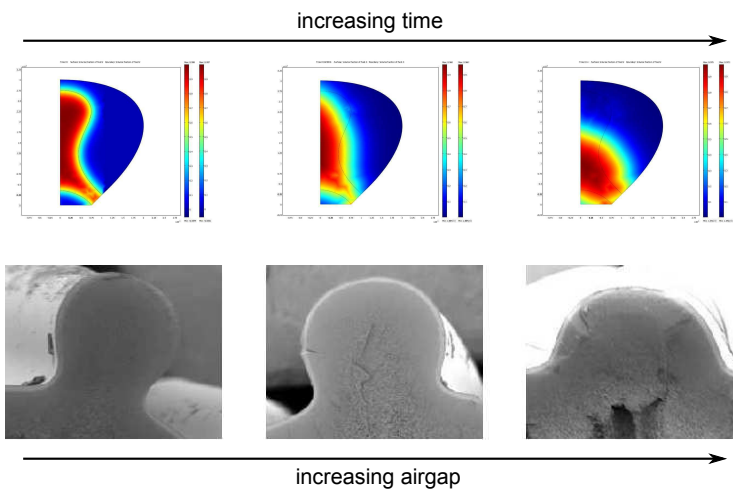


Figure 8.1: Results of the simulation of structure evolution in time and the SEM images of the structure of the fibers spun using increasing air gaps

scaling relation was suggested to describe the structure evolution of the polymer solution in the air gap upon exiting the spinneret. A more detailed model of the process supported by experiments using different inserts and spinning conditions can help in further enhancing the surface area enhancement in these fibers. In preliminary modelling attempts with a finite element modelling software (COMSOL), using the level set method for simulating a moving surface, we obtained quite good agreement between the model and the actual shape evolution of the fiber at different air gaps (Figure 8.1) [3].

Surface area enhancement is not the only important factor for the filtration performance of structured fibers. Although the permeability of the membrane is important, the fouling behavior during the filtration of an actual feed solution is what ultimately matters. In this respect, aiming at a certain filtration system, the structure on the membrane can be optimized for both maximum surface area enhancement and minimum concentration polarization and fouling. For cross-flow filtrations, the shape and depth of the grooves can affect liquid mixing especially when the fibers are twisted.

Twisting is shown to improve the performance of the structured fibers in cross-flow and aerated filtrations. The twisting in the experiments described in this thesis was done after fiber fabrication, during module preparation. It was experienced that the fibers were more elastic right after fabrication before the NaOCl treatment, which removes part of the PVP in the membrane [4]. The elasticity of the as-spun fibers can be used to twist the fibers in the spinning line (e.g. after the pulling wheel) or after collection but before the hypochlorite treatment. More twists would increase the intensity of secondary flows and vortices.

It was observed that the fabrication of the fibers with microstructured bores is more complicated than the fabrication of fibers with microstructure on the outside. Part of this complication is considered to occur during the coagulation of the outer surface in the water bath and can be reduced to some extent by using a triple spinneret. Using a solution with high solvent concentration as the external coagulant can prevent bore deformation. Although some explanations are offered for the larger pore size and varying skin layer thickness of the inside-structured fibers in **Chapter 6**, this phenomena could not be fully explained as it is probably a function of multiple variables of spinning. By spinning with a triple spinneret and a weak external coagulant, these

variables can be reduced and the factors affecting the structure and properties of these fibers can be understood better.

In this study, hollow fibers were fabricated with microstructures on the inside and on the outside. It is also possible to combine these two modifications in one spinneret and make hollow fibers with microstructures on both sides. While this is not very meaningful for asymmetric membranes as the ones in this study, it can have advantages for symmetric fibers such as those for microfiltration, for membrane contactors and for processes where concentration polarization is significant on the permeate side as well as the feed side.

For submerged filtrations with aeration, we concluded that the small size of the microstructures on the fibers excludes the effect of the bubbles and secondary flows caused by the bubbles from the depth of the grooves. Fibers with larger features may still offer advantages in these systems.

8.3.2 Characterization of fouling behavior

Two *in-situ* observation techniques were applied in this study. NMR imaging was used during dead-end filtrations, and direct visual observation was used in cross-flow filtrations. From direct visual observation experiments, we concluded that twisting the fibers may induce secondary flows. NMR imaging can be used to observe flow profiles as well as particle deposition patterns in cross-flow filtrations [5]. This would give very important insight into the filtration behavior of structured and twisted hollow fibers in cross-flow filtrations.

In dead-end filtrations, better fouling reversibility was observed during the filtration of sodium alginate, which is a mixture of molecules with a broad size distribution. The better reversibility was attributed to a looser deposit in the grooves, which forms due to self regulation of the flow towards equalizing the resistance in the fins and grooves of the fibers. It can also be expected that this flow regulation may cause the deposit to be less stratified. On the round fibers, it is expected that the deposit is richer in large molecules close to the membrane and small molecules close to the bulk. This is due to the high diffusivity of the small molecules and low diffusivity of the large molecules. However, on the structured fibers this may not be the case. While this is yet a bit speculative, it may be possible to visualize the deposition

patterns of alginates, proteins or particles on the surface of these membranes using confocal laser scanning microscopy (CLSM). Different size fractions can be labelled with different dyes and by focusing on different planes the presence or absence of stratification of the deposits may be visualized. During the course of this thesis, we tried using fluorescence microscopy and CLSM to observe the deposition of fluorescent proteins, quantum dots and fluorescently labelled dextrans from the cross-section of the fibers. For this purpose, special modules were built using a commercially available transparent epoxy (Bison Kombi-Snel). Fibers were fractured in liquid nitrogen and briefly polished while still cold in order to obtain as flat a surface as possible. The epoxy was spread on a microscope slide cover slip by spin coating. The fiber was glued to the thin epoxy layer and a small module was built around the glued fiber. Leak-free modules could be prepared and filtration of quantum dots was carried out while observing the fiber cross section from below the transparent epoxy with the CLSM. The particle deposition could not be observed online, but when the fibers were broken in liquid nitrogen after filtration and glued on the epoxy-coated cover slip for CLSM examination, a thin deposit layer could be observed (Figure 8.2). The reason

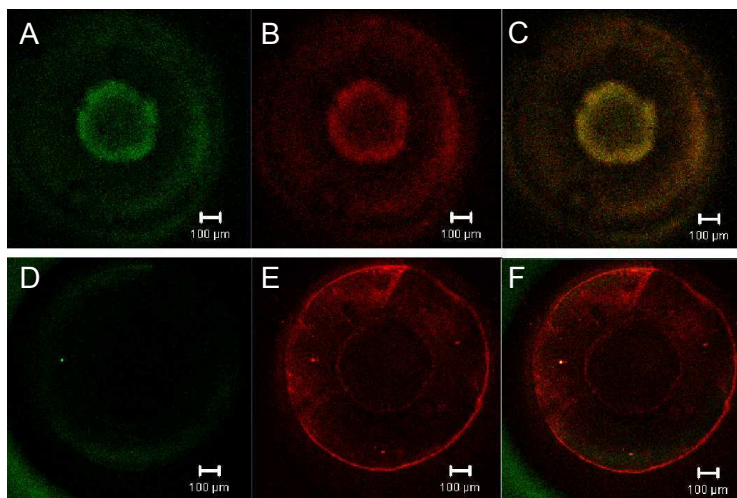


Figure 8.2: The CLSM images from the fiber before filtration (A-C) and after filtration (D-F). Images A and D show the emission of green, B and E of red and C and F of all wavelengths. Notice that the fiber itself also has a background emission. In E and F, the stronger red emission on the periphery of the fiber originates from the quantum dot deposit.

why this deposit could not be observed during filtration is probably because during the preparation of the module, the epoxy creeps up the fiber surface and blocks the pores in a region close to the transparent surface of the module which we examined. If the modules can be made in a way that this does not occur, these modules can be used to observe images of particle deposition from the cross section of the hollow fibers in dead-end filtrations.

8.3.3 Fouling of the microstructured fibers with more complex feed solutions

In this study, feed solutions of colloidal silica, sodium alginate and yeast were used for observing the fouling behavior of the microstructured fibers. It was observed for all feeds that significant differences between round and structured (or twisted) fibers can occur. In real life, hardly any feed solution is as simple as the ones used in these experiments. Often there are multiple components and ions in solution, which change surface interactions between particles. In filtrations of sodium alginate and humic acids, the presence of calcium ions has a significant affect on the fouling behavior [6, 7]. In the presence of silica and protein deposits on the membrane, it has been observed that the rejection of molecules are different than their pure component rejections [8]. In membrane bioreactors, the feed is a complex mixture of microbial flocs, organic matter and inorganic colloids. While shear induced by aeration increases the back diffusion of large flocs in the feed, this may lead to more severe fouling by fine materials [9]. Most of the time, the phenomena which take place in mixed feed solutions cannot be anticipated by superimposing the fouling behavior of single component feeds. Following up on the results from this study, filtrations of feed solutions with ionic components, bidisperse and multidisperse feeds can yield interesting and perhaps promising results in favor of the structured hollow fibers.

In our experiments we used membrane modules with single or a few fibers, unlike real modules, where the packing density is much higher. The fouling behavior of hollow fibers is affected by the packing density and uniformity. Even at low Reynolds numbers, deviations from axial streamlines and inter-fiber flow is often observed [10, 11]. In addition to the flow profile, different shear rates can cause large particles to move from high shear areas to low shear areas, as was discussed in **Chapter 4**. With the

structured fibers, these effects will probably be different than for round fibers. In a module densely packed with twisted fibers, the inter-fiber spacing will constantly expand and contract, as the fibers are not radially symmetric due to the twist. This can further improve liquid mixing and promote secondary flows.

The fibers with microstructured bore are expected to have similar fouling behavior as those with microstructures on the outside. Twisting the fibers around their own axes can decrease fouling in these fibers as well. Twisting multiple fibers in bundles is a way of creating Dean vortices in the bore of the fibers, for both round and structured bores. Combining structured walls with a helically twisting tube can amplify the centrifugal instabilities.

In both dead-end and cross-flow filtrations with the microstructured fibers, sequential particle deposition (i.e. first in the grooves, which later spreads towards the fins) was observed. As the resistance increased in the grooves, more permeate started to flow through lower-resistance areas, thus equalizing the resistances throughout the cross-section. In dead-end filtrations this effect is considered to improve the reversibility of fouling by causing the deposit in the grooves to be looser than that on the fins. While this is only a hypothesis yet not proven, it suggests that inhomogeneities might prove beneficial in terms of the fouling behavior. In this sense, the fibers with varying skin thickness throughout the surface can illustrate different behavior. Beneficial or not for the fouling performance, these cases, which are “unusual” examples of membrane filtration laws, are interesting from a more fundamental point of view.

8.3.4 Polymeric microsieves via phase separation microfabrication

While the majority of this thesis is on microstructured hollow fibers and their fouling behavior, it ends with a “bonus” chapter on microsieves. Phase separation microfabrication is a versatile technique with which many different microstructured films can be made. So far, microsieves proved to be the trickiest of these structures. Difficulties in microsieve release from molds were somewhat relieved through the use of varying pillar arrangements. The most interesting effect was seen in molds with different pillar arrangements, which showed that it is not only the density of the pillars or the distance between neighboring pillars, but also the arrangement that affects

the peeling forces. The effect of pillar arrangements was related to the shrinkage of the polymer solution during phase separation. Combining this information with the solvent-shrinking process of microsieves in the first part of **Chapter 7**, it would be interesting to see how the microsieves with different arrangements of perforations will shrink in solvents.

In microsieve shrinking experiments, several other solvents were tried, such as ethanol, methanol and propanol. While ethanol had some shrinkage effect, the other two alcohols did not cause any shrinkage in the microsieve. This method can be advanced by the use of different solvents and combinations.

8.4 Epilogue

Microstructured membrane surfaces have various effects during filtration processes. While they primarily serve to increase the surface area of a membrane in a given volume, they also alter the concentration polarization near the membrane, the flow profile in the module and consequently the fouling behavior of membranes.

8.5 References

- [1] R.S. Hine, E. Martin; *Dictionary of Biology* (2004); Grange Books
- [2] W. Barthlott and C. Neinhuis; *Purity of the sacred lotus, or escape from contamination in biological surfaces*; *Planta* **202** (1) (1997) 1–8
- [3] J. Jani; *unpublished work*
- [4] I.M. Wienk; *Ultrafiltration membranes from a polymer blend: Hollow fiber preparation and characterization*; Ph.D. thesis; University of Twente (1993)
- [5] D. Airey, S. Yao, J. Wu, V. Chen, A.G. Fane and J.M. Pope; *An investigation of concentration polarization phenomena in membrane filtration of colloidal silica suspensions by NMR micro-imaging*; *Journal of Membrane Science* **145** (2) (1998) 145–158
- [6] Q. Li and M. Elimelech; *Organic fouling and chemical cleaning of nanofiltration membranes: Measurements and mechanisms*; *Environmental Science and Technology* **38** (17) (2004) 4683–4693

- [7] W.G.J. van de Ven, K. van Sant, I.G.M. Pünt, A. Zwijnenburg, A.J.B. Kemperman, W.G.J. van der Meer and M. Wessling; *Hollow fiber dead-end ultrafiltration: Influence of ionic environment on filtration of alginates*; Journal of Membrane Science **308** (1-2) (2008) 218–229
- [8] C.W. Van Oers, M.A.G. Vorstman and P.J.A.M. Kerkhof; *Solute rejection in the presence of a deposited layer during ultrafiltration*; Journal of Membrane Science **107** (1-2) (1995) 173–192
- [9] P. Le-Clech, V. Chen and A.G. Fane; *Fouling in membrane bioreactors used in wastewater treatment*; Journal of Membrane Science **284** (1-2) (2006) 17–53
- [10] M.J. Costello, A.G. Fane, P.A. Hogan and R.W. Schofield; *The effect of shell-side hydrodynamics on the performance of axial flow hollow fibre modules*; Journal of Membrane Science **80** (1993) 1–12
- [11] J. Wu and V. Chen; *Shell-side mass transfer performance of randomly packed hollow fiber modules*; Journal of Membrane Science **172** (1-2) (2000) 59–74

Summary

The research presented in this thesis is about the fabrication, characterization and filtration behavior of microstructured membranes.

Following an introduction to the concepts and methods used in the thesis in **Chapter 1**, the fabrication of hollow fiber membranes with a microstructured outer surface is described in **Chapter 2**. The effect of fabrication parameters such as the air gap, take-up speed, polymer dope viscosity and coagulation value on the fiber microstructure are reported. The fibers are characterized with respect to their permeability, pore size distribution, molecular weight cut-off and skin layer thickness and compared to round fibers fabricated under the same conditions. It is shown that fibers with enhanced surface area and comparable intrinsic permeability and separation performance can be fabricated.

In **Chapter 3** the fouling behavior of these microstructured membranes in dead-end filtrations is reported. NMR imaging was used to visualize silica deposition on the membranes. Different deposition patterns with different silica colloids were observed and this was explained by the thickness and the resistance of the concentration polarization layers. Flux-stepping experiments were done to evaluate the fouling reversibility during filtrations of colloidal silica and sodium alginate. Better fouling reversibility during sodium alginate filtrations was illustrated.

In **Chapter 4**, the microstructured fibers were tested in cross-flow filtrations and their performance was compared to round fibers. Additionally, in separate modules, the structured fibers were twisted around their own axes to see the effect of helical grooves under cross-flow. The critical fluxes for the onset of particle deposition and for the onset of irreversible deposition were determined in flux-cycling experiments using colloidal silica and yeast suspensions as feed solutions. Improved fouling performance of twisted fibers was observed during yeast filtration. Direct visual observation was used to visualize yeast deposition on the fibers and confirmed the better performance of the twisted fibers. It was also shown that deposition occurs earlier within the grooves of the structured fibers.

In **Chapter 5**, the structured, round and twisted fibers were compared in submerged filtrations of colloidal silica with aeration. Effects of aeration rate, module orientation

and bubble size were investigated. It was found that both structured and twisted fibers had higher resistance to filtration when operated at the same permeate flux as the round fibers. Twisting the structured fibers has also shown to improve the fouling performance in these systems.

In **Chapter 6**, the fabrication of hollow fibers with microstructured surface on the bore side is described. Fabrication parameters such as the polymer dope flowrate, bore liquid flowrate, air gap and take-up speed were varied in order to observe their effects on the fiber microstructure and properties. The fibers were characterized and compared to inner-skinned round fibers with respect to their permeability, pore size distribution and skin layer thickness.

In **Chapter 7**, two aspects of polymeric microsieve fabrication by phase separation microfabrication is covered. The first part describes the downscaling of the perforation size by shrinking the microsieves in acetone and acetone-NMP mixtures. In the second part the influence of mold design on the release of the microsieves from the molds is investigated. Molds were designed with different pillar spacings, densities, shapes and arrangements and the peeling forces were measured.

Samenvatting

Het onderzoek beschreven in dit proefschrift omvat de fabricage, karakterisering en filtratiegedrag van microgestructureerde membranen.

Na een introductie van concepten en methoden in **Hoofdstuk 1**, is de fabricage van holle vezel membranen met een microgestructureerde buitenzijde beschreven in **Hoofdstuk 2**. Het effect van fabricage parameters zoals de opname snelheid van de vezels, de viscositeit van de polymeer oplossing en de coagulatie waarde op de microstructuur van de vezel zijn beschreven. De vezels zijn gekarakteriseerd ten aanzien van hun permeabiliteit, porie grootte verdeling, selectiviteit en skin dikte en deze zijn vergeleken met die van ronde vezels die vervaardigd zijn onder dezelfde condities. Het is aangetoond dat de vezels met een toegenomen oppervlak met vergelijkbare intrinsieke permeabiliteit en scheidend vermogen gefabriceerd kunnen worden.

Hoofdstuk 3 beschrijft het vervuiligingsgedrag van deze microgestructureerde membranen tijdens dead-end filtratie. NMR beeldvorming werd gebruikt om silica depositie op de membranen te visualiseren. Verschillende depositie patronen werden waargenomen voor verschillende silica colloïden. Dit werd verklaard middels de dikte en weerstand van de concentratie polarisatie laag. Flux-stap experimenten zijn uitgevoerd om de reversibiliteit van de vervuiling tijdens filtratie van colloïdaal silica en natriumalgi-naat te bepalen. Een betere reversibiliteit van de vervuiling met natriumalgi-naat werd aangetoond voor de gestructureerde vezels.

In **Hoofdstuk 4** zijn de microgestructureerde vezels getest in cross-flow filtraties en vergeleken met ronde vezels. Daarnaast zijn, in verschillende modules, de gestructureerde vezels om hun as gedraaid om het effect van helix vormige groeven tijdens cross-flow te onderzoeken. De kritische flux voor het begin van deeltjes depositie en voor het begin van irreversibele depositie werden bepaald in filtratie experimenten met colloïdaal silica en gist suspensies. Een verbeterd vervuiligingsgedrag van gedraaide vezels werd gevonden tijdens gist suspensie filtratie. Optische microscopie werd gebruikt om de gist depositie op de vezels te visualiseren en de verbeterde prestatie te bevestigen. Daarnaast werd aangetoond dat depositie begint in de groeven van de gestructureerde vezels.

In **Hoofdstuk 5** zijn de gestructureerde, ronde en gedraaide vezels vergeleken tijdens een filtratie van colloïdaal silica gecombineerd met luchtbellens. De beluchtscapaciteit, module orientatie en de bel grootte zijn hierbij onderzocht. Zowel de gestructureerde als de gedraaide vezels hadden een hogere weerstand tijdens filtratie onder gelijke permeatie flux vergeleken met de ronde vezels. Het draaien van vezels leidde wederom tot een verbetering van het vervuilingsgedrag in deze systemen.

Hoofdstuk 6 beschrijft de fabricage van holle vezels met microgestructureerde binnenzijden. Fabricage parameters zoals de stroomsnelheid van de polymeer oplossing, de vloeistof snelheid in het boorgat, de afstand tussen spinneret en coagulatiebad en de opname snelheid werden gevarieerd om hun invloed op de vezel structuur en eigenschappen te bestuderen. De vezels werden gekarakteriseerd en vergeleken met ronde vezels, gebaseerd op permeabiliteit, porie grootte verdeling en skinlaag dikte.

Hoofdstuk 7 omvat twee aspecten van polymere microzeef fabricage middels fasenscheiding microfabricage. Het eerste deel beschrijft het reduceren van de perforaties middels het krimpen van de microzeef in een aceton-NMP mengsel. Het tweede deel beschrijft het onderzoek naar de invloed van mal ontwerp op het lossen van de microzeef van de mal. Mallen werden ontworpen met verschillende pilaar afstand, pilaar dichtheid, vorm en positie waarna de loskracht werd gemeten.

Acknowledgements

I would like to express my gratitude to a number of people without whom the completion of this thesis would not have been possible.

First of all, I want to thank Rob, my daily supervisor at first and my promotor in the last months, for his ideas, help, support and patience during these four years. I would also like to thank my co-promotor Matthias, for his support and for believing in me from the beginning on.

I would like to thank the members of Membrane Technology Group (now partly Soft matter, Fluidics and Interfaces, but anyway, they know who they are) for the nice and peaceful working atmosphere. Among them, there are some people who contributed to this work more than others. I want to thank Erik Rolevink for teaching me how to spin hollow fibers and his other small lab tricks and Herman for his help in SEM, permporometry and spinning. It was a very valuable experience for me to share a lab with them. I also want to thank John and Ineke for their help in the lab and Greet for her help with all the paperwork and answering my never-ending questions.

I would like to thank all my office-mates, Wilbert, Tymen, Hakan, Joao, Erik, Geraldine, Al-Hadidi and the office-neighbors, especially Katja, Ikenna and Can for their company. I would like to thank Wilbert also for helping me with his setup and Jigar for his help in COMSOL.

I had two master students during the course of my PhD, both of whose work contributed to this thesis. Joan and Maryam, thank you very much for the nice work you have done. I also want to thank Matías for his collaboration during the project and especially during the supervision of Joan.

During this study I collaborated with several people from other research groups. The work we did together with Steffen Buetehorn, Lavinia Utiu, Thomas Melin, Markus Kueppers and Bernard Bluemich from RWTH Aachen University created one of my favourite chapters in the thesis and I would like to thank these people for the smooth collaboration. We also worked together with Yujie Ma and Christian Blum from the Biophysical Engineering group of the UT and I want to thank them as well for their help.

Acknowledgements

It was a very nice working environment thanks to all these people I mentioned, but I must say that what made these four years unforgettable for me was outside this environment. Some of these people were with me since our first day and I met some later, but I cannot imagine how I could survive all this time without them. Vasilis, Dimitris (the wise), Dimitris (the Parisian), Kosmas, Oya, Banu, Oktay, Erhan, Arzu, Engin, Duygu, Tasos, Antonis, Kostas, Marcela, Diego.. Thank you all for the good times at Macandra, at Bolwerk, the food, the drinks, the ideas, the laughter, the music and the friendship we shared. I am grateful to Faruk and Nilüfer for all their help and I hope to share a neighbourhood again some time, perhaps somewhere else. I also want to thank my good old friend Belma for always being a relief and a reason to smile when I felt bad, even though she was actually far away.

Last but not least, there are the people whom I really do not know how to thank.. I am deeply grateful to my mother, my father and my brother, for always being there for me, supporting me, respecting me and inspiring me. And to Aytaç, for being the wonderful person he is, for finding me, sharing this life with me, for the hope and happiness he brings to my life. For the good times past, and better ones to come!

Zeynep

